

DEVELOPING A NEW INTERATOMIC POTENTIAL AND ATOMISTIC STUDY OF NiTiHf

By

Saeed Ataollahi

Dr. Mohammad Mahtabi
Assistant Professor of Mechanical Engineering
(Chair)

Dr. Hamdy Ibrahim
Assistant Professor of Mechanical Engineering
(Committee Member)

Dr. Aref Yadollahi
Assistant Professor of Mechanical Engineering
(Committee Member)

Dr. Rahul Bhosale
Assistant Professor of Chemical Engineering
(Committee Member)

DEVELOPING A NEW INTERATOMIC POTENTIAL AND ATOMISTIC STUDY OF NiTiHf

By

Saeed Ataollahi

A Dissertation Submitted to the Faculty of the University
of Tennessee at Chattanooga in Partial Fulfillment of
the Requirements of the Degree of Doctor of
Philosophy in Computational Science

The University of Tennessee at Chattanooga
Chattanooga, Tennessee

December 2023

Copyright © 2023
Saeed Ataollahi
All Rights Reserved

ABSTRACT

With the growing demand for high-temperature shape memory alloys (HTSMAs), NiTi-based HTSMAs have gained more attention for implementation in applications at elevated temperatures. Among NiTi-based alloys, NiTiHf has shown to have great potential, by having high transformation temperatures, lower preparation cost and good thermal stability. However, until today, most studies conducted on NiTiHf have focused on a limited range of compositions due to the difficulties and high cost of the experimental studies. Therefore, there exists a lack of comprehensive research on the thermo-mechanical behavior of these HTSMAs. Computational simulations are a very cost-effective and feasible approach for addressing this shortcoming. Among computational methods, molecular dynamics (MD) simulation as an atomistic method offers comprehensive means to explore microstructural phenomena that govern the behavior of material. An essential requirement for performing MD simulations is interatomic potential which serves as the constitutive equations of MD and determine the forces and interactions between atoms. Since no applicable interatomic potential has been developed for NiTiHf, there has not been any progress in MD studies on NiTiHf alloys. Therefore, in this study, a Second Nearest-Neighbor Modified Embedded Atom Method (2NN MEAM) interatomic potential has been developed to accurately represent the NiTiHf ternary system. Initially, the parameters of constituent unary and binary potentials were calibrated by fitting their reproduced results of physical properties to DFT results. Then, the final ternary MEAM potential was checked for reliability and transferability

by performing MD simulations. The results showed that the developed potential can accurately capture temperature-induced and stress-induced martensitic phase transformation in NiTiHf. In addition, the lattice parameters and formation energy of different compositions of NiTiHf were obtained and compared with experimental and DFT (Density Functional Theory) results showing a good agreement. Furthermore, using the developed MEAM potential, MD simulations were conducted to analyze the influence of precipitates on the superelasticity and shape memory effect of NiTiHf alloy. The results showed that in the presence of H-phase precipitates, the transformation temperatures increase. In addition, the thermal cycling of NiTiHf under constant stress was simulated and it was found that reducing the temperature rate results in a narrower thermal hysteresis.

DEDICATION

A heartfelt dedication to the loving memory of my late father.

ACKNOWLEDGMENTS

I would like to express my deepest gratitude to my advisor, Dr. Mohammad Mahtabi who provided his guidance for me to complete this research, and for his encouragement and support throughout my PhD study during the last four years. He was always available whenever I had questions along this research study. Without his incredible knowledge, wisdom and patience, my dissertation work would have been an overwhelming pursuit.

I would also like to thank the other members of my dissertation committee Dr. Ibrahim, Dr. Bhosale and Dr. Yadollahi, for their invaluable help and support throughout this journey.

TABLE OF CONTENTS

ABSTRACT	iv
DEDICATION	vi
ACKNOWLEDGMENTS	vii
LIST OF TABLES	x
LIST OF FIGURES	xi
LIST OF SYMBOLS	xiv
LIST OF ABBREVIATIONS	xv
CHAPTER	
1. INTRODUCTION AND MOTIVATION	1
1.1 A Brief Background on Shape Memory Alloys	1
1.2 Statement of Problem	5
1.3 Objectives and Technical Approach	14
2. BACKGROUND	16
2.1 Interatomic Potential	16
3. DEVELOPMENT OF TERNARY NITIHf MEAM POTENTIAL	26
3.1 Methodology	26
3.2 Density Functional Theory	26
3.3 Calibration of Unary MEAM Potentials (Ni, Ti)	27
3.4 Calibration of Binary MEAM Potentials (NiTi, HfNi and HfTi)	34
3.5 Calibration of Ternary MEAM Potential (NiTiHf)	37
3.6 Calculation of Lattice Parameters Using the Developed MEAM Potential	39
3.7 Simulation of the Temperature- and Stress-induced Phase Transformation	41

4. PRECIPITATE PHASE IN NiTiHf (H-PHASE)	50
4.1 Challenges in Employing HTSMAs	50
4.2 Precipitation in NiTiHf	50
4.3 Methodology	55
5. THERMAL ACTUATION OR CYCLING IN NiTiHf	66
5.1 Introduction to the Thermal Actuation	66
5.2 Methodology	69
5.3 Results	70
6. SUMMARY, CONCLUSIONS AND FUTURE WORKS	74
6.1 Summary and Conclusions	74
6.2 Future Works	79
REFERENCES	81
VITA	94

LIST OF TABLES

3.1	Parameters of the unary MEAM potentials for Ni, Ti, and Hf. E_c (eV/atom) is the cohesive energy; r_e (Å) is the equilibrium nearest-neighbor distance; B (GPa) is the bulk modulus. All other parameters are dimensionless	33
3.2	The physical properties of Ni and Ti, including their calculated values using both DFT and the developed MEAM potentials, as well as their corresponding experimental values. Cohesive energy is denoted as E_c (eV/atom); a and c (Å) denote the lattice constants; B is the bulk modulus and C_{11} , C_{12} , C_{13} , C_{33} and C_{44} (GPa) are the elastic constants; E_f^{vac} (eV) denote the vacancy formation energy; and $E_{(111)}^{(surf)}$, $E_{(110)}^{(surf)}$, $E_{(100)}^{(surf)}$, $E_{(0001)}^{surf}$, $E_{(10\bar{1}0)}^{surf}$, $E_{(10\bar{1}1)}^{surf}$ and $E_{(2\bar{1}\bar{1}2)}^{surf}$ (mJ/m ²) represent the surface energies	35
3.3	Parameters of the binary MEAM potentials for HfNi, HfTi and NiTi. E_c (eV/atom) is the cohesive energy; r_e (Å) is the equilibrium nearest-neighbor distance. All other parameters are dimensionless	37
3.4	The physical properties of HfNi, HfTi and NiTi, including their calculated values using both DFT and the developed MEAM potentials. a (Å) denotes the lattice constant; ΔE_f (eV/atom) is the formation energy; C_{11} , C_{12} and C_{44} (GPa) are the elastic constants . . .	38
3.5	Parameters of the ternary MEAM potential for NiTiHf	40
3.6	Formation energy (ΔE_f (eV/atom)) of B2 and B19' structures of various compositions of NiTiHf calculated by DFT and developed MEAM Potential	42
4.1	Precipitate's shape, size and crystal structure	57

LIST OF FIGURES

1.1	Temperature-induced phase transformation of SMAs and phase transformation temperatures	2
1.2	Stress-strain-temperature graph showing superelasticity and SME	3
1.3	B2 and B19' unit cells of NiTi	4
1.4	Tensile, compressive and shear response of binary NiTi [24]	5
1.5	Variable geometry of engine nozzle fan chevrons made of HTSMA [33]	7
1.6	Comparison M_s temperature and transformation strain between HTSMAs [35]	12
1.7	Dependence of martensite peak temperature (M_p) to the content of Hf in NiTiHf alloy system [35]	13
1.8	Martensite peak temperature (M_p) at different compositions of $Ni_xTi_{90-x}Hf_{10}$ [35]	14
2.1	Time-versus length-scale demonstration of different simulation methods [72]	17
2.2	Relationship between interaction energy and atomic distance, r. Dashed line represents hard sphere model, and the solid line shows the Lennard-Jones model [75]	19
3.1	Energy versus lattice parameter curves of Ni obtained via DFT and the developed MEAM potential	29
3.2	Energy versus lattice parameter curves of Ti obtained via DFT and the developed MEAM potential	30
3.3	Three scenarios of depicting the screening of interactions between two adjacent atoms of different types by a third atom in the Ni-Ti-Hf ternary system	38
3.4	Comparison of experimental lattice constants of B2 and B19' structures of NiTiHf with varying Hf content, with calculated lattice constants using the developed MEAM potential	41
3.5	Simulated $Ni_{50.3}Ti_{29.7}Hf_{20}$ model and its dimensions	43

3.6	The change of the rate of martensitic transformation with respect to the temperature, denoting transformation temperatures. Sudden jumps in atomic volume during heating and cooling indicate the phase transformation. In insets, B2 structure is shown in blue and B19' is shown in red	45
3.7	Ni _{50.3} Ti _{29.7} Hf ₂₀ model size effect on the values of M_s and A_f obtained from MD simulations	47
3.8	Stress-strain graphs of Ni _{50.3} Ti _{29.7} Hf ₂₀ subjected to compression in [100] direction at (a) 200 °C ($T < M_f$), and (b) 350 °C ($T > M_s$), computed by the developed ternary MEAM potential. In insets, B2 structure is shown in blue and B19' is shown in red	48
3.9	Stress-strain graph of Ni _{50.3} Ti _{29.7} Hf ₂₀ subjected to compression in [100] direction at 700 °C ($T > A_f$), computed by the developed ternary MEAM potential. In insets, B2 structure is shown in blue and B19' is shown in red	49
4.1	Distribution of the precipitates in B2 alloy matrix [139]	52
4.2	Spindle-shaped precipitates in aged Ni _{50.3} Ti _{29.7} Hf ₂₀ [69]	54
4.3	Electron diffraction patterns of the precipitates and their angular relationships with B2 parent phase [69]	55
4.4	Unit cell of the orthorhombic precipitate [69]	56
4.5	Embedded precipitate in single-precipitate NiTiHf matrix	58
4.6	Distribution of fine precipitates in multi-precipitate NiTiHf matrix	59
4.7	Variation of the rate of martensitic transformation with respect to the temperature, denoting transformation temperatures. Sudden changes in the rate of transformation during heating and cooling indicate the phase transformation	60
4.8	Present phases at the end of the cooling stage. Red atoms show martensite and blue atoms show austenite phase	61
4.9	Stress-strain behavior of models simulated at 0 °C	62
4.10	Presentation of the coherency of precipitates before and after equilibration at 0 °C	63
4.11	Stress-strain behavior of models simulated at $A_f + 50$ °C	64
4.12	Stress-strain behavior of models in [110] direction at 0 °C and 750 °C	65

5.1	F18's folding wings and torque tube assembly for actuating the folding wings [154] . . .	68
5.2	Detail of plate model in thermal cycling	69
5.3	Stress-strain response of the plate model at 500 °C	70
5.4	Shape memory response of the material obtained via thermal cycling with rates under constant stress of 400 MPa	71
5.5	(a) Stress-strain-temperature curve, and (b) shape memory response of the material subjected to thermal cycling under 600 MPa constant stress	72
5.6	(a) Stress-strain-temperature curve, and (b) shape memory response of the material subjected to thermal cycling under 800 MPa constant stress	72
5.7	(a) Stress-strain-temperature curve, and (b) shape memory response of the material subjected to thermal cycling under 1000 MPa constant stress	73
6.1	Schematic presentation of common materials strength [159]	79

LIST OF SYMBOLS

M_s , Martensite start temperature

M_f , Martensite finish temperature

A_s , Austenite start temperature

A_f , Austenite finish temperature

σ^{AM} , Austenite to martensite stress

M_p , Martensite peak temperature

B , Bulk modulus

E_c , Cohesive energy

E_f^{vac} , Vacancy formation energy

E_{hkl} , Surface energy

ΔE_f , Formation energy

LIST OF ABBREVIATIONS

SMA, Shape memory alloy

DSC, Differential scanning calorimetry

TT, Transformation temperature

SME, Shape memory effect

NiTi, Nickel-titanium

HTSMA, High-temperature shape memory alloy

NiTiHf, Nickel-titanium-hafnium

MD, Molecular dynamics

EAM, Embedded atom model

2NN MEAM, Second nearest-neighbor modified embedded atom method

LJ, Lennard-Jones

EMT, Effective-medium-theory

TB-SMA, Second-moment approximation of tight binding

fcc, Face-centered cubic

bcc, Body-centered cubic

hcp, Hexagonal close-packed

DFT, Density functional theory

MPC, Meam potential calibration

PAW, Projector augmented wave

PBE, Perdew-Burke-Ernzerhof

PTM, Polyhedral template matching

XRD, X-ray diffraction

STEM, Scanning transmission electron microscopy

HAADF, high-angle annular dark field

APT, Atom probe tomography

CHAPTER 1

INTRODUCTION AND MOTIVATION

1.1 A Brief Background on Shape Memory Alloys

Shape memory alloys (SMAs) form one of the most important classes of materials that can recover their original shape after deformation when heated to a certain temperature. This shape recovery can even happen under high levels of applied loads resulting in high actuation energy densities. Moreover, in response to mechanical cyclic loading, SMAs undergo a reversible hysteretic shape change, absorbing and dissipating mechanical energy. These unique characteristics of SMAs have made them a popular candidate for actuation and sensing (In actuation, a non-mechanical input, such as thermal energy, undergoes a conversion to mechanical output. Conversely, a sensor operates by converting a mechanical input into a non-mechanical output [1]) applications [2–5]. Over the past few decades, SMAs have been employed in different sectors of industry such as biomedical, aerospace and automotive [6–8]. Two key properties distinguish SMAs from regular engineering metals: superelasticity and the shape memory effect. The shape memory effect is the capability of recovering the pre-deformed shape when heated, and superelasticity is defined as the reversible elastic behavior. The driving factor in these unique characteristics is the reversible phase transformation. SMAs exhibit two distinct phases in their activation temperatures. Accordingly, the crystal structure and properties of SMA change depending on the present phase. The high-temperature phase which is generally cubic is called austenite, and the low-temperature phase which may have tetragonal, orthorhombic or monoclinic structure, is called martensite [9]. The phase transformation from austenite (parent phase) to martensite (product phase) can occur due to external stress (stress-induced phase transformation), or due to a temperature change (temperature-induced phase transformation) [10]. The phase transformation in SMAs is diffusionless and happens by shear distortion of lattices [1]. The

transformed martensite can have different crystallographic orientations which are called variants. The present variants in the martensitic phase can result in two types of twinned and detwinned martensite [11].

In a temperature-induced phase transformation, when the SMA is cooled from a high temperature, it begins to transform from austenite to twinned martensite at martensite start temperature (M_s). By cooling the material to lower temperatures, the transformation finishes at martensite finish temperature (M_f). Then by heating the SMA from low to high temperatures, the phase transformation starts at austenite start temperature (A_s) and by further heating, transformation becomes complete at austenite finish (A_f) temperature. Figure 1.1 shows a schematic Differential Scanning Calorimetry (DSC) graph that represents heat flow with respect to the temperature. This analysis method is the most well-known approach for the determination of the transformation temperatures (TTs: M_s , M_f , A_s and A_f).

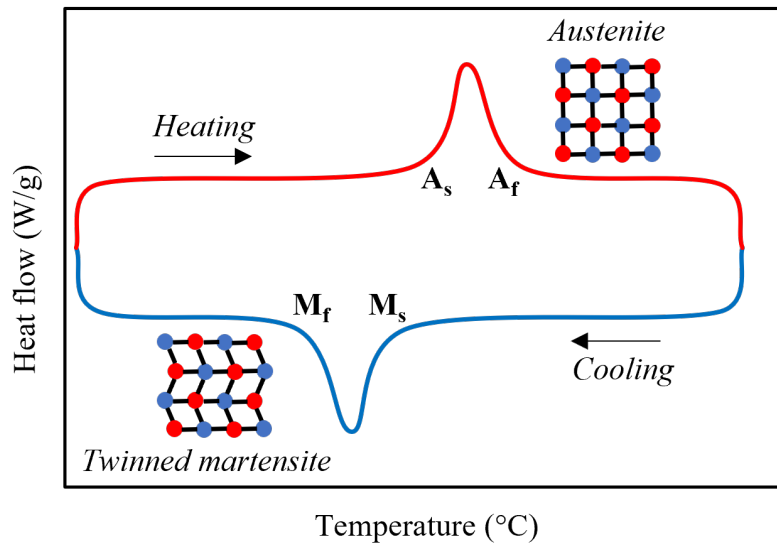


Figure 1.1 Temperature-induced phase transformation of SMAs and phase transformation temperatures

In stress-induced phase transformation, depending on the temperature that the load is being applied to the SMA, the response of the material can be different. Figure 1.2 presents

a stress-strain-temperature graph for a typical SMA. If the temperature is above A_f , the phase transformation will occur at sufficiently high stress levels (above σ^{AM}) from austenite to detwinned martensite. At the end of unloading, a complete shape recovery is obtained with no residual strain. Moreover, the detwinned martensite at the end of loading transforms to parent austenite upon unloading. This behavior is called pseudoelasticity or superelasticity and has been demonstrated by the red stress-strain curve in Figure 1.2. However, if the load is applied at a temperature below M_f , the initial twinned martensite (refer to Figure 1.1) subjected to a sufficiently high stress, transforms into detwinned martensite. Upon unloading, the material elastically deforms and the detwinned martensite is still retained (blue stress-strain curve in Figure 1.2). By heating the material, the residual strain starts to recover at A_s and it completely recovers at temperatures above A_f . In addition, the detwinned martensite transforms into austenite. This behavior is called the shape memory effect (SME) and has been shown by the strain-temperature curve in Figure 1.2.

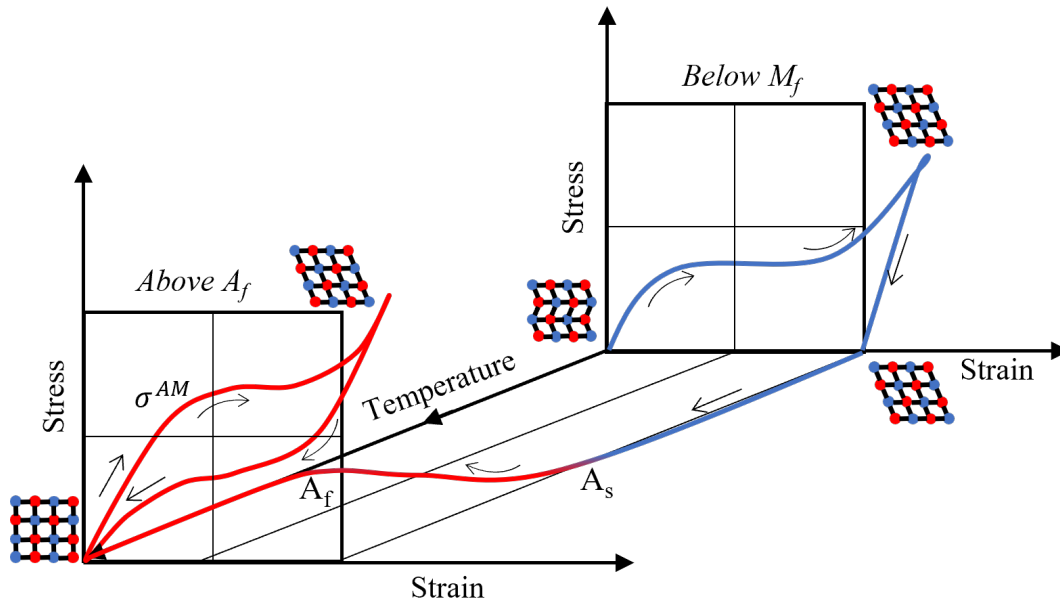


Figure 1.2 Stress-strain-temperature graph showing superelasticity and SME

Among the SMAs, nickel-titanium (NiTi) is the most important and popular one. Soon after its discovery in 1959, nearly equiatomic NiTi rose to prominence and attracted research interest towards SMAs [12]. Due to its excellent thermo-mechanical properties, NiTi is used in numerous commercial applications today. Under purely mechanical and thermal loads, large strain recovery is made possible thanks to NiTi's superelasticity and SME. Although NiTi shares some common properties with other SMAs, it also presents some unique characteristics. NiTi exhibits low elastic anisotropy compared to other SMAs, which makes it quite ductile leading up to 60% cold working (under certain conditions) [13]. In addition, it has superb biocompatibility, and corrosion and abrasion resistance. These superior properties have made NiTi an interesting candidate for automotive and biomedical applications [14–20]. At high-temperature austenite phase, NiTi has an ordered B2 (CsCl) type crystal structure, with a lattice constant of 0.3015 nm [21]. Upon cooling and in the martensite phase, it exhibits a B19' monoclinic crystal structure. Figure 1.3 shows NiTi's austenitic B2 and martensitic B19' crystal structures.

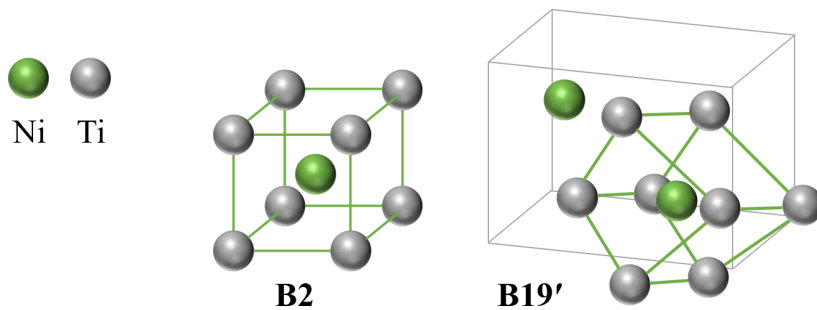


Figure 1.3 B2 and B19' unit cells of NiTi

The mechanical behavior of NiTi SMAs is influenced by their composition and aging process, and also by the direction of applied stress. This means that the shape memory behavior can vary depending on whether the SMA is subjected to tension, compression, or torsion [22, 23]. Figure 1.4 illustrates the tension, shear, and compression behavior of NiTi SMAs [24]. The flat stress plateau is evident in tension and torsion but not in compression. Additionally, the maximum

stress after 6% deformation is approximately 800 MPa under compression, however, it is less than 200 MPa for tension and torsion. The variation of deformation mechanisms during phase transformation and morphology of the martensite phase are reasons for this asymmetry in the mechanical properties of NiTi. Under compression, the interaction of different variants is more pronounced, and detwinning is more challenging compared to tension or torsion. This results in a higher stress-strain slope during the transformation process and a lower transformation strain. Moreover, the observed types of twinning can also differ depending on the applied stress direction.

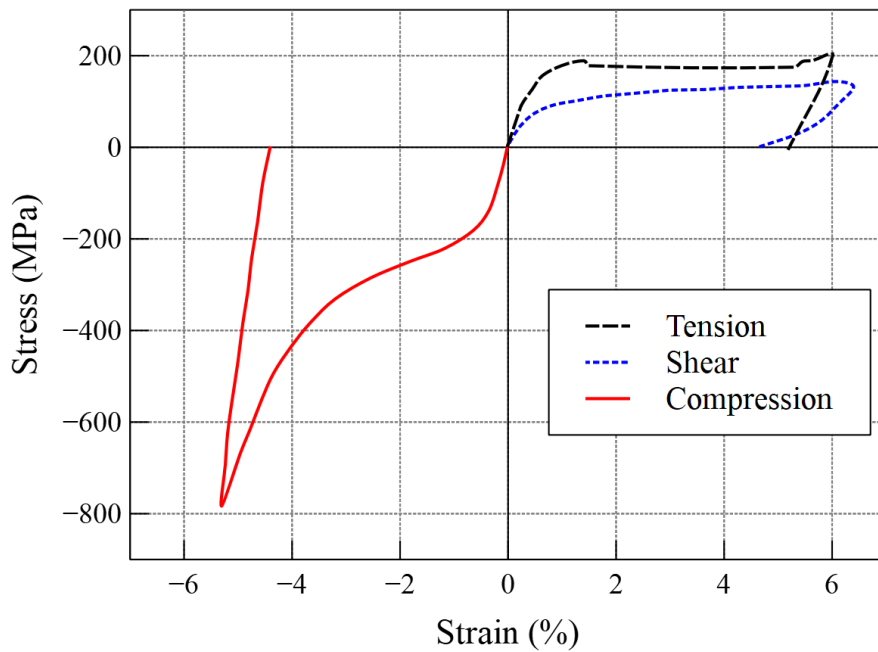


Figure 1.4 Tensile, compressive and shear response of binary NiTi [24]

1.2 Statement of Problem

In spite of excellent properties of NiTi and in general SMAs, their use in high-temperature applications is limited. Since the TTs in SMAs are typically limited to below 100 °C, when employed at high temperatures, SMAs cannot exhibit proper superelasticity and SME properties [25–27]. These unique properties of SMAs can be even more advantageous at high-temperature

applications where they can reduce complex multi-component assemblies to single piece adaptive components. This design improvement will reduce the possibility of wear and damage by lower weight and volume of the components. An example of a high-temperature application can be found in satellite antennae [28]. These antennae are designed to be compactly stored during transportation but can be deployed when needed by applying a low electrical current to activate the SMA based antenna. To ensure optimal functionality, orbital satellites employing this technology often necessitate the use of high-temperature shape memory alloys with transformation temperatures exceeding 100°C. This precautionary measure prevents unintended actuation in the event of direct sunlight exposure. Another notable application of SMAs at high temperatures is in constrained recovery, where the SMA component is deliberately prevented from returning to its original shape upon heating, resulting in the generation of substantial stresses [29]. This particular property can be effectively utilized for fastening multiple components together or connecting pipes and tubes, among other applications. However, it is important to note that currently available SMAs suffer from material property degradation, rendering them unsuitable for the aforementioned applications due to the risk of failure arising from insufficient material strength [29]. The growing demand for SMAs that can operate at high temperatures is largely driven by their potential applications in solid-state actuators. SMA-based actuators have been found to exhibit higher energy densities compared to pneumatic actuators and DC motors, and are comparable to hydraulics, all while significantly reducing weight [30]. The combination of being lightweight, frictionless, and noiseless makes SMA-based solid state actuators highly desirable for weight-critical systems like jet turbine engines, spacecraft, and other aerospace applications [6]. Consequently, the development of high-temperature shape memory alloys (HTSMAs) will play a crucial role in enabling the practical utilization of SMAs in aerospace applications, including clearance control in compressor and turbine sections of jet engines, variable area and geometry inlets for subsonic jets, self-damping components in fuel line clamps, down-well flow control valves, as well as electrical appliances and actuators in close proximity to engine parts in automobiles [31, 32]. Figure 1.5 [33] shows image of an experimental work on reconfigurable engine nozzle fan chevrons of a Boeing airplane made of HTSMAs.

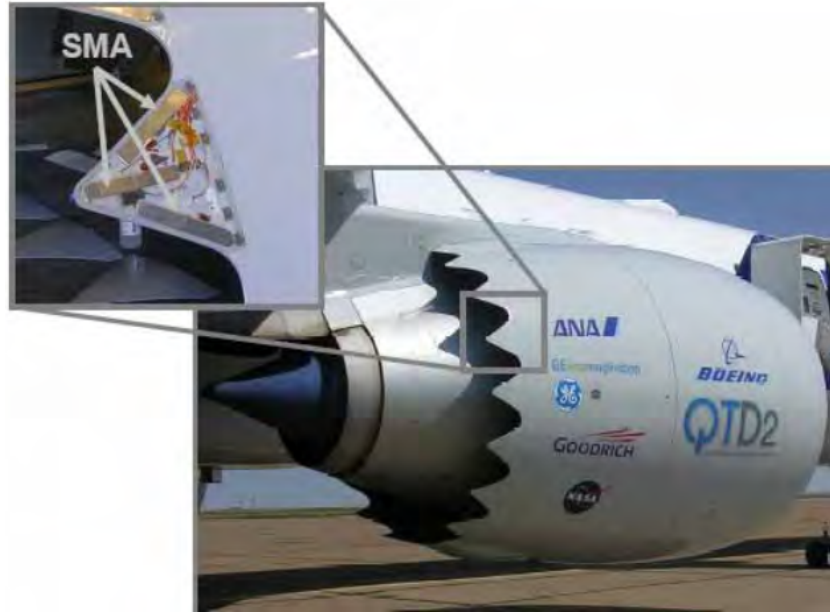


Figure 1.5 Variable geometry of engine nozzle fan chevrons made of HTSMA [33]

Several commonly proposed approaches for modifying the activation temperature range in SMAs include the following [13, 34–37]:

- Alloy Composition: Adjusting the chemical composition of SMAs can effectively alter their TTs. By incorporating different elements or adjusting their ratios, it is possible to tailor the activation temperature range to suit specific application requirements.
- Heat Treatment: Applying various heat treatment processes, such as annealing or quenching, can significantly impact the TTs of SMAs. Controlled heating and cooling procedures can help achieve desired activation temperature ranges.
- Microstructural Control: Manipulating the microstructure of SMAs through techniques like grain refinement or precipitation hardening can influence their transformation behavior. This, in turn, allows for the modification of the activation temperature range.
- Alloy Combination: Utilizing hybrid or composite SMAs by combining different types of shape memory alloys can broaden the range of activation temperatures. By carefully

selecting and combining suitable alloys, the activation temperature range can be effectively modified.

- **Doping and Alloying:** Introducing dopants or alloying elements into SMAs can alter their transformation characteristics and consequently modify the activation temperature range. The addition of specific elements can shift the TTs higher or lower as desired.
- **Mechanical Processing:** Applying mechanical deformation techniques like cold rolling to SMAs can induce dislocation movements, leading to changes in their TTs. This approach offers a means to control the activation temperature range.

Many attempts have been undertaken to develop high-temperature shape memory alloys. However, many times the outcomes have often been unsatisfactory for some systems such as CoNiAl, RuTa and NiMnGa, as these alloys either possess inadequate mechanical or shape memory properties at elevated temperatures or come at a considerable cost. Some of the issues in such cases include [10, 38, 39]:

- **Inadequate Mechanical Properties:** Several HTSMAs exhibit compromised material strength and ductility when subjected to high temperatures. This limitation restricts their applicability in demanding environments where robust mechanical performance is essential.
- **Unstable Cyclic Behavior:** HTSMAs may display undesirable cyclic behavior, such as creep (time-dependent deformation under constant stress) and fatigue (progressive structural damage under repeated loading). These phenomena can hinder the reliability and long-term durability of HTSMAs under high-temperature conditions.
- **Limited Recoverable Strain:** The recoverable strain can be significantly diminished at high temperatures. This reduction in recoverable strain restricts the effectiveness of HTSMAs in applications that require substantial shape memory effects.
- **High Cost:** Some HTSMAs are prohibitively expensive due to the complex manufacturing processes or the scarcity and high cost of the constituent elements involved. The cost factor presents a significant obstacle to the widespread adoption of HTSMAs in various industries.

NiTi-based HTSMAs have attracted considerable research interest due to the unique characteristics of NiTi. There are a few elements such as Pt, Cu, Pd, Zr and Hf that can be used for alloying with NiTi to form ternary and quaternary alloys [29, 40–45]. TTs of these alloys exhibit a strong dependency on their composition [46]. Even a slight increase in the Ni content away from the stoichiometry of Ni-rich intermetallic compounds, results in a sharp decrease in TTs, while the Ti-rich side of the intermetallic compound is less affected by compositional variations, primarily due to the precipitation of NiTi₂ particles, which act against the compositional changes in the matrix [28]. The addition of ternary elements, typically in concentrations less than 10%, generally has minimal impact on the M_s or has a slight decreasing effect [13]. Substituting Ni with Fe or Co, or Ti with Mn, Cr, or V, significantly decreases the TTs of the alloys. Conversely, the addition of more than 10% of Au, Hf, Pd, Pt, or Zr to NiTi increases the transformation temperature [29]. Moreover, when Cu and Fe is added to NiTi, followed by application of a low-temperature heat treatment, the thermal hysteresis reduces significantly to only a few degrees. Conversely, the addition of Nb has the opposite effect, increasing the hysteresis to approximately 100 °C [47].

One of the successful works on modification of TTs was a study [35] on the solid solution between PdTi and NiTi at high temperatures [48] determined that M_s exhibits a uniform decreasing trend when Pd substitutes Ni, with the lowest values observed for ternary compositions containing 5-10 at.% Pd [49]. Consequently, Pd was added to NiTi alloys to increase the TTs by substituting for Ni. Initially, adding Pd to replace Ni in NiTi results in a decrease in M_s , reaching a minimum value of -26 °C for up to 10 at.% Pd addition. However, when Pd content increases to approximately 20 at.%, there is a substantial increase in M_s , reaching around 100 °C. Shimizu et al. [50] examined the effect of stoichiometry on TTs for Ni_{20+x}Ti_{50-x}Pd₃₀ alloys (x ranging from -0.6 to 1.5%) and found a significant decrease in TTs for Ti-lean alloys, while Ti-rich alloys exhibited only moderate variation in TTs, following the trend observed in binary NiTi alloys. Alloys containing over 40 at.% Pd exhibited poor shape memory properties due to the low critical stress for slip. To enhance shape memory properties, small amounts of boron were added in some studies. However, Yang et al. [51] and Shimizu et al. [50] found no significant effect on TTs

and shape memory properties with the addition of boron, although it increased the ultimate tensile strength by approximately two times and improved ductility.

Furthermore, to improve shape memory properties, Shimizu et al. [50] utilized precipitation hardening by deviating from the stoichiometric ratio in $\text{Ni}_{19.4}\text{Ti}_{50.6}\text{Pd}_{30}$ alloy. This induced the precipitation of homogeneous NiTi_2 particles, resulting in approximately 10% higher recovery rate compared to $\text{Ni}_{20}\text{Ti}_{50}\text{Pd}_{30}$ due to the homogeneous precipitate distribution. It should be noted that the requirement for a higher percentage of Pd to achieve a significant increase in TTs outweighs the benefits when considering the cost of the expensive component in commercial alloys.

Compared to NiTiPd, NiTiAu exhibits higher TTs with the same content of Au instead of Pd. However, the amount of work in NiTiAu alloys is much less. In two studies on two extremes of Au content in the alloy, Eckelmeyer [52] and Donkersloot [53] investigated the influence of 2 at.% Au and 40-50 at.% Au, respectively. A qualitative demonstration of one way shape memory was achieved through the bending and subsequent recovery of a bar composed of higher Au content, while no two way shape memory effect was observed.

In the context of increasing the TTs with the addition of ternary elements, NiTi alloys containing Pt exhibit higher TTs compared to other NiTi-based systems. When substituting Ni with Pt, there is a slight decrease in TTs within the range of approximately 10 at.%, but beyond this threshold, there is an almost linear increase in M_s . In fact, alloys with 50 at.% Pt have been reported to reach an impressive M_s of 1040 °C. Studies conducted by Lindquist and Wayman [54] recorded narrow hysteresis for all Pt containing alloys, except for the 30 at.% Pt alloy, which exhibited a hysteresis of around 80 °C, higher than the general range of 20 °C. However, the extremely low ductility of the alloy prevented the measurement of recoverable strains in the study. Another study by Hosoda et al. [55] reported a general decrease in ductility with increasing Pt content in the alloy. Despite the extremely high TTs, similar to other mentioned HTSMAs, alloys containing Pt face significant challenges due to the high cost and very low ductility.

The addition of Zr to NiTi alloys has been investigated as a cost-effective alternative to Pd and Pt. In NiTiZr alloys, any increase in the TTs is observed only when the zirconium content exceeds 10 at.%. Above this threshold, the addition of zirconium to the alloy leads to an increase in

M_s at a rate of approximately 18 °C/at.-% of zirconium [56]. Moreover, similar to other HTSMAs, the concentration of Zr in NiTiZr alloys has a significant impact on the transformation process. At Zr concentrations below 20 at.%, the B2 phase transforms to B19' during cooling. However, at higher Zr concentrations (greater than 20 at.%), the martensite structure changes to B19 [35, 57]. In addition, one of the main challenges associated with NiTiZr alloys is their lower stability during cycles of transformation. Unlike other SMAs that stabilize after a few cycles, NiTiZr alloys do not stabilize their TTs even after 100 thermal cycles [57].

The expensive nature of Pd, Pt, and Au limits their usage to specific high-priority applications, such as aerospace, where performance outweighs cost considerations. Additionally, Zr is known for its strong affinity towards oxygen [25, 29, 58]. Among the potential HTSMAs, NiTiHf shows great promise for a wide range of applications within the critical temperature range of 100-300 °C [59]. This is due to its cost-effectiveness, exceptional shape memory properties, high work output and good thermal stability [35]. Previous studies have indicated that Hf has a more significant impact on TTs compared to Pd and Au, even at similar content [60, 61]. Similar to other HTSMAs, TTs in NiTiHf are highly dependent on the composition of the alloy. The TTs of NiTiHf alloys exhibit minimal increase up to the content of 10 at.% Hf. However, when the chemical concentration exceeds 10 at.% Hf, TTs show a linear increase, reaching up to 525 °C for a content of 30 at.% Hf when Hf atoms substitute Ti atoms [59]. In Figure 1.6 [35], a schematic comparison of different HTSMAs is presented in terms of their M_s temperature and transformation strain. The top three alloys i.e. NiTiPt, NiTiAu and NiTiPd are the ones that have limited use due to their expensive nature. However, the next HTSMA that exhibits a good combination of high transformation temperature and shape memory strain, is NiTiHf.

Figure 1.7 [35] illustrates the variation in martensite peak temperature (M_p) as a function of Hf content in NiTiHf alloys. The plot indicates that M_p remains unchanged with the addition of up to 3 at.% Hf. However, it starts to increase after reaching 5 at.% Hf. For Hf concentrations up to 10 at.%, the rate of increase in M_p is approximately 5 °C/at.% Hf. Beyond 10 at.% Hf, there is a sudden and significant rise in M_p , with an increase of nearly 20 °C/at.% Hf. In NiTiHf alloys, the M_p can reach up to 400 °C for an alloy containing 25% Hf.

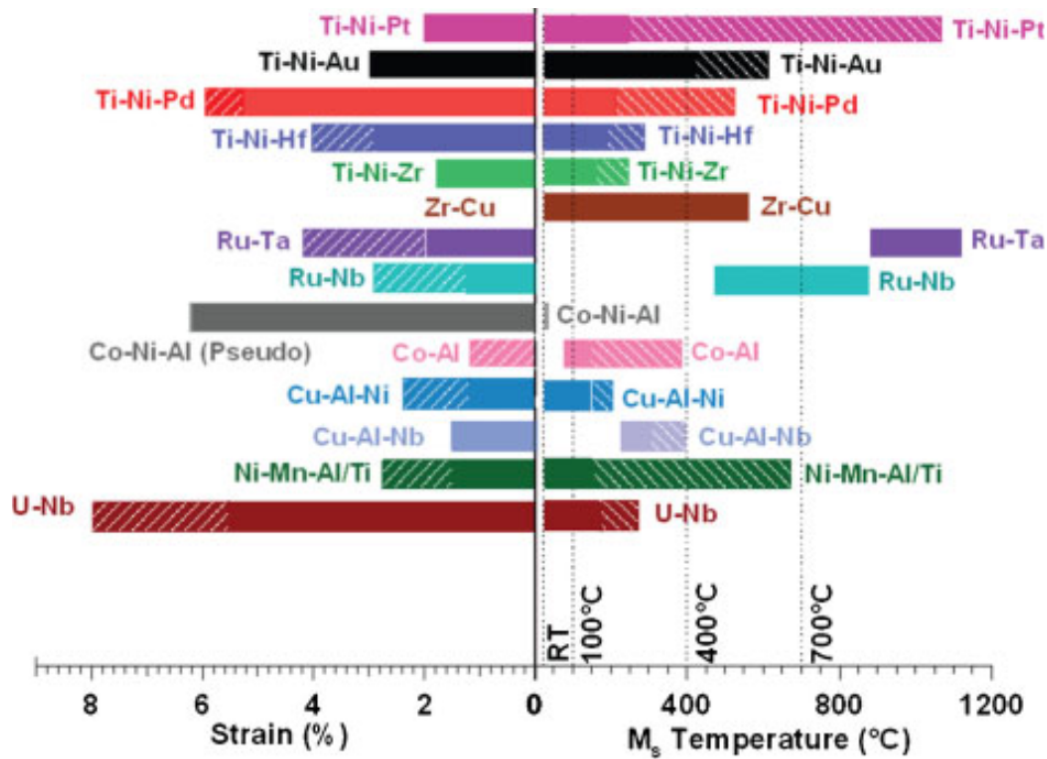


Figure 1.6 Comparison M_s temperature and transformation strain between HTSMAs [35]

In Figure 1.8 [35], the effect of Ni content on M_p is shown for NiTiHf alloys with a fixed Hf content of 10 at.%. The plot demonstrates that M_p is not significantly influenced by the concentration of Ni up to 50 at.%. However, beyond this point, there is a drastic decrease in M_p , eventually falling below 0 °C as the Ni content increases.

NiTiHf alloys exhibit superior resistance to slip and higher transformation strains compared to NiTi alloys in both tension and compression. The addition of Hf in NiTiHf alloys leads to an increase in transformation strains, allowing even small amounts of Hf to enhance the transformation behavior. When subjected to compression, NiTiHf alloys can achieve transformation strains of up to 7%, while in tension, they can reach levels as high as 15%. However, binary NiTi alloys have demonstrated compressive strains of up to 5.5% and tensile strains of up to 10% [59].

Alloys containing more than 15 at.% Hf were reported to exhibit a monoclinic B19' structure for the martensite phase, similar to binary NiTi alloys. In contrast, alloys with higher Hf content transformed into an orthorhombic B19' martensitic phase, and both structures transformed

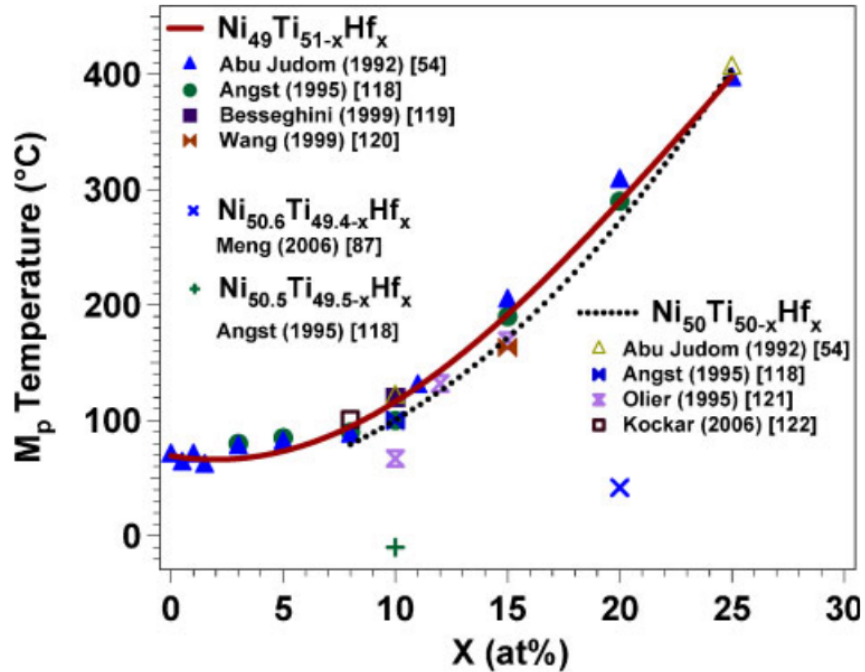


Figure 1.7 Dependence of martensite peak temperature (M_p) to the content of Hf in NiTiHf alloy system [35]

into the austenitic B2 phase [62]. NiTiHf alloys with deviations from stoichiometry were found to exhibit various phases under different thermo-mechanical processing conditions [63]. These phases can have diverse effects on the transformation characteristics and stability of the alloy. However, there is a limited availability of studies focusing on qualitative analysis of microstructure, microstructure evolution, and their overall impact on the properties of NiTiHf alloy.

The primary focus of research has been on (Ti+Hf)-rich NiTiHf alloys, primarily due to the lower TTs of Ni-rich materials. However, (Ti+Hf)-rich NiTiHf alloys suffer from several significant drawbacks. These include a large hysteresis (> 50 °C), poor ductility at room temperature, lack of cyclic stability due to high stress required for martensite reorientation and detwinning, low slip strength, and limited formability [29, 36]. In a previous study by Meng et al. [64], the tensile properties of (Ti+Hf)-rich NiTiHf alloys were investigated. It was found that no stress plateau was observed at room temperature, but rather continuous yielding with significant work hardening. This behavior can be attributed to the high resistance to martensite reorientation and the low stress required for plastic deformation. In order to increase the resistance

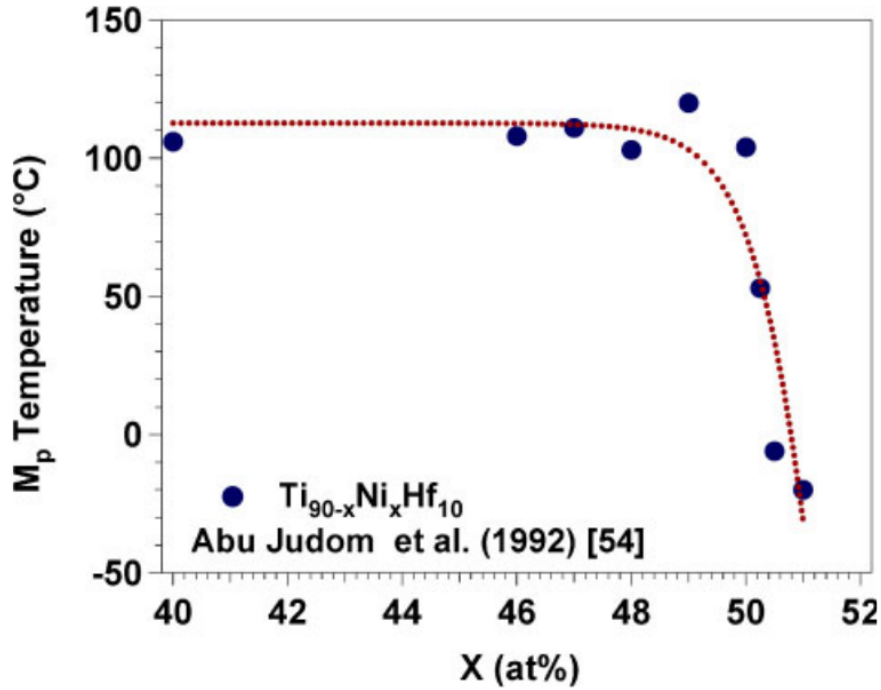


Figure 1.8 Martensite peak temperature (M_p) at different compositions of $\text{Ni}_x\text{Ti}_{90-x}\text{Hf}_{10}$ [35]

to dislocation slip, Kockar et al. [36] applied severe plastic deformation to (Ti+Hf)-rich NiTiHf alloys. Their findings revealed an increase in recoverable strain and a decrease in irrecoverable strain levels under isobaric thermal cycling experiments. Additionally, they observed improved thermal cyclic stability and reduced thermal hysteresis. However, the large thermal hysteresis prevented the observation of a reversible superelastic response [36].

There are many factors that can affect the properties of NiTiHf including alloy composition, heat treatment, precipitation, grain size, and the type of load applied (tension versus compression). These factors play a crucial role in determining the thermomechanical properties of NiTiHf alloys. Given the complex interplay of these factors, extensive research efforts are necessary to deepen our understanding of the thermomechanical properties of NiTiHf and optimize its performance for various applications.

1.3 Objectives and Technical Approach

To date, the majority of investigations on NiTiHf have focused on a limited range of compositions [65–69]. As a result, there exists a lack of comprehensive research examining

the influence of various factors on the characteristics of these HTSMAs. Given the obstacles and complexities involved in synthesizing diverse alloy compositions, computational simulations, particularly atomistic approaches, offer a valuable means to estimate and predict the material properties of novel NiTiHf alloy compositions. These simulations have demonstrated their effectiveness in terms of time and cost efficiency, making them highly beneficial in this context. Molecular dynamics (MD) is a highly effective approach in atomistic simulations, offering a comprehensive means to explore microstructural phenomena that govern the behavior of material. MD simulations are used to study the behavior and movement of atoms and molecules over time. They are widely used in various fields of science, including physics, chemistry, materials science, and biology.

The accuracy of MD simulation results is heavily reliant on the quality of interatomic potentials, which serve as the constitutive equations of MD and determine the forces and interactions between atoms. Interatomic potentials, also known as force fields, are mathematical models that describe the energy and forces associated with the arrangement of atoms in a system. The construction of interatomic potentials involves parameterizing the functional forms of the potential energy equations based on experimental data, theoretical calculations, or a combination of both. These potentials capture the effects of various interactions, such as bonded interactions (e.g., covalent bonds, bond angles, torsional angles) and non-bonded interactions (e.g., van der Waals forces, electrostatic interactions). Therefore, the development of robust interatomic potentials is critical to ensure reliable MD simulations. Thus far, no applicable interatomic potential has been specifically developed for ternary NiTiHf alloys. In this research endeavor, a Second Nearest-Neighbor Modified Embedded Atom Method (2NN MEAM) interatomic potential has been developed to accurately represent the NiTiHf ternary system, as well as its constituent binary and unary systems. This significant advancement aims to provide a robust and reliable tool for conducting simulations and investigating the properties of these alloys.

CHAPTER 2

BACKGROUND

2.1 Interatomic Potential

Computer simulations, such as atomistic simulations, play a crucial role in investigating the properties of assemblies of atoms, providing valuable insights into their structure and interactions. Simulations serve as a complementary tool to conventional experiments, allowing researchers to bridge the gap between microscopic and macroscopic scales [70]. By employing computer simulations, scientists can explore the behavior of atoms and molecules in a controlled virtual environment. Simulations enable the study of complex systems that may be challenging or even impossible to investigate experimentally. They offer a cost-effective and efficient means of exploring a wide range of conditions, materials, and scenarios. Simulations are not only used to validate existing theories and models but also serve as a testing ground for new hypotheses. The ability to compare simulation results with experimental data allows researchers to refine and improve theoretical models, expanding our understanding of the physical world. Simulations can also predict and explore phenomena that have not yet been observed experimentally, guiding future experimental design and investigation.

Atomistic simulations, in particular, focus on describing the behavior of individual atoms and molecules, taking into account their interactions and movements. These simulations consider the atoms as discrete entities, allowing for a detailed examination of their collective behavior [71]. By tracking the positions, velocities, and energies of atoms over time, atomistic simulations can reveal how materials deform, undergo phase changes, react to external stimuli, or exhibit other phenomena. The insights gained from atomistic simulations provide a connection between the atomic scale and macroscopic phenomena. By understanding how individual atoms interact and influence each other, researchers can gain a deeper understanding of the underlying mechanisms

that govern material properties and behaviors. Figure 2.1 [72] illustrates a graphical representation that compares the time scale and length scale of different simulation methods commonly employed in engineering problems.

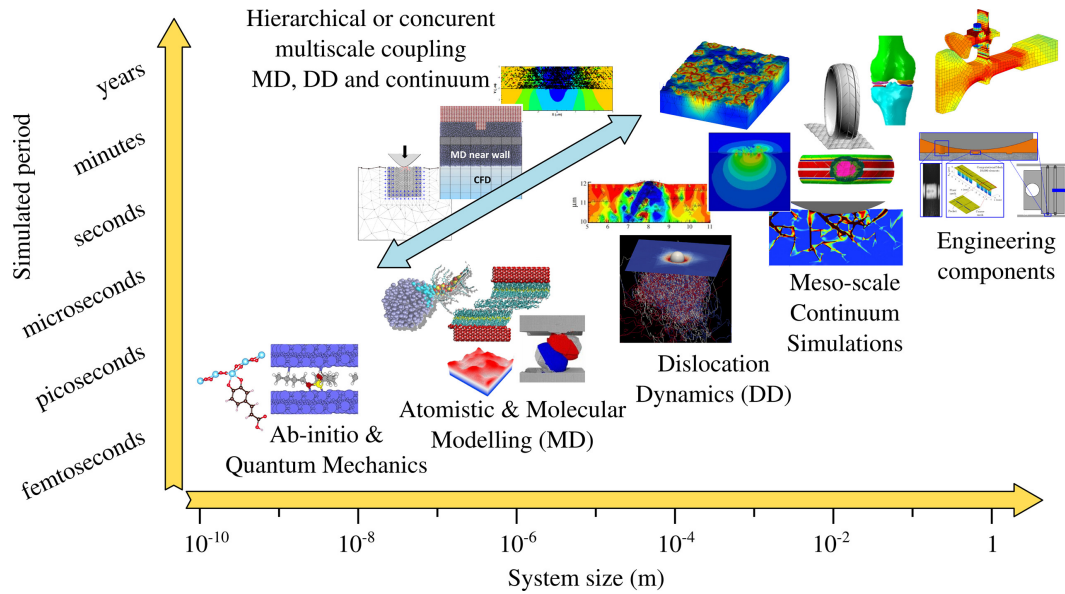


Figure 2.1 Time-versus length-scale demonstration of different simulation methods [72]

Molecular dynamics (MD) is an atomistic method used to simulate the time-dependent behavior of a system of atoms. In MD simulations, the evolution of a group of interacting atoms is tracked by integrating their equations of motion, taking into account appropriate boundary conditions that reflect the geometry or symmetry of the system being studied [73]. By simulating the motion of atoms over time, MD provides insights into the dynamic behavior and properties of materials at the atomic level. The primary data obtained from MD simulations are the positions and velocities of individual atoms as a function of time. These data allow researchers to observe the movement, interactions, and changes in atomic configurations, providing a detailed understanding of the system's behavior. By analyzing the trajectories of atoms, researchers can extract valuable information about various properties, including diffusion, structural changes, phase transitions, and thermodynamic quantities.

To perform an MD simulation, a description of the interaction potential or force field is required as input. The force field encodes the rules and parameters governing the interactions between atoms in the system. It defines the potential energy associated with different atomic configurations and determines the forces experienced by the atoms [74]. The force field incorporates terms for bonded interactions, such as bonds, angles, and dihedrals, as well as non-bonded interactions, including van der Waals forces and electrostatic interactions [74]. In constructing a model of interatomic interactions for MD simulations, it is common practice to assume a relatively straightforward and analytical functional form for the potential energy (V) of a group of atoms. These functional forms are often based on empirical or semi-empirical considerations and are chosen to strike a balance between computational efficiency and accuracy in representing the underlying physics. The accuracy and reliability of MD simulation results heavily rely on the quality of the chosen interatomic interaction potential. It is essential to parameterize the force field accurately by fitting it to experimental data or quantum mechanical calculations to ensure that it reproduces relevant properties and behavior of the system. The choice of force field also depends on the specific system being studied and the level of detail required. Consider:

$$V(\{r_i\}) \equiv V(r_1, r_2, \dots, r_N) \quad (2.1)$$

where r_i is the position vector of atom i and N is the total number of atoms. Acting force on an atom can be obtained as the negative derivative of the potential function with respect to its position:

$$f_j = -\frac{\partial V(\{r_i\})}{\partial r_j} \quad (2.2)$$

The goal is to develop approximate forms that are able to capture the maximum possible physical interatomic interactions. These ideal functions are called interatomic potentials. Typically, experimental or data from ab initio simulations are used to fit the parameters of the interatomic potential.

As the first consideration in interatomic interactions, we know that atoms cannot get too close to each other. This quantum mechanical effect should be accounted for in developing models,

by increasing the potential energy in small distance between two atoms. The "Hard-sphere" model is a simple approach that considers this short range repulsion. When the distance between two atoms becomes smaller than δ_0 (the diameter of the spheres), the energy becomes infinite:

$$V(\{R_i\}) = \sum_{i=1}^N \sum_{j=i+1}^N \phi(|R_i - R_j|) \quad (2.3)$$

where

$$\phi(r) = \begin{cases} +\infty, & r < \delta_0 \\ 0, & r \geq \delta_0 \end{cases} \quad (2.4)$$

This is shown in Figure 2.2 [75]. Apart from their short range repulsion, atoms are attracted to one another across greater distances. The Lennard-Jones (LJ) potential [76] is a well-known model that describes both long range attraction and short range repulsion between atoms:

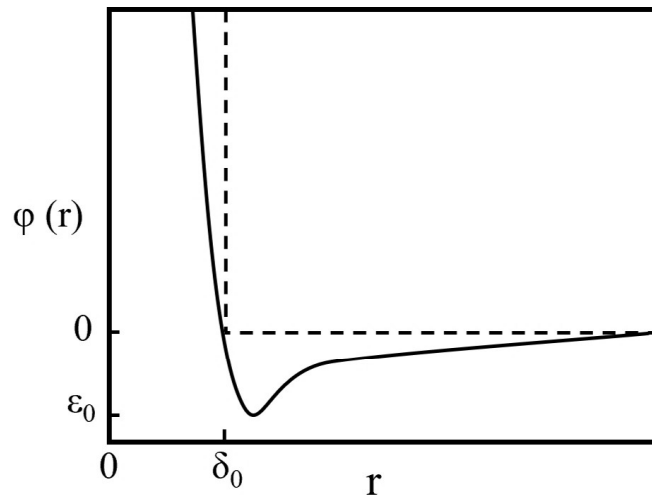


Figure 2.2 Relationship between interaction energy and atomic distance, r . Dashed line represents hard sphere model, and the solid line shows the Lennard-Jones model [75]

$$\phi(r) = 4\epsilon_0 \left[\left(\frac{r}{\delta_0} \right)^{-12} - \left(\frac{r}{\delta_0} \right)^{-6} \right] \quad (2.5)$$

The Lennard-Jones model is also presented in Figure 2.2. ϵ_0 is the depth of energy well, and $2^{1/6}\delta_0$ is the distance between atoms where the minimum interaction energy between two atoms occurs.

Two potential energy functions, which have been previously discussed, represent the energy as the cumulative effect of interactions between pairs of atoms. Such potentials are commonly referred to as pair potentials. While pair potentials are suitable for describing noble gases and ionic crystals, they do not possess the necessary accuracy for other types of solid state materials [77]. An alternative approach involves utilizing many-body potentials capable of calculating the potential energy by summing up terms from two-body interactions to N-body interactions.

$$V(\{r_i\}) = \sum_{i<j} \phi(|\mathbf{r}_i - \mathbf{r}_j|) + \sum_{i<j<k} V_3(\mathbf{r}_i, \mathbf{r}_j, \mathbf{r}_k) + \sum_{i<j<k<l} V_4(\mathbf{r}_i, \mathbf{r}_j, \mathbf{r}_k, \mathbf{r}_l) + \dots \quad (2.6)$$

The challenge of this approach is to obtain a fast convergence. In metals, bonding electrons behave differently asking for various consideration of many-body interactions. A common and popular interatomic potential for metals is the Embedded Atom Model (EAM) [78]. The functional form in EAM is:

$$V(\{r_i\}) = \sum_{i<j} \phi(|\mathbf{r}_i - \mathbf{r}_j|) + \sum_i F(\rho_i) \quad (2.7)$$

$$\rho_i = \sum_{j \neq i} f(r_{ij}) \quad (2.8)$$

In Eq. (2.7), the first term represents the pairwise interaction considering core electrons. ρ_i is the density of bonding electrons provided by the neighboring atoms of atom i . The contribution of each atom to the density field is defined by function $f(r)$. Function $F(\rho_i)$ describes the energy needed to embed atom i into a field with electron density ρ_i . There are other potentials such as Finnis-Sinclair (FS) [79] ($F(\rho) = -A\sqrt{\rho}$), Effective-Medium-Theory (EMT) [80] models and

the second-moment approximation of tight binding (TB-SMA) [81]. However, due to the non-linearity of the embedding function in EAM potentials, the description of physical properties in EAM approach is more realistic than pair potentials.

To address the shortcomings posed by EAM potentials, which are limited to face-centered cubic (fcc) elements, researchers introduced modifications to the EAM approach, resulting in the development of modified embedded atom method (MEAM) interatomic potentials. MEAM potentials have emerged as one of the most widely utilized classes of interatomic potentials in computational modeling. Baskes [82] proposed the MEAM potential as an extension of EAM by incorporating angular-dependent interactions in bonding. This addition of angular-dependent interactions expanded the scope of MEAM to encompass the modeling of body-centered cubic (bcc) structures, as well as low symmetry structures such as hexagonal close-packed (hcp), diamond-structured elements, and gaseous materials. By incorporating these angular-dependent interactions, MEAM offers a more versatile and comprehensive approach for simulating a broader range of materials and structures.

However, the utilization of MEAM in MD simulations of bcc metals revealed certain critical issues that required attention. These issues primarily appeared during the calculation of surface energy for bcc metals, specifically in cases where the calculated value for the (111) plane was found to be lower than that of the (100) plane [83], which was not in agreement with experimental information. Moreover, MD simulations on bcc metals like Fe, Mo, and Cr, showed that the most stable structure obtained was not the expected bcc phase [83]. Instead, a different structure was found to be more energetically favorable. This deviation from the anticipated bcc structure had implications for the elastic properties of these metals, as the newly obtained structure exhibited different mechanical characteristics compared to the original bcc structure. These issues cannot be resolved by merely altering the model's parameters without sacrificing accurate representations of other physical features. In MEAM formulations, only the nearest-neighbor interactions were considered by applying strong screening functions [84, 85]. However, in bcc metals, interactions of second nearest-neighbor atoms are not negligible since the second nearest-neighbor distance is just 15% larger than the first nearest-neighbor distance. The inability

of MEAM to reproduce the correct surface energies was attributed to considering only the first nearest-neighbor interactions. Lee and Baskes [83] improved the original MEAM by taking into account the second-nearest neighbor (2NN) interactions through the use of less severe many-body screening parameters. The obtained results based on the 2NN MEAM potential solved the issues with the original MEAM. In addition, it was found that for multi-component alloys containing constituents with different ground states, the 2NN MEAM potential is the most suitable form of potential for MD simulations [86]. Therefore, the method used in this study to develop a ternary NiTiHf interatomic potential was chosen as the 2NN MEAM. Following is the summary of the formalism of 2NN MEAM.

In the 2NN MEAM potential, the total energy of a multi-component alloy is approximated as

$$E = \sum_i [F_i(\bar{\rho}_i) + \frac{1}{2} \sum_{j(\neq i)} S_{ij} \phi_{ij}(R_{ij})] \quad (2.9)$$

where the embedding function is denoted as F_i and the background electron density at site i is shown as $\bar{\rho}_i$. The screening function S_{ij} and pair interaction $\phi_{ij}(R_{ij})$ are calculated between atoms i and j having the distance R_{ij} . The embedding function F_i can be written as:

$$F(\bar{\rho}) = AE_c \left(\frac{\bar{\rho}}{\bar{\rho}^0} \right) \ln \left(\frac{\bar{\rho}}{\bar{\rho}^0} \right) \quad (2.10)$$

where A is an adjustable parameter, E_c is the cohesive energy and $\bar{\rho}^0$ is the reference structure's background electron density. The background electron density $\bar{\rho}_i$ consists of contributions from spherically symmetric partial electron density as well as angular contributions (please refer to [83, 84, 87] for detailed formulations).

The energy per atom is determined for the reference structure, which is defined as having individual atoms precisely positioned on the lattice points. This calculation involves using the zero-temperature universal equation of state developed by Rose et al. [88], where the energy is

expressed as a function of the nearest-neighbor distance denoted as:

$$E^u(R) = -E_c (1 + a^* + da^{*3}) e^{-a^*} \quad (2.11)$$

where

$$a^* = \alpha \left(\frac{R}{r_e} - 1 \right) \quad (2.12)$$

$$\alpha = \left(\frac{9B\Omega}{E_c} \right)^{\frac{1}{2}} \quad (2.13)$$

in which $E^u(R)$ represents the universal function that describes a uniform expansion or contraction in the reference structure, B is the bulk modulus, Ω is the equilibrium atomic volume and E_c represents the cohesive energy of the equilibrium reference structure. Since the 2NN MEAM considers up to the second nearest-neighbor interactions, the total energy per atom in a reference structure can be calculated as:

$$E^u(R) = F(\bar{\rho}^0(R)) + \frac{Z_1}{2}\phi(R) + \frac{Z_2S}{2}\phi(aR) \quad (2.14)$$

where Z_1 and Z_2 are the number of the first and second nearest-neighbor atoms, respectively. a is the ratio of distances between the first and second nearest-neighbor atoms, and S represents the screening factor of the 2NN interactions. S and a are constant for a given reference structure. Therefore, the total energy and the embedding energy can be functions of only R . The pair potential $\phi(R)$ between two atoms having distance R between them can be obtained by equating equations (2.11) and (2.14). To do this, another pair potential $\psi(R)$ needs to be introduced:

$$E^u(R) = F(\bar{\rho}^0(R)) + \frac{Z_1}{2}\psi(R) \quad (2.15)$$

where

$$\psi(R) = \phi(R) + \frac{Z_2 S}{Z_1} \phi(aR) \quad (2.16)$$

As a result, the pair potential $\phi(R)$ can be calculated as:

$$\phi(R) = \psi(R) + \sum_{n=1} (-1)^n \left(\frac{Z_2 S}{Z_1} \right)^n \psi(a^n R) \quad (2.17)$$

The summation continues until the atomic energy of the reference structure is accurately determined.

The screening functions of the second nearest-neighbor interactions in the MEAM are less severe. Here, the effect of the neighbor atom k on the interaction between atoms i and j is denoted by S_{ij} , which is the product of the screening factors, S_{ikj} , from all neighbor atoms k :

$$S_{ij} = \prod_{k \neq i, j} S_{ikj} \quad (2.18)$$

The screening factor S_{ikj} is calculated by utilizing an ellipse that intersects atoms i , k , and j , with the orientation of the ellipse determined by atoms i and j along the x-axis.

$$x^2 + \frac{1}{C}y^2 = \left(\frac{1}{2}R_{ij} \right)^2 \quad (2.19)$$

By considering the relative distances between three i , j and k atoms, the value of C can be obtained.

$$C = \frac{2(X_{ik} + X_{kj}) - (X_{ik} - X_{kj})^2 - 1}{1 - (X_{ik} - X_{kj})^2} \quad (2.20)$$

where $X_{ik} = \left(\frac{R_{ik}}{R_{ij}}\right)^2$ and $X_{kj} = \left(\frac{R_{kj}}{R_{ij}}\right)^2$. The screening factor S_{ikj} can be obtained as a function of C :

$$S_{ikj} = f_c \left[\frac{C - C_{min}}{C_{max} - C_{min}} \right] \quad (2.21)$$

The screening range is determined by C_{min} and C_{max} where they limit the value of C . f_c represents the smooth cutoff function and is obtained as:

$$f_c(x) = \begin{cases} 1 & x \geq 1 \\ [1 - (1 - x)^4]^2 & 0 < x < 1 \\ 0 & x \leq 0 \end{cases} \quad (2.22)$$

CHAPTER 3

DEVELOPMENT OF TERNARY NITIHf MEAM POTENTIAL

3.1 Methodology

Interatomic potentials play a crucial role in atomistic simulations by governing the interactions between atoms based on their positions. The accuracy of the employed potential greatly influences the reliability of MD simulation results, as it determines the system's potential energy. Since the MEAM formulation is empirical, it is important to enhance its physical foundation by calibrating its parameters to match with material properties obtained from experiments or computed through lower length scale analysis [89]. This study utilizes the density functional theory method [90] at a lower length scale to accurately determine the bulk material properties [91]. When calibrating the parameters of the MEAM potential for an alloy system, the introduction of a new element alters the electron density, necessitating a new calibration procedure for each new alloy system [92]. To calibrate a ternary 2NN MEAM potential for NiTiHf, all constituent unary and binary systems are required. Hence, unary MEAM potentials for Ni, Ti, and Hf, along with binary MEAM potentials for HfNi, HfTi, and NiTi, are essential. In this study, all the aforementioned MEAM potentials were calibrated, with the exception of the Hf unary MEAM potential, which was adopted from the work of Huang et al. [93].

3.2 Density Functional Theory

Density Functional Theory (DFT) is a powerful computational method used in physics, chemistry, and materials science to study the electronic structure and properties of atoms, molecules, and solids. It provides a way to calculate the behavior of electrons in a material system by approximating the many-body quantum mechanical problem in terms of the electron density. The foundation of DFT is the Hohenberg-Kohn theorems [94], which state that the ground-state electronic properties of a system are uniquely determined by its electron density. This means that

instead of solving the complicated many-electron Schrödinger equation, DFT focuses on finding the ground-state electron density that minimizes the total energy of the system. In DFT, the electronic structure problem is formulated as an energy functional of the electron density. The Kohn-Sham equations are solved iteratively to obtain self-consistent solutions for the electron density and the corresponding electronic energy. These equations introduce a set of fictitious non-interacting electrons, called Kohn-Sham orbitals, that reproduce the same electron density as the real interacting system. The exchange-correlation functional is a crucial component of DFT as it accounts for the electronic exchange and correlation effects, which arise from the quantum mechanical behavior of electrons [95]. Various approximations exist for the exchange-correlation functional, ranging from simple local density approximations to more accurate gradient-corrected and hybrid functionals. DFT has a wide range of applications. It can be used to predict and understand the properties of molecules, such as their structures, energies, and spectra. It is also employed in the study of materials, including the calculation of electronic band structures, lattice vibrations, and magnetic properties [96]. Additionally, DFT plays a crucial role in guiding experimental investigations, interpreting spectroscopic data, and designing new materials with tailored properties.

3.3 Calibration of Unary MEAM Potentials (Ni, Ti)

Quantum ESPRESSO suite [97] was utilized to conduct DFT simulations, aiming to acquire material properties essential for calibrating unary MEAM potentials for Ni and Ti. Various properties such as the energy-volume curve, cohesive energy, bulk modulus, elastic constants, vacancy formation energy, and surface formation energy were calculated through DFT simulations. Subsequently, the MEAM potential was calibrated to accurately replicate these properties when employed in an MD simulation. To find the unary potential parameters, MEAM Potential Calibration (MPC) tool [91] was employed.

For DFT simulations, the widely used Projector Augmented Wave (PAW) pseudopotentials were employed in combination with the Perdew-Burke-Ernzerhof (PBE) generalized gradient approximation for the exchange correlation functional. These pseudopotentials allowed for an accurate description of the interaction of the valence electrons, and taking into account the

shielding effect of the core electrons. To ensure an accurate representation of the electronic structure and properties of the system, the Brillouin zone sampling was performed using the Monkhorst-Pack scheme. This scheme divides the Brillouin zone into discrete points or k-points to obtain an average over the reciprocal space. The choice of Brillouin zone k-point sampling was determined through a sensitivity analysis. By evaluating the response of the calculated properties to different k-point meshes, a $12 \times 12 \times 12$ mesh was selected that provided a good balance between accuracy and computational efficiency. In addition to the sampling scheme, a Fermi-level smearing of 0.03 eV was applied using the Methfessel-Paxton method. This smearing technique helps to account for temperature effects and provides a more realistic description of the electronic behavior. To determine the optimum energy cutoff value (*ecut*) for the plane-wave basis set, the convergence rate and the sensitivity of the results to *ecut* were considered. By systematically varying the *ecut* value and observing the convergence behavior of the calculated properties, the *ecut* values that yielded reliable and accurate results were identified.

The procedure of MEAM potential calibration consists of two steps. At the first step which is called the global approach, the parameter space of MEAM potential is coarsely refined. This step starts with guessing the MEAM potential parameters and continues by performing sensitivity analysis for parameters. The second step which is called the local approach, is for the evaluation of sensitive parameters, sampling parameter space and generation of analytical models for optimization of the potential.

The fitting of MEAM parameters to experimental and first principles data incorporates different target properties. Some of these properties, such as energy-volume curves for various lattices and elastic constants, are fundamental to the MEAM formalism and are essential targets that should always be included. Other properties, such as surface energies, contribute to obtaining reasonable results for specific aspects of physical properties. The first physical property to start the calibration with is the energy variation. Energy variation with respect to the volume or nearest neighbor distance is also used to check the validity of the potential. For the unary systems of Ni and Ti, the energy-volume correlation in different crystal structures was obtained. In the beginning, the most stable lattice structure that was reported in the experiments was chosen for each material and

referred to as the primary structure. Two alternative lattice structures were referred to as secondary structures. The calibration outputs were derived from the raw simulation data using the following procedure. Firstly, the energy in the energy-volume curve was divided by the number of atoms to obtain the energy per atom values. Subsequently, interpolation techniques were employed, utilizing a Birch-Murnaghan equation of state [98], to determine the cohesive energy and relaxed volume. Furthermore, the lattice parameter and atomic radius were derived from the relaxed volume using basic lattice-dependent formulas that establish relationships between the lattice parameter, atomic radius, and volume. In Figure 3.1 and 3.2, the energy versus lattice parameter curves generated by the unary potentials for Ni and Ti are presented, respectively.

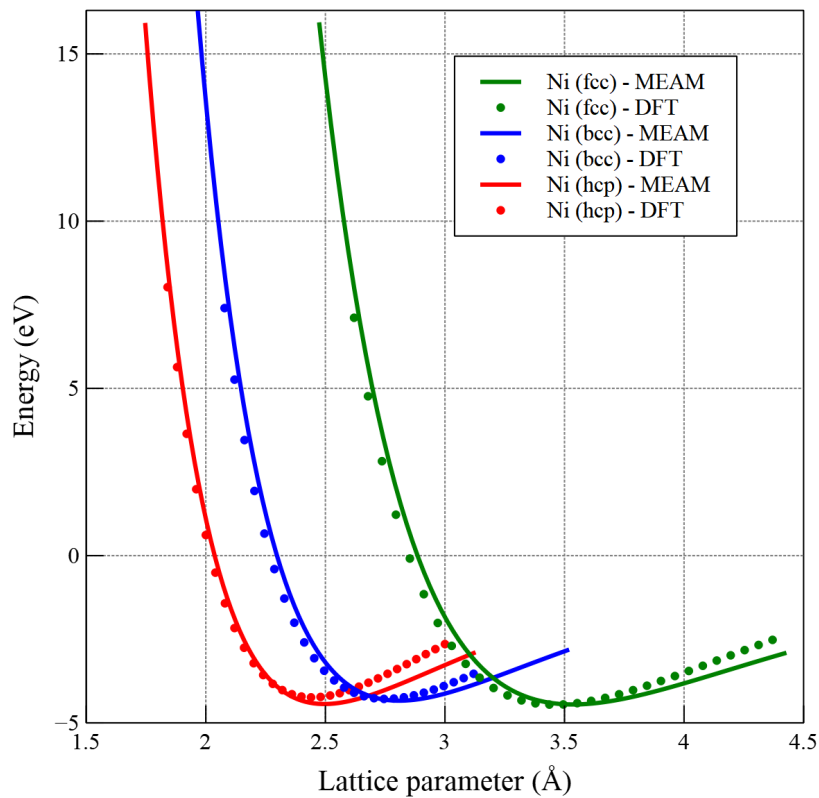


Figure 3.1 Energy versus lattice parameter curves of Ni obtained via DFT and the developed MEAM potential

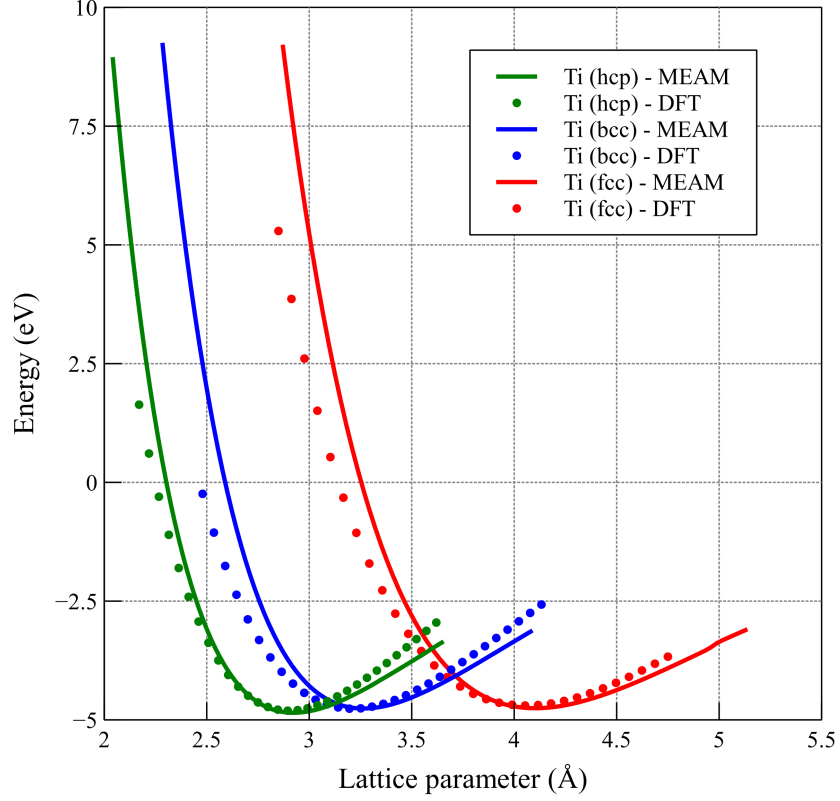


Figure 3.2 Energy versus lattice parameter curves of Ti obtained via DFT and the developed MEAM potential

The data was also utilized to calculate the bulk modulus. The values of the elastic constants were derived using the following equation [29]:

$$E(e_i) = E_C - P(V)\Delta V + VC_{ij}e_i e_j / 2 + O(e_i^3) \quad (3.1)$$

Based on equation 3.1, e represents the strain tensor and C represents the stiffness in using Voigt notation. E_C stands for the cohesive energy, while $E(e_i)$ denotes the energy per atom for a given strain. V corresponds to the volume per atom, and $P(V)$ represents the pressure, which can be expressed as the trace of the stress, thereby involving the contraction of the stiffness tensor and the strain. When the strain components tend towards zero, the contribution of higher order terms ($O(e_i^3)$) becomes negligible. Consequently, the stiffness values can be determined based on the energy of the cell for a given strain. To accurately depict the curvature proportionate

to each elastic constant, energies were obtained for small positive and negative strain values in addition to the equilibrium energy. The equilibrium volume was determined using the Murnaghan equation of state, although the energies for both equilibrium and strained configurations were directly calculated rather than relying on the equation of state. The strain values can be adjusted to incorporate the requirements of different materials.

The vacancy formation energy (E_f^{vac}) was computed as the energy variation resulting from breaking the bonds of one atom from the bulk material [99]. It should be noted that due to the consideration of periodic boundary conditions, a large number of atoms should be modeled in the simulation to prevent interactions between the vacancy and its periodic images. The specific size of our simulations depends on the lattice type, but as a general guideline, we simulated over 100 atoms to accurately determine the vacancy energy:

$$E_f^{vac} = E_{tot}^{vac} - \frac{N-1}{N} E_{tot}^{bulk} \quad (3.2)$$

where E_{tot}^{vac} is the energy of the system with a single vacancy, E_{tot}^{bulk} is the energy of the perfect bulk system, and N is the number of atoms in the bulk system. To determine the surface energy of the (hkl) plane, denoted as E_{hkl} , a commonly used approach known as the slab model [100] was utilized. In this method, a supercell incorporating the desired surface (specified by the hkl Miller indices) is generated. To introduce a vacuum region, atoms are selectively removed from one half of the supercell. By employing this configuration, the surface energy E_{hkl} can be calculated using the following formula:

$$E_{hkl} = \frac{E_{slab}^{hkl} - E_{bulk}^{hkl} \times n_{slab}}{2 \times A_{slab}} \quad (3.3)$$

where E_{slab}^{hkl} represents the total energy of the slab system, while E_{bulk}^{hkl} corresponds to the energy per atom of the bulk system. The parameter n_{slab} denotes the total number of atoms in the slab structure, and A_{slab} represents the surface area of the slab structure. The factor of 2 is included to account for the presence of two surfaces within the slab model. According to literature [100], it is recommended to maintain a minimum slab thickness of 10 Å in order to minimize interactions

between the two surfaces of the slab. By ensuring an adequate separation between the surfaces, the potential effects of surface interactions can be effectively mitigated.

The 2NN MEAM formalism for a pure unary element involves fourteen independent model parameters [83, 89], as outlined in Table 3.1. Among these parameters, four are associated with the universal equation of state i.e. cohesive energy (E_c), equilibrium nearest-neighbor distance (r_e), bulk modulus (B) of the reference structure, and the adjustable parameter d [89]. The electron density is described by seven parameters: decay lengths ($\beta^{(0)}, \beta^{(1)}, \beta^{(2)}, \beta^{(3)}$), and weighting factors ($t^{(1)}, t^{(2)}, t^{(3)}$) [89]. Additional parameters include the embedding function adjustable parameter A , and screening parameters C_{min} and C_{max} . The screening parameters are used to account for the many-body interactions between atoms in a material. These parameters represent the minimum and maximum cutoff distance for many-body interactions. They determine the range over which many-body interactions are significant. At distances below C_{min} , the many-body interactions are considered to have a significant contribution. At distances beyond C_{max} , the many-body interactions are assumed to have a negligible contribution.

In each iteration of parameter calibration, the accuracy of the current parameter set was assessed by calculating the physical properties of Ni and Ti based on the new MEAM parameters and comparing them with the results obtained from DFT. The final calibrated parameters for the unary 2NN MEAM potentials of Ni and Ti, as well as the parameters for the Hf MEAM potential developed by Huang et al. [93], are presented in Table 3.1. It is worth mentioning the primary crystal structures considered for Ni and Ti were fcc and hcp, respectively. Furthermore, the G (Gamma) function, with $G = 2/(1 + e^{-\gamma})$, was chosen for the calculation of the electron density.

In the calibration process, two influential parameters, namely the cohesive energy (E_c) and equilibrium nearest-neighbor distance (r_e), had a significant impact on all properties, particularly the energy-volume curves. Additionally, other parameters exhibited noticeable and direct effects on specific properties as follows: $t^{(2)}$ directly influenced C_{44} ; $\beta^{(0)}$ and $t^{(3)}$ affected the energy per atom of secondary structures; $\beta^{(2)}$ and $t^{(1)}$ influenced values such as vacancy formation energy, surface energies, and C_{44} .

Table 3.1 Parameters of the unary MEAM potentials for Ni, Ti, and Hf. E_c (eV/atom) is the cohesive energy; r_e (Å) is the equilibrium nearest-neighbor distance; B (GPa) is the bulk modulus. All other parameters are dimensionless

	Ni	Ti	Hf ^a
E_c	4.45	4.75	7.33
r_e	2.50	2.83	3.17
B	194	114	113
A	0.82	0.28	0.79
$\beta^{(0)}$	2.63	2.25	2.23
$\beta^{(1)}$	2.30	3.90	2.82
$\beta^{(2)}$	1.50	1.20	3.73
$\beta^{(3)}$	1.00	3.40	2.06
$t^{(1)}$	5.00	-5.00	2.98
$t^{(2)}$	1.00	-28.00	1.92
$t^{(3)}$	3.20	-44.00	-6.24
C_{min}	0.98	0.30	0.66
C_{max}	1.60	1.70	2.28
d	0.05	0.00	-0.02, -0.08

^aRef. [93]

However, it is important to note that calibrating MEAM parameters is a complex procedure, and establishing a direct one-to-one correlation between each parameter and a specific material property is not feasible. Table 3.2 presents the computed physical properties and their corresponding values using the developed MEAM potential, along with those obtained from DFT and previous experimental studies, for Ni and Ti. The results demonstrate that the physical properties obtained with the developed unary MEAM potentials correlate with the results from DFT and experiments, except for the surface energy of Ni in the (100) plane, $E_{(100)}^{(surf)}$, which exhibits

a 22% overestimation compared to the DFT result. Hence, the calibrated unary MEAM potentials successfully replicate the material's physical properties.

3.4 Calibration of Binary MEAM Potentials (NiTi, HfNi and HfTi)

To calibrate a ternary MEAM potential, it is generally necessary to first calibrate binary MEAM potentials. Calibrating binary MEAM potentials involves determining the appropriate parameter values for two elements, typically denoted as Element A and Element B. This calibration process involves fitting the MEAM potential to reproduce various physical properties and behaviors of the binary alloy formed by Elements A and B. Once the binary MEAM potentials for Elements A and B are calibrated and validated against experimental data or DFT results, they can serve as a foundation for developing ternary MEAM potentials.

In addition to the parameters used for unary potentials, each binary system's MEAM potential requires thirteen additional independent parameters. These parameters serve specific purposes in defining the potential for the binary system. Here is an overview of the thirteen additional parameters:

- **Equation of State Parameters:** The equation of state parameters include the cohesive energy (E_c), equilibrium nearest-neighbor distance (r_e), and two parameters (α and d) related to the equation of state. These parameters determine the overall energy and bonding behavior of the binary system.
- **Screening Factors (C_{min} and C_{max}):** There are four parameters for C_{min} and four parameters for C_{max} , which are many-body screening factors. These factors account for the interactions between atoms in the binary system and control the range and strength of these interactions.
- **Atomic Electron Density Scaling Factor (ρ_0):** The atomic electron density scaling factor (ρ_0) is the final parameter. It scales the electron density contribution to the energy and determines the strength of the electron density term in the MEAM potential.

The calibration and optimization of MEAM parameters were carried out with the aim of obtaining material properties consistent with both DFT calculations and experimental data available in the literature. Various properties were taken into account during the calibration

Table 3.2 The physical properties of Ni and Ti, including their calculated values using both DFT and the developed MEAM potentials, as well as their corresponding experimental values. Cohesive energy is denoted as E_c (eV/atom); a and c (Å) denote the lattice constants; B is the bulk modulus and C_{11} , C_{12} , C_{13} , C_{33} and C_{44} (GPa) are the elastic constants; E_f^{vac} (eV) denote the vacancy formation energy; and $E_{(111)}^{(surf)}$, $E_{(110)}^{(surf)}$, $E_{(100)}^{(surf)}$, $E_{(0001)}^{surf}$, $E_{(10\bar{1}0)}^{surf}$, $E_{(10\bar{1}1)}^{surf}$ and $E_{(2\bar{1}\bar{1}2)}^{surf}$ (mJ/m²) represent the surface energies

Property	Ni			Ti		
	Exp.	DFT ^g	MEAM ^g	Exp.	DFT ^g	MEAM ^g
E_c	4.440 ^a	4.453	4.450	4.850 ^a	4.806	4.779
a	3.520 ^b	3.510	3.540	2.951 ^h	2.895	2.925
c	-	-	-	4.679 ^h	4.632	4.680
B	190.3 ^c	190.6	193.9	109.7 ⁱ	110.5	114.1
C_{11}	253 ^d	247	275	176.1 ⁱ	182.0	178.5
C_{12}	152 ^d	173	153	86.9 ⁱ	67.0	85.3
C_{13}	-	-	-	68.3 ⁱ	65.0	73.2
C_{33}	-	-	-	190.5 ⁱ	204.0	195.6
C_{44}	124 ^d	111	115	50.8 ⁱ	57.0	52.4
E_f^{vac}	1.73 ^e	1.81	1.97	1.50 ^j	1.61	1.44
$E_{(111)}^{(surf)}$		1920	2216	-	-	-
$E_{(110)}^{(surf)}$		2290	2607	-	-	-
$E_{(100)}^{(surf)}$	2240 ^f	2210	2703	-	-	-
$E_{(0001)}^{surf}$	-	-	-	1920 ^f	1987	1748
$E_{(10\bar{1}0)}^{surf}$	-	-	-		2067	1815
$E_{(10\bar{1}1)}^{surf}$	-	-	-		1970	2170
$E_{(2\bar{1}\bar{1}2)}^{surf}$	-	-	-		2083	2120

Note: The table includes data for both fcc Ni and hcp Ti that have distinct quantities and indices. Cells filled with a "dash" indicate that the corresponding information is not applicable (n/a). ^aRef. [101]; ^bRef. [102]; ^cRef. [103]; ^dRef. [104]; ^eRef. [105]; ^fRef. [106]; ^gPresent study; ^hRef. [107]; ⁱRef. [108]; ^jRef. [109].

process, including lattice constants, formation energy (ΔE_f), elastic constants, and cohesive energy. In the case of developing the NiTi potential, the initial starting point for the calibration process was the NiTi MEAM potential proposed by Ko et al. [110]. This existing potential served as the initial guess, providing a foundation for further refinement and optimization of the parameters to accurately describe the properties of the NiTi system.

By comparing the predictions of the initial binary MEAM potentials with the target properties obtained from DFT calculations and experimental data, adjustments and optimizations of the parameters were made iteratively. The calibration process aimed to achieve a good agreement between the predicted properties using the MEAM potential and the reference data. This iterative optimization process ensures that the developed binary potentials better capture the behavior and properties of the binary alloys. In the case of NiTi, the B2 crystal structure, known for its thermodynamic stability [13], was chosen as the reference structure during the calibration process. Similarly, for HfNi and HfTi systems, the cohesive energy calculations in this study led to the identification of specific reference crystal structures. In the case of HfNi, the B2 structure was considered as the reference structure, and for HfTi, the L12 structure was chosen as the reference structure, indicating its stability based on cohesive energy calculations.

The formation energy and lattice parameters of the system were primarily influenced by two MEAM parameters, E_c and r_e . The screening parameters were calibrated to achieve the best fit for the elastic constants. The calibrated parameters for the 2NN MEAM potentials of HfNi, HfTi, and NiTi are presented in Table 3.3. To assess the reliability of the obtained MEAM potentials, the computed lattice parameters, formation energy, and elastic constants of the three binary alloys were compared with the corresponding results obtained from DFT. The details of this comparison are provided in Table 3.4. The comparison in Table 3.4 reveals a general agreement between the results obtained using the developed binary MEAM potentials and those obtained from DFT. However, there are a couple of discrepancies, including an underestimation of C_{11} in HfNi and an overestimation of C_{44} in NiTi, when compared to the DFT values.

Table 3.3 Parameters of the binary MEAM potentials for HfNi, HfTi and NiTi. E_c (eV/atom) is the cohesive energy; r_e (Å) is the equilibrium nearest-neighbor distance. All other parameters are dimensionless

Parameter	Binary Alloy		
	HfNi	HfTi	NiTi
Ref. structure	B2	L12	B2
E_c	6.40	5.90	4.96
r_e	2.720	3.025	2.612
α	5.00	5.47	4.46
d	0.025	0.000	0.025
$\rho_0^A : \rho_0^B$	1 : 1	1 : 1	1 : 1
$C_{min}(i-i-j)$	0.40	0.40	0.20
$C_{min}(j-j-i)$	0.67	0.25	0.06
$C_{min}(i-j-i)$	0.60	0.40	0.60
$C_{min}(j-i-j)$	0.40	0.60	0.60
$C_{max}(i-i-j)$	2.80	1.90	1.70
$C_{max}(j-j-i)$	1.70	1.80	1.70
$C_{max}(i-j-i)$	1.90	1.90	1.80
$C_{max}(j-i-j)$	1.80	1.70	1.90

3.5 Calibration of Ternary MEAM Potential (NiTiHf)

To develop the ternary NiTiHf MEAM potential, a set of six additional screening parameters is necessary. These parameters, specifically three $C_{min}(i-k-j)$ and three $C_{max}(i-k-j)$, supplement the existing parameters used for unary and binary potentials. The purpose of the $C_{min}(i-k-j)$ and $C_{max}(i-k-j)$ parameters is to describe how the interaction between two neighboring atoms (i and j) is influenced or screened by the presence of a third element atom (k). These screening parameters play a crucial role in accurately capturing the behavior of the ternary alloy. In the ternary system of Ni-Hf-Ti, six parameters are designated as $C_{min}(Hf-Ni-Ti)$,

Table 3.4 The physical properties of HfNi, HfTi and NiTi, including their calculated values using both DFT and the developed MEAM potentials. a (Å) denotes the lattice constant; ΔE_f (eV/atom) is the formation energy; C_{11} , C_{12} and C_{44} (GPa) are the elastic constants

Property	B2 HfNi		L12 HfTi		B2 NiTi	
	DFT	MEAM ^c	DFT	MEAM ^c	DFT	MEAM ^c
a	3.023 ^a	3.148	4.317 ^a	4.289	3.040 ^d	3.008
ΔE_f	-0.519 ^b	-0.510	0.000 ^b	0.000	-0.396 ^b	-0.428
C_{11}	540 ^a	391	195 ^a	201	183 ^e	153
C_{12}	122 ^a	127	123 ^a	149	146 ^e	122
C_{44}	88 ^a	101	86 ^a	105	46 ^e	80

^aRef. [111]; ^bRef. [112]; ^cPresent study; ^dRef. [113]; ^eRef. [114];

$C_{min}(Hf - Ti - Ni)$, $C_{min}(Ni - Hf - Ti)$, $C_{max}(Hf - Ni - Ti)$, $C_{max}(Hf - Ti - Ni)$, and $C_{max}(Ni - Hf - Ti)$ as shown in Figure 3.3.

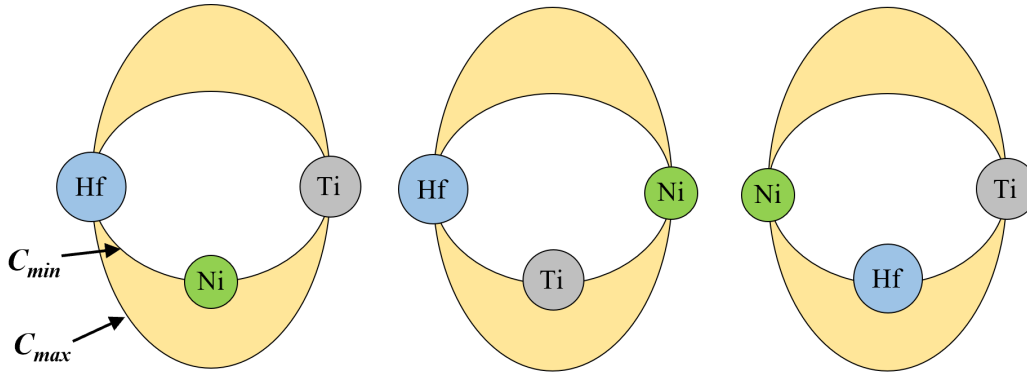


Figure 3.3 Three scenarios of depicting the screening of interactions between two adjacent atoms of different types by a third atom in the Ni-Ti-Hf ternary system

Because of the challenge in obtaining sufficient data for confirming the ternary potential parameters, the approach used to develop interaction potential parameters for binary systems is typically not directly applicable to ternary systems. However, [115] introduced an alternative approach that utilizes an averaging concept to derive the 2NN MEAM potential parameters

specifically for ternary systems. The formulations of this method are as following:

$$C_{min}(i-j-k) = \left[0.5 \left(C_{min}^{i-j-i} \right)^{\frac{1}{2}} + 0.5 \left(C_{min}^{k-j-k} \right)^{\frac{1}{2}} \right]^2, \quad (3.4)$$

$$C_{min}(i-k-j) = \left[0.5 \left(C_{min}^{i-k-i} \right)^{\frac{1}{2}} + 0.5 \left(C_{min}^{j-k-j} \right)^{\frac{1}{2}} \right]^2, \quad (3.5)$$

$$C_{min}(j-i-k) = \left[0.5 \left(C_{min}^{j-i-j} \right)^{\frac{1}{2}} + 0.5 \left(C_{min}^{k-i-k} \right)^{\frac{1}{2}} \right]^2, \quad (3.6)$$

$$C_{max}(i-j-k) = \left[0.5 \left(C_{max}^{i-j-i} \right)^{\frac{1}{2}} + 0.5 \left(C_{max}^{k-j-k} \right)^{\frac{1}{2}} \right]^2, \quad (3.7)$$

$$C_{max}(i-k-j) = \left[0.5 \left(C_{max}^{i-k-i} \right)^{\frac{1}{2}} + 0.5 \left(C_{max}^{j-k-j} \right)^{\frac{1}{2}} \right]^2, \quad (3.8)$$

$$C_{max}(j-i-k) = \left[0.5 \left(C_{max}^{j-i-j} \right)^{\frac{1}{2}} + 0.5 \left(C_{max}^{k-i-k} \right)^{\frac{1}{2}} \right]^2. \quad (3.9)$$

However, in this study in order to determine suitable values for these parameters, numerous MD simulations of the NiTiHf model were conducted. Through these simulations, the behavior of the ternary alloy at both high and low temperatures was observed. Specifically, the focus was on achieving the desired characteristics of the alloy, such as high-temperature superelasticity and low-temperature martensitic behavior. The calibrated parameters of the ternary MEAM potential are presented in Table 3.5. In order to incorporate second-nearest neighbor interactions into the potential model, a radial cutoff distance needs to be defined for atomistic simulations. This cutoff distance should be chosen such that it lies between the distances corresponding to the second and third nearest neighbors. After calibrating the ternary MEAM potential, a radial cutoff distance of 5.0 Å was determined to be sufficiently large for accurately reproducing the mechanical properties and phase transformations of the system. This means that during simulations, interactions between atoms beyond this distance are neglected as they are considered negligible for the desired outcomes.

3.6 Calculation of Lattice Parameters Using the Developed MEAM Potential

The predominant crystal structure of the NiTiHf alloy is known to be cubic B2 in the austenite phase, while it transforms into a monoclinic B19' structure in the martensite phase

Table 3.5 Parameters of the ternary MEAM potential for NiTiHf

Parameter	Ni-Ti-Hf
$C_{\min}(\text{Hf} - \text{Ni} - \text{Ti})$	0.10
$C_{\min}(\text{Hf} - \text{Ti} - \text{Ni})$	1.10
$C_{\min}(\text{Ni} - \text{Hf} - \text{Ti})$	0.15
$C_{\max}(\text{Hf} - \text{Ni} - \text{Ti})$	1.90
$C_{\max}(\text{Hf} - \text{Ti} - \text{Ni})$	2.60
$C_{\max}(\text{Ni} - \text{Hf} - \text{Ti})$	1.90

[116]. To validate the accuracy and transferability of the developed MEAM potential in accurately reproducing the alloy's physical properties under different conditions from the calibration, MD simulations were performed to determine the lattice constants of NiTiHf with varying compositions in both the austenitic B2 and martensitic B19' structures, utilizing the developed MEAM potential. These results were then compared to experimental values [59] for each lattice constant.

In this analysis, Ni-rich alloys with different Hf contents were considered. Specifically, different alloy compositions were modeled using $\text{Ni}_{50}\text{Ti}_{50-x}\text{Hf}_x$ formula where x ranges from 0 to 25. For each composition of interest, a supercell consisting of 2000 atoms was constructed with the associated crystal structure. During the simulation, models underwent energy minimization using a box relaxation procedure, allowing for the calculation of the lattice constants. The obtained results from the MEAM potential were then compared to the experimental data, as shown in Figure 3.4. In this graph, the lattice parameter of the cubic austenitic B2 phase was denoted as " a_0 ." This parameter signifies the length of the lattice vectors defining the cubic structure. On the other hand, the lattice parameters (a , b , c) and the monoclinic angle (β) were used to characterize the B19' martensitic structure. These parameters are represented in the inset of Figure 3.4, which provides a schematic representation of the B2 and B19' structures for better understanding.

Figure 3.4 demonstrates that the computed values of the lattice constants obtained using the developed MEAM potential align well with the experimental values. Additionally, an increasing trend in lattice constants was observed at higher Hf contents. Furthermore, the formation energy

of four different compositions of NiTiHf with B2 and B19' structures was calculated using both DFT and the developed MEAM potential. The results of this comparison are presented in Table 6, indicating good agreement between the MEAM potential and DFT results.

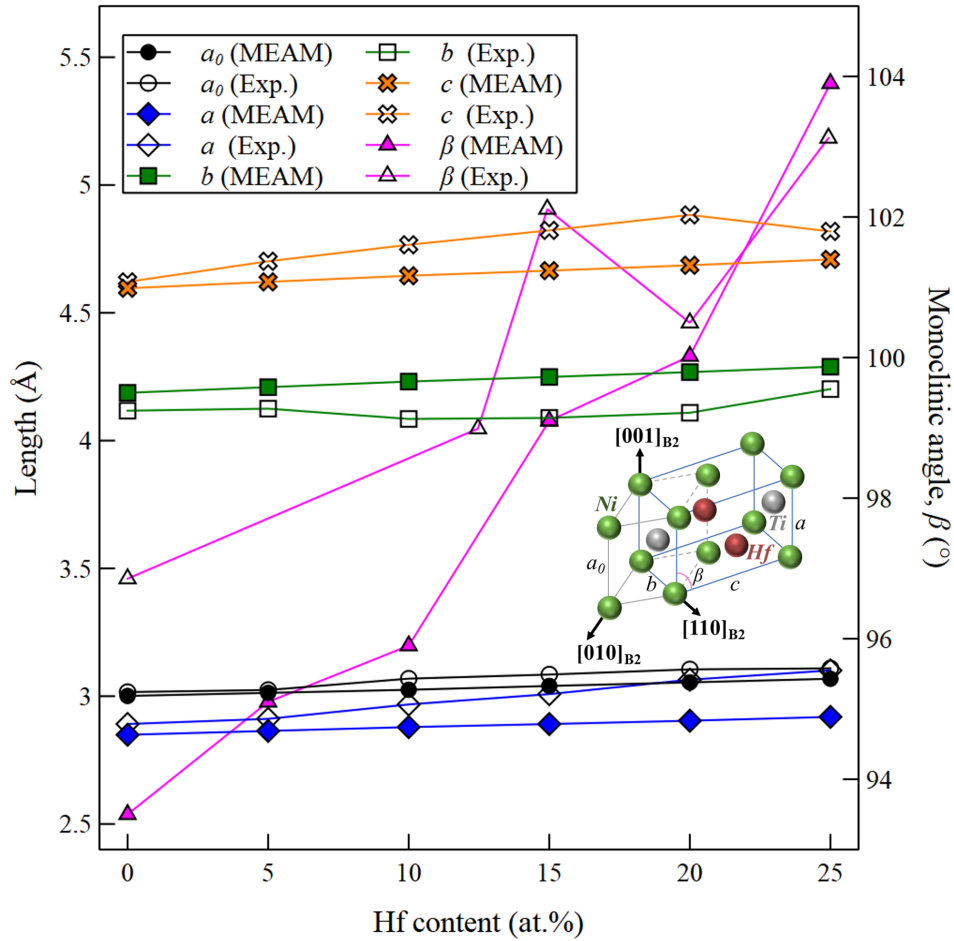


Figure 3.4 Comparison of experimental lattice constants of B2 and B19' structures of NiTiHf with varying Hf content, with calculated lattice constants using the developed MEAM potential

3.7 Simulation of the Temperature- and Stress-induced Phase Transformation

The thermomechanical behavior of NiTiHf HTSMA is a topic of great importance. Understanding how this material behaves under different temperature and stress conditions is

Table 3.6 Formation energy (ΔE_f (eV/atom)) of B2 and B19' structures of various compositions of NiTiHf calculated by DFT and developed MEAM Potential

Structure	Property	Composition	DFT	MEAM
B2	ΔE_f	Ni ₅₀ Ti _{43.75} Hf _{6.25}	-0.386	-0.369
		Ni ₅₀ Ti _{37.5} Hf _{12.5}	-0.369	-0.328
		Ni ₅₀ Ti _{31.25} Hf _{18.75}	-0.342	-0.289
		Ni ₅₀ Ti ₂₅ Hf ₂₅	-0.336	-0.283
B19'	$E - E_{B2}$	Ni ₅₀ Ti _{43.75} Hf _{6.25}	-0.042	-0.035
		Ni ₅₀ Ti _{37.5} Hf _{12.5}	-0.034	-0.030
		Ni ₅₀ Ti _{31.25} Hf _{18.75}	-0.031	-0.024
		Ni ₅₀ Ti ₂₅ Hf ₂₅	-0.027	-0.016

crucial for its practical applications. Two significant factors that influence its behavior are the temperature-induced and stress-induced martensitic phase transformations. The temperature-induced phase transformation is particularly important since the transformation temperatures can be obtained through it. Hence, the developed MEAM potential was used to study the martensitic phase transformation of NiTiHf. MD simulations were initially employed to explore the temperature-induced phase transformations in Ni_{50.3}Ti_{29.7}Hf₂₀, which is a frequently utilized composition of the ternary alloy. This composition has demonstrated significant promise for its potential application as an HTSMA [68, 117].

The LAMMPS molecular dynamics code [118] was utilized to conduct MD simulations, employing a timestep of 2 fs. To generate B2 austenitic single-crystal models of Ni_{50.3}Ti_{29.7}Hf₂₀, the software tool ATOMSK [119] was employed. In order to create models of NiTiHf with the desired composition, initially, an equiatomic NiTi box model with $155 \times 155 \times 155$ Å dimensions that contained 250,000 atoms was constructed. Then, to achieve the desired composition of NiTiHf, a specific number of Ti atoms within the equiatomic NiTi box were randomly selected for replacement with Hf atoms. The number of Ti atoms replaced corresponded to the desired composition of the final NiTiHf alloy. It's important to note that during this replacement process,

the energy changes associated with the atom substitutions were not considered. Instead, the focus was primarily on achieving the desired atomic ratio. Following the replacement of Ti atoms with Hf atoms, the resulting distribution of atoms within the model was visually inspected and analyzed. This visual investigation aimed to identify any potential formation of blocks or clusters consisting predominantly of Hf atoms. Such formations could indicate an uneven or non-homogeneous distribution of Hf within the model, which would not accurately represent the desired NiTiHf composition. To mitigate surface effects and create a more realistic simulation environment, periodic boundary conditions were implemented in all directions. This approach ensures that the atoms within the system interact as if they were part of an infinite lattice, reducing any potential influence from the edges of the model. In Figure 3.5, NiTiHf modeled box and its dimensions are presented.

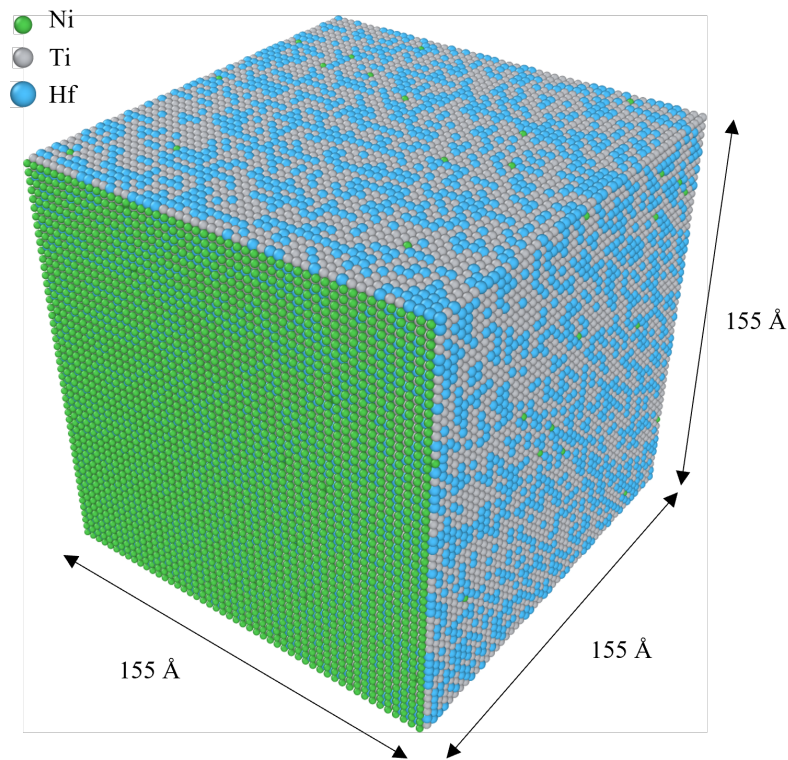


Figure 3.5 Simulated $\text{Ni}_{50.3}\text{Ti}_{29.7}\text{Hf}_{20}$ model and its dimensions

To maintain precise control over the temperature and pressure parameters, the Nose-Hoover style thermostating and barostating methods were applied on all atoms, respectively. These techniques were employed to regulate the temperature and pressure experienced by each atom within the system. To investigate the temperature-induced phase transformation, a cyclical process of cooling and heating was applied on the model under zero pressure conditions. Prior to any temperature alteration, the model underwent an equilibration phase using the isobaric-isothermal NPT ensemble, maintaining a pressure of zero at a temperature of 900 °C. Subsequently, the model was cooled gradually from 900 °C to -100 °C and then heated back to 900 °C, both at a controlled rate of ± 2.75 °C/ps. This stepwise cooling and heating process allowed for a systematic exploration of the temperature-dependent phase transformations in the material. Figure 3.6 illustrates the variation of the rate of martensitic transformation in the NiTiHf model as a function of temperature. The calculation of the martensitic transformation rate involved determining the fraction of martensite at each step of the simulation. In this graph, the abrupt jump in the martensitic transformation rate while cooling signifies the initiation of the transformation from austenite to martensite (referred to as the martensite start temperature, M_s). Conversely, the subsequent drop in the transformation rate marks the conclusion of the martensitic transformation (designated as the martensite finish temperature, M_f). Likewise, the sudden changes in the transformation rate during the heating process serve as indicators of the transformation from martensite to austenite (referred to as austenite start temperature, A_s , and austenite finish temperature, A_f). For demonstration of phase transformations and differentiation between various crystal structures at key moments of the simulation, the atomic models were visualized using OVITO [120], where the polyhedral template matching (PTM) algorithm [121] was employed to assign color coding to the models. In the inset figures of Figure 3.6, the B19' structure (martensite) was represented by red atoms, while the B2 phase (austenite) was depicted by blue atoms.

As illustrated in the inset (a) in Figure 3.6, during the cooling process from 900 °C, no transformation occurs and the alloy maintains the B2 crystal structure (the only change in the model is the decrease in the atomic volume). This pattern persists until the temperature reaches

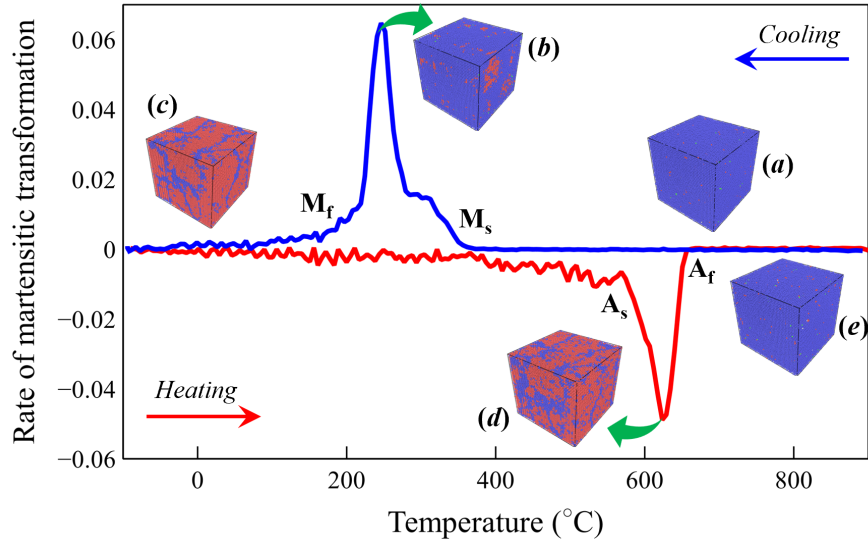


Figure 3.6 The change of the rate of martensitic transformation with respect to the temperature, denoting transformation temperatures. Sudden jumps in atomic volume during heating and cooling indicate the phase transformation. In insets, B2 structure is shown in blue and B19' is shown in red

M_s (350 °C), where the nucleation of the martensite phase occurs in the model, resulting in a sudden increase in the rate of transformation. The martensite volume fraction (represented by red color in inset (b)) continues to grow until reaching M_f (220 °C), at which point the model becomes completely martensitic for temperatures below M_f (inset (c)). During the heating step, although the majority of atoms remain in the martensitic state, some regions of austenite begin to nucleate within the model. Once the temperature reaches 550 °C (A_s), the reverse transformation (Martensite \rightarrow Austenite) starts, leading to a sudden change in the transformation rate. Between A_s and A_f , which occurs at 650 °C, a mixture of austenite and martensite can be observed (inset (d)). However, after reaching A_f , the model becomes entirely austenitic (inset (e)).

The study also included an investigation into the sensitivity of the results with respect to the size of the model. To assess this, various models were examined, each containing a different number of atoms ranging from 2000 to 1,000,000. Each model size was subjected to four separate simulations to obtain a robust set of data. The key focus was on analyzing the average values of M_s and A_f for each model size, which was then presented in Figure 3.7. In the graph, an oscillatory behavior in the values of M_s and A_f is apparent for the smaller models. This oscillation suggests

that the measured M_s and A_f values experience fluctuations and variations in smaller systems, potentially due to the limited number of atoms and statistical noise inherent in such cases. This observation is further supported by the larger error bars associated with the measurements for the smaller models, which reflect the increased uncertainty in determining the precise values of M_s and A_f . However, as the model size increases, the oscillatory pattern diminishes, and convergence of M_s and A_f values becomes evident. This convergence phenomenon indicates that with a larger number of atoms in the model, the measured M_s tends to stabilize around 330 °C, while the measured A_f converges at approximately 635 °C. As the model size expands, the system becomes more representative and yields more reliable and consistent values for the critical temperatures, M_s and A_f . These results highlight the importance of considering the size of the model when analyzing phase transformations and TTs range. It suggests that larger models provide a more accurate representation of the system's behavior, offering enhanced confidence in the reported M_s and A_f values. By capturing a greater number of atoms and encompassing a broader scope of interactions, larger models can help mitigate statistical fluctuations and obtain more robust and reliable results.

To investigate the stress-induced phase transformation in $\text{Ni}_{50.3}\text{Ti}_{29.7}\text{Hf}_{20}$, the ternary Ni-TiHf MEAM potential was employed. The modeling approach followed a similar methodology as the temperature-induced phase transformation simulations. However, in this case, a monotonically increasing compressive stress was applied at a constant temperature (T). Based on the results obtained from the temperature-induced phase transformation analysis depicted in Figure 3.6, three simulations were conducted to capture the behavior of NiTiHf under different conditions. Specifically, these simulations aimed to observe the superelastic behavior ($T > A_f$), the martensitic behavior ($T < M_f$), and the mixed phase behavior ($T > M_s$) of the material. The simulations were performed at temperatures of 700 °C, 200 °C, and 350 °C, respectively.

For the simulations at 700 °C and 200 °C, an equilibration step was carried out using the isobaric-isothermal NPT ensemble without applying any pressure before applying the stress. This step ensured that the system reached a stable equilibrium state prior to applying stress. However, since the material at 350 °C can exist in both the austenitic and martensitic phases, an additional

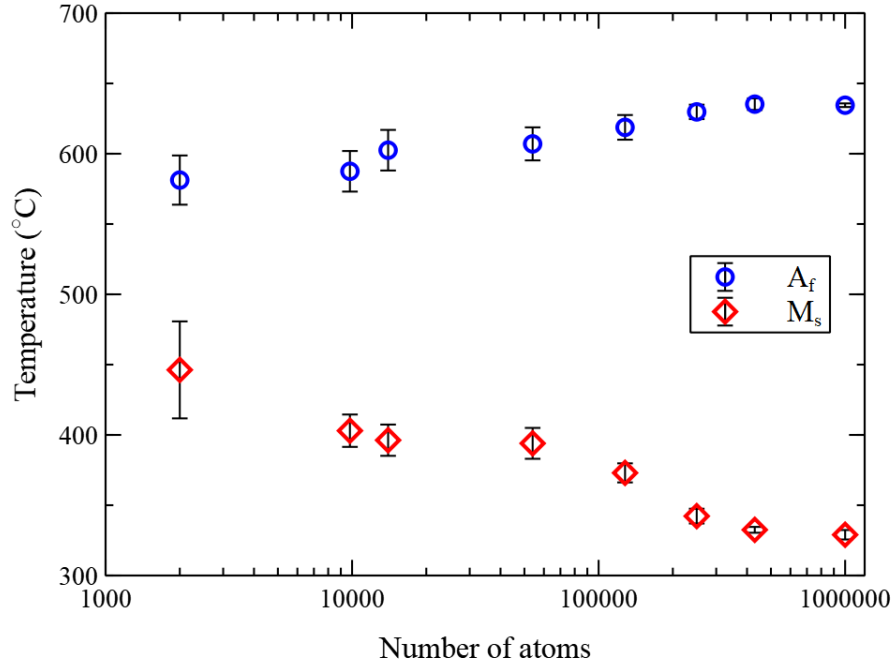


Figure 3.7 $\text{Ni}_{50.3}\text{Ti}_{29.7}\text{Hf}_{20}$ model size effect on the values of M_s and A_f obtained from MD simulations

step involving cooling and heating was necessary to properly capture its behavior. Further details regarding this step will be provided and explained in more depth later in the study.

Models were subjected to a stress-controlled uniaxial compressive load along the [100] crystallographic orientation. The compressive stress was incrementally increased from 0 to 2 GPa and subsequently reduced back to 0 GPa, using a stress rate of 5 MPa/ps. The stress-strain response of the models at various temperatures was investigated and is depicted in Figures 3.8 and 3.9. Additionally, the figures show the presence of different phases within the models at significant moments during the simulations, presenting the phase evolution during the stress-induced phase transformation process.

In Figure 3.8a, the stress-strain behavior of the model at 200 °C is presented. The inset (I) within the figure provides a snapshot of the model's initial state before any load is applied, indicating that the model was fully martensitic at that stage. Upon loading the model, the stress-strain curve exhibits a stress plateau at approximately 1 GPa, corresponding to a strain of 0.017. During this phase, the twinned martensite begins to transform into detwinned martensite, although

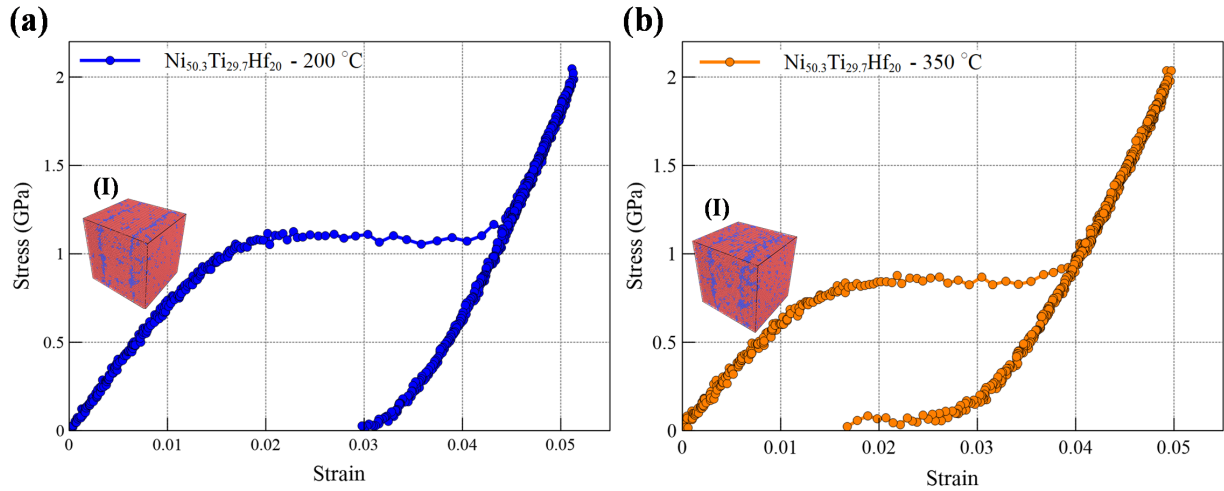


Figure 3.8 Stress-strain graphs of $\text{Ni}_{50.3}\text{Ti}_{29.7}\text{Hf}_{20}$ subjected to compression in [100] direction at (a) 200 °C ($T < M_f$), and (b) 350 °C ($T > M_s$), computed by the developed ternary MEAM potential. In insets, B2 structure is shown in blue and B19' is shown in red

the PTM algorithm utilized in the study cannot distinguish between the two types. Continuing the loading process leads to a total strain of 0.051 in the model. As the unloading stage begins, the elastic deformation of the detwinned martensite becomes apparent. The residual strain of 0.03 remains in the model at the end of the unloading step.

To obtain a proper mixed-phase structure, a specific thermal treatment was conducted before applying the compressive load. The model was initially equilibrated at 900 °C and subsequently cooled to -100 °C. Finally, the temperature was raised to 350 °C. In Figure 3.8b(I), which represents the initial state of the model, it can be observed that the predominant phase is still martensitic. However, compared to Figure 3.8a(I) (which corresponds to loading at 200 °C), there is an increase in the fraction of austenite and a decrease in the fraction of martensite. Analyzing the stress-strain graph in Figure 3.8b, it is evident that the stress plateau occurs at 715 MPa, corresponding to a strain of 0.013. Upon loading, the total strain reaches 0.05. Upon unloading, a residual strain of 0.017 can be observed, which is lower than the residual strain observed in the fully martensitic case (loaded at 200 °C). This behavior can be attributed to the presence of both austenite and a reduced fraction of martensite at 350 °C, as compared to the temperature of 200 °C during loading. Hence, in this study, this behavior is referred to as mixed-phase behavior.

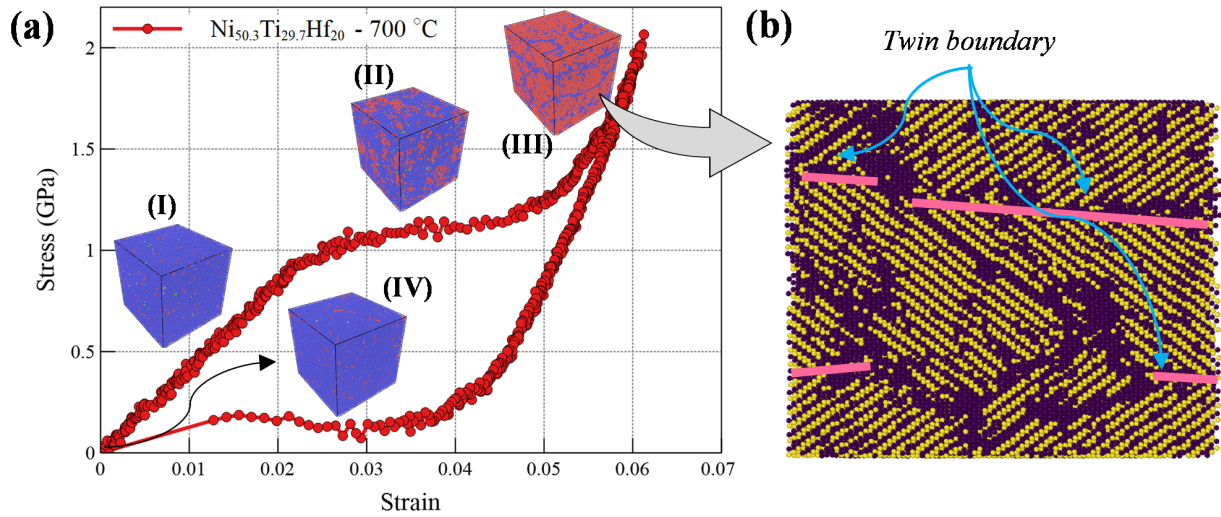


Figure 3.9 Stress-strain graph of $\text{Ni}_{50.3}\text{Ti}_{29.7}\text{Hf}_{20}$ subjected to compression in [100] direction at 700 °C ($T > A_f$), computed by the developed ternary MEAM potential. In insets, B2 structure is shown in blue and B19' is shown in red

At temperature of 700 °C, which is above the austenite finish temperature ($A_f = 650$ °C), a complete superelastic behavior was observed in the model, as depicted in Figure 3.9a. Upon loading, the forward phase transformation initiates at a stress of 960 MPa. By the end of the loading process, the majority of the model undergoes a transformation into martensite (as shown in Figure 3.9a(III)), resulting in a total strain of 0.061. During unloading, a reverse phase transformation from martensite to austenite takes place entirely, as illustrated in Figure 3.9a(IV). This reverse transformation enables perfect strain recovery, indicating the superelastic behavior of the material at 700 °C. Figure 3.9b provides a view of the transformed martensite at the end of loading at 700 °C, in (110) plane. Pink lines have been added to indicate the locations of twin boundaries, aiding in the visualization of these features. It is noteworthy that similar superelastic and martensitic behaviors, as well as twinning patterns, have been observed in experimental studies conducted on the same NiTiHf composition [68]. This consistency between the simulation results obtained using the developed ternary MEAM potential and experimental findings confirms the reliability and accuracy of the employed potential model.

CHAPTER 4

PRECIPITATE PHASE IN NiTiHf (H-PHASE)

4.1 Challenges in Employing HTSMAs

When employed in practical applications, HTSMAs face several significant challenges that need to be addressed. Among these challenges, the most crucial ones are the occurrence of large plastic deformations at high temperatures and stress levels, unstable cyclic performance, and a behavior that strongly depends on orientation and texture [29, 122]. Additionally, in the high-temperature regime, there are several other factors, such as creep and oxidation, which can uniquely influence the shape memory behavior [35, 123]. In essence, HTSMAs suffer from a major problem: they have low strength for generating and allowing the motion of dislocations, resulting in the accumulation of significant irrecoverable strain and cyclic instability [25, 36].

4.2 Precipitation in NiTiHf

To overcome these challenges and improve the shape memory and mechanical properties of HTSMAs, various methods have been employed. These methods include thermomechanical processing, precipitate hardening, solid solution hardening, and grain refinement of polycrystalline alloys [10, 35, 36, 64, 124–126]. However, a significant obstacle arises when dealing with prospective HTSMAs systems, as they are often ordered intermetallics that exhibit limited ductility at low and intermediate temperatures. This limitation makes it difficult and expensive to apply thermomechanical processing techniques to increase the material's strength. Therefore, to enhance the strength of HTSMAs, precipitation hardening methods are considered the most practical and cost-effective approach among others. By introducing nanoscale particles into the material, the strength of the matrix can be increased by elevating the critical shear stress required for slip. This improvement in strength subsequently enhances the shape memory properties and fatigue life of

the material [127–130]. Moreover, the inclusion of nanoscale particles as barriers to dislocation motion contributes to the improvement of fatigue life and cyclic stability [127, 129].

It is important to note that the effectiveness of the strengthening achieved by precipitates depends on various factors such as their size, volume fraction, interparticle spacing, and coherency with the second phase [131]. Additionally, factors like aging time, temperature, and lattice mismatch between the matrix and precipitates introduce local stress fields that alter the strengthening behavior, martensite nucleation, and shape memory and material properties. By employing alloying techniques and thermal treatments, it is possible to manipulate the precipitation characteristics of NiTiHf alloys. This control over precipitation opens up opportunities for designing NiTiHf alloys with desirable properties such as high TTs, superior strength, and stable response.

As per previous studies, the presence of different types of precipitates has been confirmed in NiTiHf alloys depending on various factors such as the alloys being Ti-rich or Ni-rich. Konig et al. [132] studied a wide range of NiTiHf compositions by fabricating thin films of NiTiHf using the magnetron sputtering method. They investigated the precipitate structure and thermal cycling properties of the specimens. Through annealing the multilayer thin films at 550 °C for 1 hour, the initial multilayer structures were transformed into alloys. The study depicted the composition regions in which different precipitates were formed based on the relative intensity of a characteristic X-ray diffraction (XRD) peak. In Ti- and Hf-rich composition regions, four distinct precipitates were seen, i.e. HfNi(Ti), Ti₂Ni(Hf), Hf₂Ni(Ti), and the Laves phase. Their findings indicated that as the Ti content increased in the NiTiHf alloy, there was a corresponding increase in the presence of the secondary Laves phase. This led to a rise in thermal hysteresis. In cases where the Laves phase precipitates were present in small amounts, it was observed that the stress recovery of the NiTiHf thin films increased. The study concluded that the strengthening of the matrix due to the Laves phase precipitates resulted in improved functional fatigue properties, particularly for alloy compositions rich in Ti and Hf.

Other works also have observed the presence of Ti₂Ni(Hf) precipitates in Ni-lean NiTiHf alloys [133–136]. It has been noted that the volume fraction of Ti₂Ni(Hf) precipitates decreases

as the Ni content increases, although they can still be found in slightly Ni-rich compositions [133, 137]. These fine $\text{Ti}_2\text{Ni}(\text{Hf})$ precipitates play a crucial role in strengthening the matrix and enhancing the shape memory and superelastic properties of NiTiHf-based alloys [134]. Importantly, the size of the $\text{Ti}_2\text{Ni}(\text{Hf})$ precipitates has a significant influence on controlling the martensite morphology. Studies have found that when the material contains evenly distributed $\text{Ti}_2\text{Ni}(\text{Hf})$ precipitates with diameters ranging from 20 to 40 nm, the dominant martensite morphology consists of (001)B19' compound twins. A similar martensite morphology has been observed in Ti-rich NiTi thin films with homogeneously distributed fine Ti_2Ni precipitates [138]. Additionally, martensite domains with (001)B19' compound twins have been observed around larger $\text{Ti}_2\text{Ni}(\text{Hf})$ precipitates.

To study the precipitate phase in Ni-rich NiTiHf, Han et al. [139] performed an aging heat treatment at 600°C for 150 hours on a $\text{Ni}_{48.5}\text{Ti}_{36.5}\text{Hf}_{15}$ alloy. Through comprehensive TEM analysis, they discovered the existence of a precipitate type with a composition of $\text{Ti}_{0.6}\text{Hf}_{0.4}\text{Ni}$ in the alloy. The precipitate had a face-centered orthorhombic lattice and it exhibited a close association with the B2-type matrix. In addition, the precipitate possessed an oblate spindle-like shape. They called it "H-phase precipitate". The distribution of the formed precipitates in NiTiHf alloy is shown in Figure 4.1.

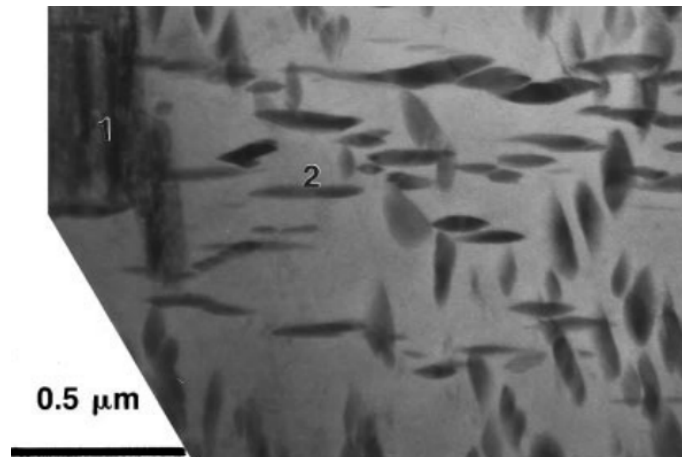


Figure 4.1 Distribution of the precipitates in B2 alloy matrix [139]

Meng et al. [137] conducted a study to characterize the precipitate type in Ni-rich compositions of NiTiHf. They observed that upon aging Ni_{50.6}Ti_{29.4}Hf₂₀ alloy at 550°C, (Ti + Hf)₃Ni₄ precipitates form. As the aging time increased, the precipitates grew to larger sizes. When the precipitates were small, the precipitation did not have a significant impact on the morphology of martensite. However, in the Ni_{50.6}Ti_{29.4}Hf₂₀ alloy aged at 550°C for 5 hours, leading to precipitates of approximately 50 nm in size, the martensite variants exhibited strong preferential orientation. The formation of (Ti + Hf)₃Ni₄ precipitates strengthened the matrix of the Ni-rich NiTiHf alloy, resulting in improved thermal stability of the transformation temperatures.

Since the composition of the H-phase was not analyzed by Han et al. [139], the details of images extracted using high-resolution scanning transmission electron microscopy (STEM) could not be explained properly. Therefore, Yang et al. [69] employed high-angle annular dark field (HAADF)-STEM, atom probe tomography (APT) and first-principles calculations to fully characterize the H-phase. They made an alloy with composition of Ni_{50.3}Ti_{29.7}Hf₂₀ using induction melting and aged it at 600°C for 815 h. Extending the aging time had the effect of increasing the coarseness of the precipitates, which facilitated the characterization of the precipitate phase. The HAADF-STEM image of the aged alloy is presented in Figure 4.2 while the precipitates have been highlighted using enhanced Z contrast. The spindle-shaped precipitates were measured, revealing approximate dimensions of 40-50 nm in thickness and 300-500 nm in length.

The area electron diffraction patterns were obtained from the identified precipitates, and the findings agreed with those previously reported by Han et al. [139]. In Figure 4.3 several significant electron diffraction patterns, along with their angular relationships, on the [001]_{B2} stereographic projection of the parent B2 phase, are presented. The obtained results suggest a strong structural connection between the precipitates and the parent B2 grains in which they formed, as the aging process was conducted above the A_f temperature. The orthorhombic unit cell obtained for the H-phase precipitate is illustrated in Figure 4.4. The lattice parameters were similar to those reported by Han et al. [139]: $a = 4a_0$, $b = 2\sqrt{2}a_0$, $c = 6\sqrt{2}a_0$, where a_0 is the lattice parameter of B2

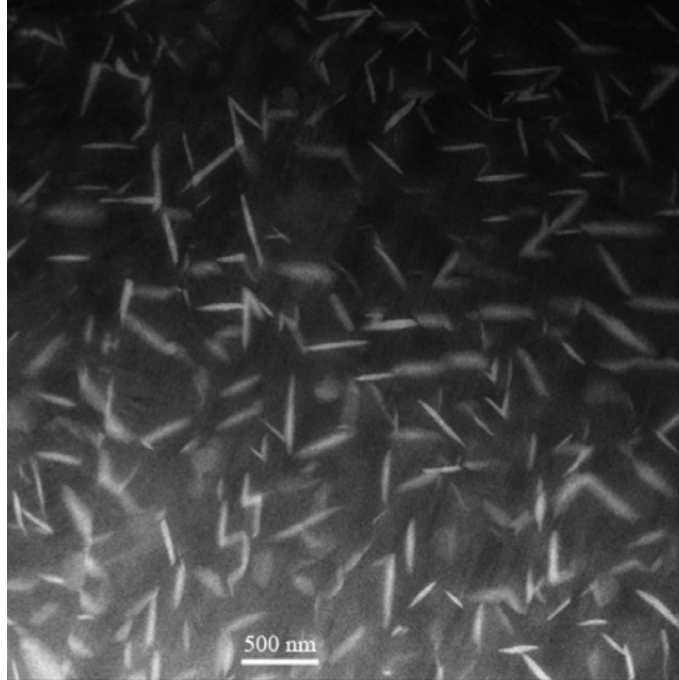


Figure 4.2 Spindle-shaped precipitates in aged $\text{Ni}_{50.3}\text{Ti}_{29.7}\text{Hf}_{20}$ [69]

parent structure. The lattice correspondence was reported to be as:

$$[100]_{\text{H}} \longrightarrow [001]_{\text{B2}} \quad (4.1)$$

$$[010]_{\text{H}} \longrightarrow [110]_{\text{B2}} \quad (4.2)$$

$$[001]_{\text{H}} \longrightarrow [-110]_{\text{B2}} \quad (4.3)$$

Upon examination, it became evident that the suggested unit cell possesses the $F2/d2/d2/d$ space group. The composition of the H-phase was found to be Ni_3TiHf_2 . However, both existing literature [67, 140, 141] and the findings of Yang et al. [69] indicated that the composition of H-phase precipitates varies depending on the composition of the initial alloy even with similar heat treatment process. Therefore, they might not possess a unique composition, unlike Ni_4Ti_3 precipitates which form in a fixed composition regardless of NiTi's initial composition.

On this matter, Santamarta et al. [141] found that the composition of the precipitates in Ni-rich NiTiHf contains a higher content of the third element (Hf), a lower proportion of Ti and slightly more Ni compared to the initial composition of the Ni-rich alloy. They also discovered

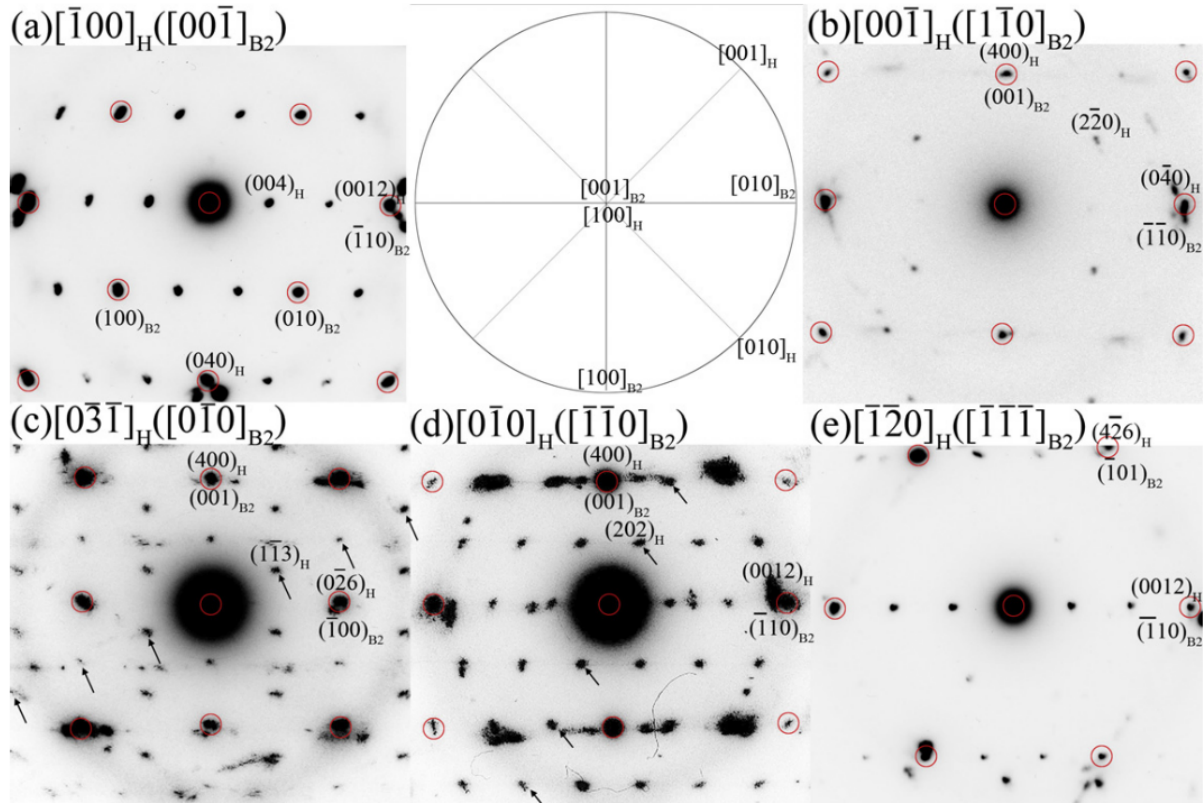


Figure 4.3 Electron diffraction patterns of the precipitates and their angular relationships with B2 parent phase [69]

that the growth rate of precipitates is sensitive to the contents of Ni and Hf since by increasing Ni content, the precipitates grew faster as was the case for increasing Hf and keeping Ni content constant. In this study, to understand the effect of precipitates on the thermo-mechanical behavior of NiTiHf, MD simulations have been performed using the developed MEAM potential on NiTiHf models with and without precipitates.

4.3 Methodology

For MD simulations and visualization purposes, LAMMPS code [118] and Ovito software [120] were used, respectively. The matrix and precipitate models were created using AtomsK [119]. The same Ni-rich composition $\text{Ni}_{50.3}\text{Ti}_{29.7}\text{Hf}_{20}$ that was studied in Chapter 3, was considered for MD models. The crystal structure reported by Yang et al. [69] for Ni-rich NiTiHf was chosen for the H-phase precipitate i.e. Ni_3TiHf_2 . It was reported in the literature that lower aging temperatures

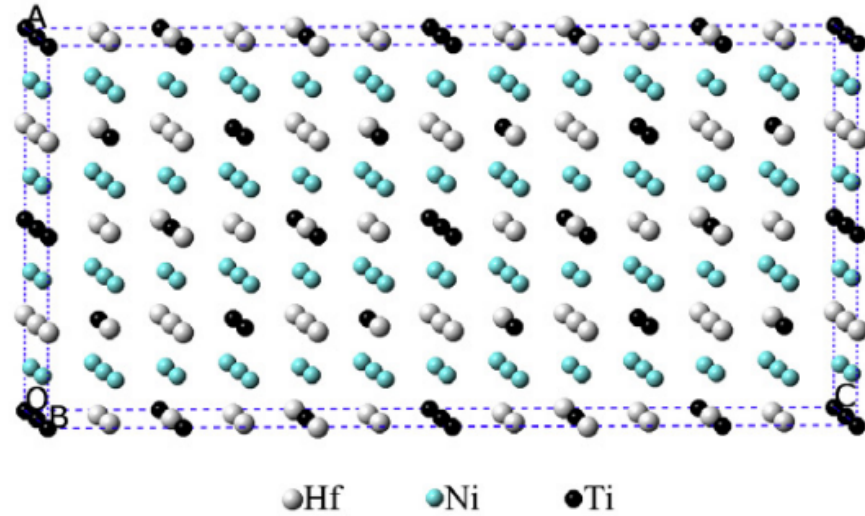


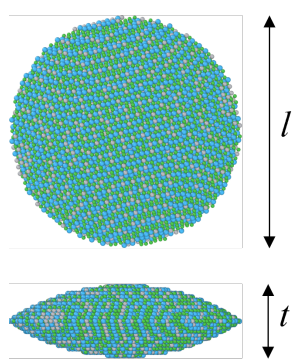
Figure 4.4 Unit cell of the orthorhombic precipitate [69]

lead to fine and coherent H-phase precipitates. On the other hand, in higher aging temperatures, precipitates grow and interparticle distance increases. Therefore, to capture the effect of each of these cases, two scenarios were considered for models with precipitate. In one scenario, the NiTiHf model contained a single large precipitate in the center of a matrix, resembling the alloy aged at higher temperatures. Furthermore, in the second scenario, the model with the same size contained eight smaller precipitates distributed evenly in the box. The ratio of the precipitate to the matrix was similar in both cases.

To model the NiTiHf matrix with a single precipitate (this model will be called the "single-precipitate" model), initially an oblate spindle-like shape was created with an orthorhombic crystal structure. Then a NiTiHf box was generated with the dimensions of $250 \times 250 \times 250 \text{ \AA}$. Finally, the precipitate model was embedded into the middle of the NiTiHf matrix. The lattice correspondence of precipitate (subscript H) to matrix (subscript $B2$) was based on equation 4.1 to 4.3 i.e. $[100]_H \rightarrow [001]_{B2}$; $[010]_H \rightarrow [110]_{B2}$; $[001]_H \rightarrow [\bar{1}10]_{B2}$. Moreover, the minor axis of the precipitate was along $[001]$ crystal orientation. For the model with multiple precipitates (this model will be called the "multi-precipitate" model), the same method was conducted on a smaller NiTiHf box ($125 \times 125 \times 125 \text{ \AA}$) where a smaller precipitate was embedded in the center of the matrix. Then, this model was replicated 2 times in three dimensions, to create a model containing eight

precipitates. The details of the shape, size and crystal structure of the precipitates are presented in Table 4.1. In addition, Figure 4.5 shows the final single-precipitate NiTiHf model while Figure 4.6 shows the distribution of fine precipitates in the multi-precipitate model (matrix atoms are not shown). The model in Figure 4.5 has been cut in half for better visualization. The models contained almost 1,000,000 atoms where the ratio of precipitation was 2.6% in both cases.

Table 4.1 Precipitate's shape, size and crystal structure

Parameter	Ni-Ti-Hf	Model
Shape	Oblate spindle	
t (Single-precipitate)	50 Å	
l (Single-precipitate)	150 Å	
t (Multi-precipitate)	22 Å	
l (Multi-precipitate)	70 Å	
Crystal structure	Ni ₃ TiHf ₂	
a ($4a_0$)	12.66 Å	
b ($2\sqrt{2}a_0$)	8.83 Å	
c ($6\sqrt{2}a_0$)	26.14 Å	
α	90 °	
β	90 °	
γ	90 °	

During simulation, the timestep was taken as 2 fs. Periodic boundary conditions were considered in all directions to reduce surface effects. To control the temperature, the Nose-Hoover style thermostating was employed while for pressure, the Nose-Hoover barostating method was implemented on all atoms. In order to study the effect of precipitate on the temperature-induced phase transformation of NiTiHf, similar to Section 3.7, a cooling and heating cycle was applied to the models with and without precipitate. Initially, the models were equilibrated at 800 °C and

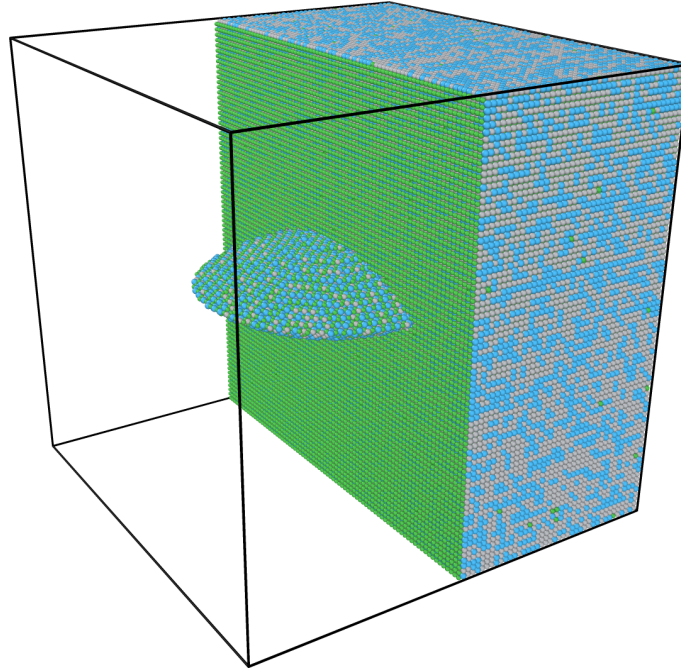


Figure 4.5 Embedded precipitate in single-precipitate NiTiHf matrix

then, were cooled to 0 °C followed by a heating to 800 °C at a controlled rate of ± 2.75 °C/ps. The rate of the martensitic transformation which was calculated by measuring the fraction of martensite in the model at each step of the thermal cycle, was obtained for all the models. The variation of the rate of transformation is presented in Figure 4.7 with respect to the temperature change. In these graphs, the abrupt jump in the rate of martensitic transformation while cooling signifies the initiation of the transformation from austenite to martensite (M_s). The subsequent drop in the rate of martensitic transformation indicates the completion of the transformation (hence representing M_f). Similarly, the sudden jump and drop in the transformation rate while heating serve as indications of the transformation from martensite to austenite (A_s and A_f). As can be seen in Figure 4.7, the austenite start and finish temperatures increased in the models containing precipitate. This increase in the single-precipitate model is the highest, while the multi-precipitate model experienced a lower increase in A_s and A_f values.

To explore this difference, a cross-sectional view of each model, displaying the austenite and martensite phases existing at the end of the cooling process, is depicted in Figure 4.8. The application of color coding, employing the Polyhedral Template Matching (PTM) algorithm,

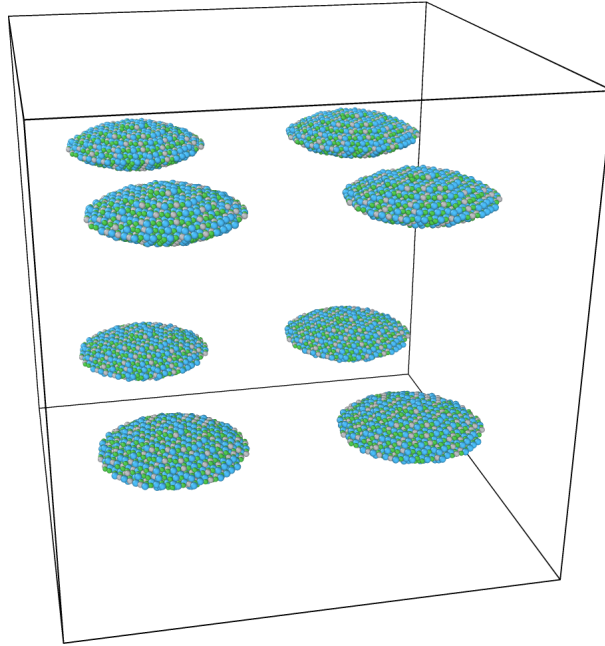


Figure 4.6 Distribution of fine precipitates in multi-precipitate NiTiHf matrix

facilitated the differentiation of distinct phases in each model. In Figure 4.8, the martensite phase (with a B19' structure) is indicated in red, while the austenite phase (with a B2 structure) is depicted in blue. The visual representation illustrates that a substantial portion of the initially austenitic material in all models has transformed into martensite. The blue bands of atoms indicate the twinning planes. It can be observed that the precipitate-free model contains a dense distribution of twinning planes. It is important to highlight that these twinning planes serve as sites for the nucleation of austenite during the reverse phase transformation from martensite to austenite. Consequently, in the precipitate-free model, this reverse transformation happens at a lower temperature (earlier), leading to lower austenite start and austenite finish temperatures. Conversely, in the single-precipitate model, characterized by a single and relatively wide twinning plane, the reverse phase transformation occurs at a higher temperature due to the presence of fewer potential nucleation zones. Consequently, this scenario results in higher A_s and A_f temperatures. In the case of the multi-precipitate model, there is a greater quantity of twinning planes when compared to the single-precipitate model, but this quantity is still less than what is observed in

the precipitate-free model. Therefore, this leads to notably reduced TTs in comparison with the single-precipitate model and only slightly higher TTs than those seen in the precipitate-free model.

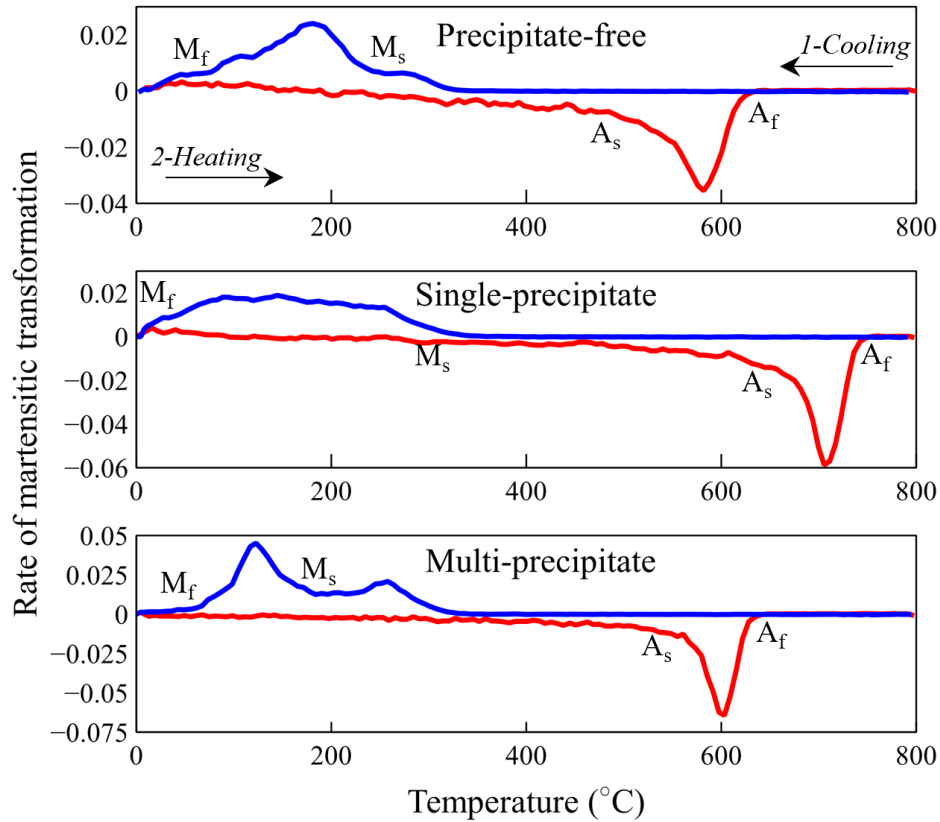


Figure 4.7 Variation of the rate of martensitic transformation with respect to the temperature, denoting transformation temperatures. Sudden changes in the rate of transformation during heating and cooling indicate the phase transformation

The effect of precipitates on superelastic and martensitic responses of NiTiHf alloy with $\text{Ni}_{50.3}\text{Ti}_{29.7}\text{Hf}_{20}$ composition was also studied. Two simulation temperatures: one below M_f and one above A_f were considered to study martensitic and superelastic behaviors of the precipitated and precipitate-free models. By considering Figure 4.7, 0 °C was chosen as the martensitic temperature. The temperature selected for observing superelastic behavior above A_f , was determined to enable a meaningful comparison of the resultant stress-strain responses. This choice was made based on the Clausius-Clapeyron equation, which establishes a linear relation

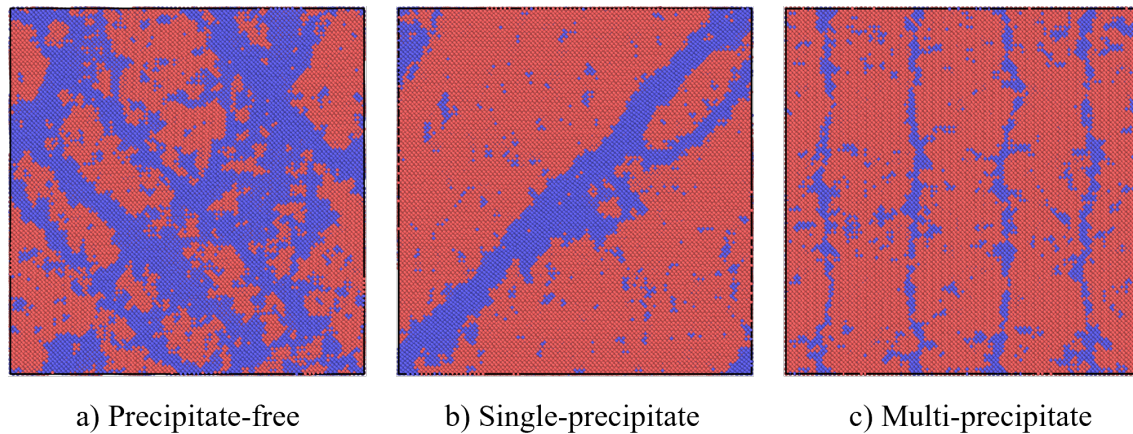


Figure 4.8 Present phases at the end of the cooling stage. Red atoms show martensite and blue atoms show austenite phase

between transformation stress and temperature. Hence, the stress-induced phase transformation was studied at a temperature of $A_f + 50$ °C for each model. The isobaric-isothermal NPT ensemble was used for the equilibration and loading of the models. For martensitic temperature, after equilibration of the model at 0 °C, a uniaxial compressive load was applied along [100] direction. The load gradually increased from 0 to 2 GPa, and then the model was unloaded back to 0 GPa. Figure 4.9 shows the stress-strain behavior of models with and without precipitate at 0 °C. The maximum strain in single-precipitate and multi-precipitate models is larger compared to the precipitate-free model. It has been reported that the H-phase precipitates are completely coherent with austenitic matrix [141]. When the model is cooled to a martensitic temperature, this coherency becomes disrupted as a result of transformation strains. Consequently, in the presence of H-phase precipitates, the martensitic matrix must adjust to accommodate the non-transforming particles, leading to higher strain levels. Figure 4.10 presents this loss of coherency around the precipitate(s) using Ovito's defect mesh analysis. This algorithm is designed to highlight areas within the model where the atomic arrangement deviates from the perfect crystal structure. Accordingly, insets (I) and (III) display the defect mesh around the surface of the precipitate, for both the single-precipitate and multi-precipitate models before undergoing equilibration. On the other hand, insets (II) and (IV) depict the defect mesh after equilibration at the martensitic temperature. It is evident

that the surface of the precipitates has become uneven and rough, signifying a loss of coherency between the precipitate and the matrix.

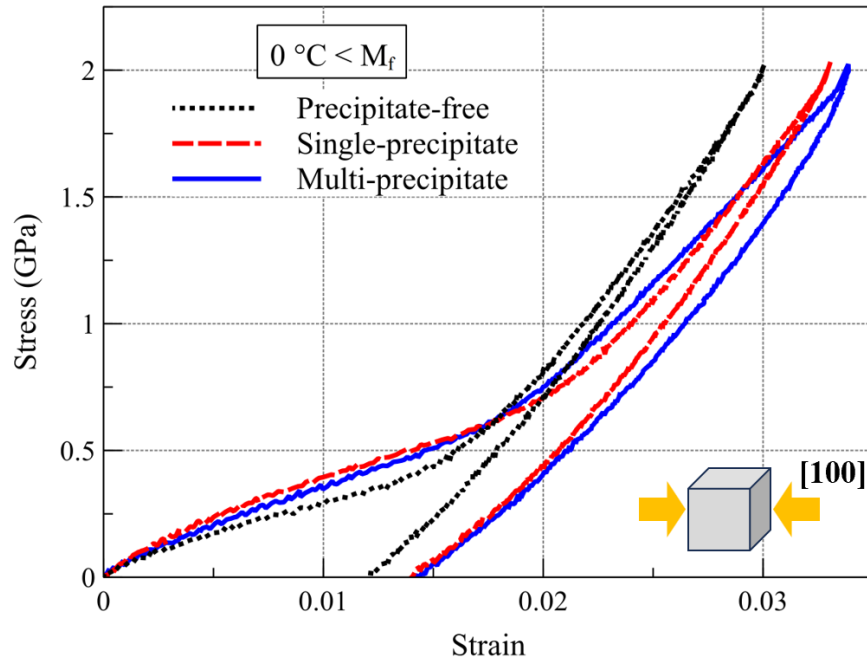


Figure 4.9 Stress-strain behavior of models simulated at 0 °C

The superelastic stress-strain curves of the precipitate-free, single-precipitate, and multi-precipitate models are presented in Figure 4.11, which were subjected to equilibration and loading at 675, 780 and 685 °C ($A_f + 50\text{ }^{\circ}\text{C}$), respectively. During loading, the austenitic phase experiences elastic deformation and subsequently after reaching a certain deformation, the stress-induced transformation from austenite to martensite occurs. Stress-induced phase transformation was initiated at approximately 0.025 strain across all the models. As the loading process advanced, the models experienced some transformation strains, which manifested as a plateau phase evident in the stress-strain curves. The multi-precipitate model showed a notably improved superelastic response. Nonetheless, this enhancement came alongside a moderate decrease in the capacity for energy dissipation, as indicated by a reduction in the size of the hysteresis loop, within the multi-precipitate model.

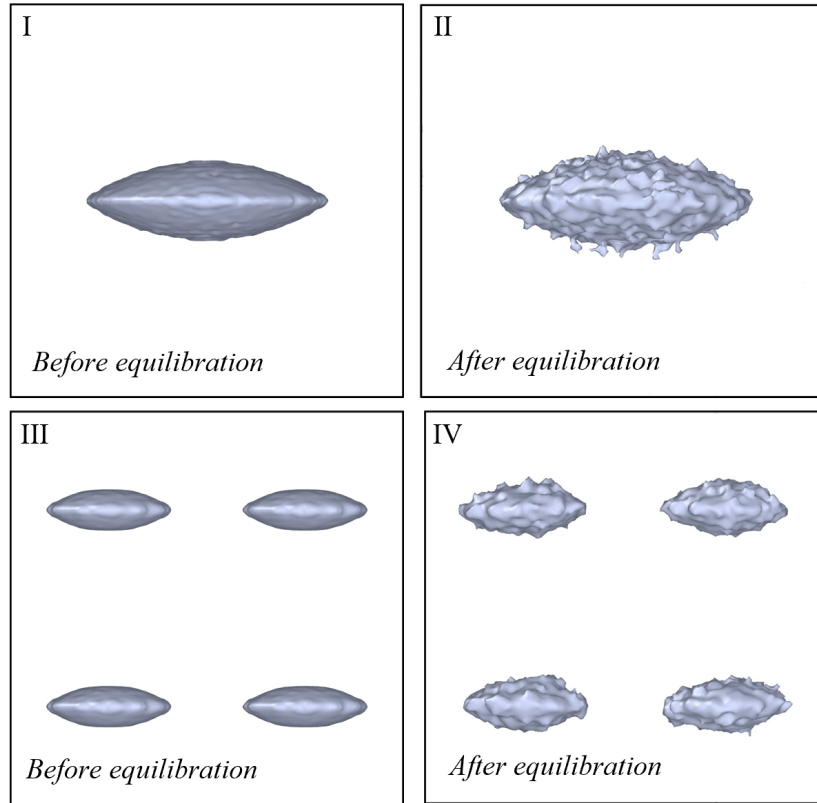


Figure 4.10 Presentation of the coherency of precipitates before and after equilibration at 0 °C

Furthermore, in terms of transformation behavior, the multi-precipitate model exhibited lower transformation strain and maximum strain values in comparison to the other models. This outcome stems from the greater complexity of selecting and propagating martensite variants in the presence of numerous precipitates. This phenomenon was further explored through the quantification of the martensite phase fraction during the simulation. It was observed that the multi-precipitate model attained a lower maximum martensite fraction when compared to the other two models, consequently leading to lower transformation strains.

It was reported that the shape memory and mechanical properties of Ni-rich NiTi alloys are significantly influenced by the crystallographic orientation of the material [142–146]. To study the direction-dependence of NiTiHf and the way H-phase precipitates affect the mechanical response of NiTiHf, both precipitate-free and precipitated models were subjected to compressive load along [110] crystallographic directions (in contrast to the previous case, which was loaded in the [100]

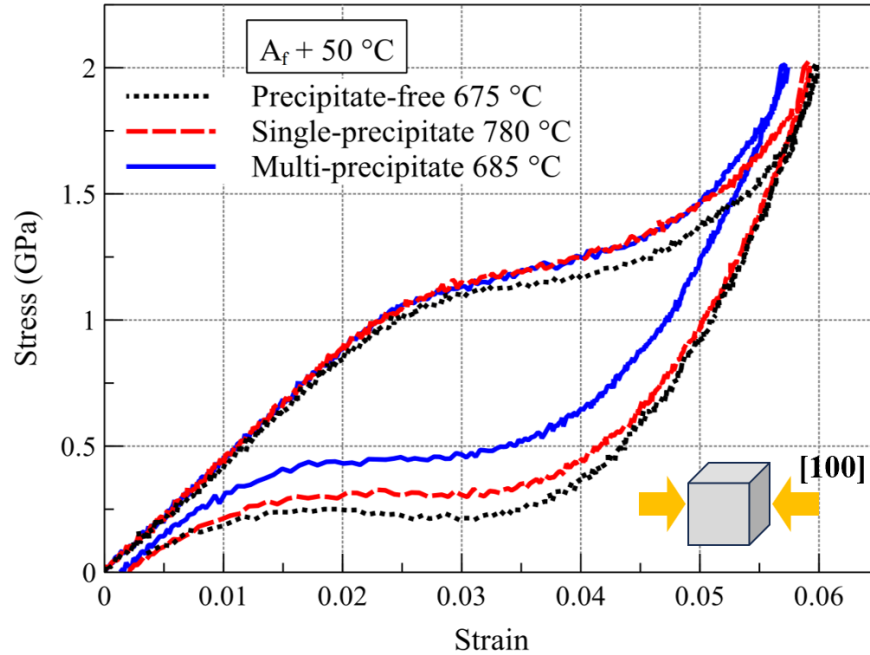


Figure 4.11 Stress-strain behavior of models simulated at $A_f + 50\text{ }^\circ\text{C}$

direction). Figure 4.12 presents the stress-strain behavior of models subjected to load in [110] direction at $0\text{ }^\circ\text{C}$ and $A_f + 50\text{ }^\circ\text{C}$. Unlike the equivalent cases loaded along [100] direction, when the models were subjected to compressive load along [110] direction at $0\text{ }^\circ\text{C}$, they all showed elastic behavior with no phase transformation (Figure 4.12(a)). It has been reported that in NiTi, grains oriented in the [110] direction effectively impede stress-induced phase transformation and detwinning [147, 148]. The consistent elastic behavior observed in all the models in Figure 4.12(a) can be attributed to the same underlying principle. This is because, at martensitic temperature and under the applied load, the models are unable to transform from twinned to detwinned martensite due to these inhibitory effects.

As can be seen in Figure 4.12(b), a noticeable difference was also observed at $A_f + 50\text{ }^\circ\text{C}$ compared to [100] direction. The maximum strain reached slightly over 0.03 while in [100] models, the amount of maximum strain was twice this value. Moreover, the energy dissipation observed in the [110] direction was notably less than that in the [100] direction. Once again, the crystallographic orientation had a hindering effect on the martensitic transformation process resulting in smaller transformation strains when compared to the [100] direction. Furthermore,

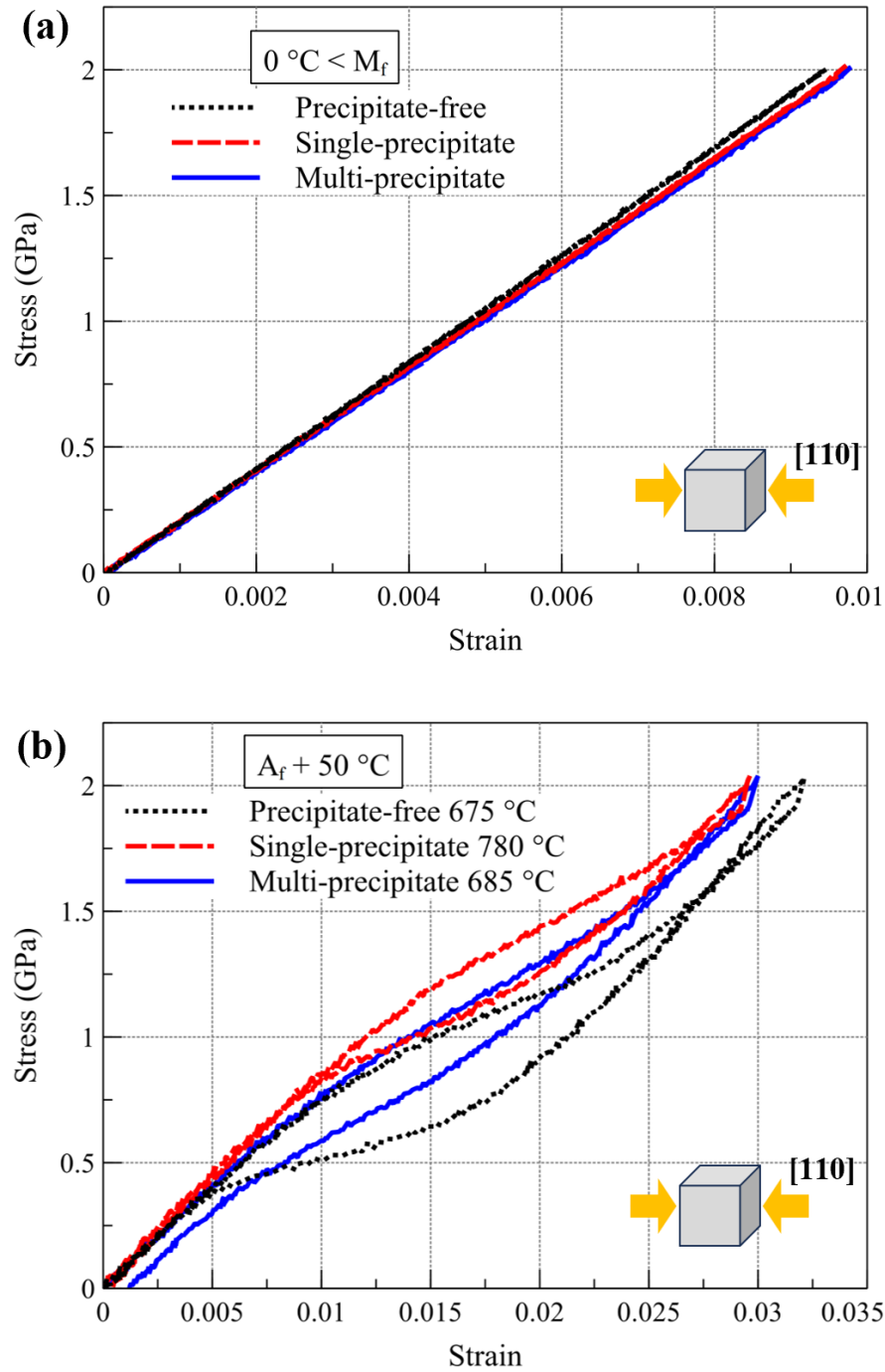


Figure 4.12 Stress-strain behavior of models in [110] direction at $0\text{ }^\circ\text{C}$ and $750\text{ }^\circ\text{C}$

both the single-precipitate and multi-precipitate models exhibited elevated stress plateaus when compared to the precipitate-free model, similar to the behavior observed in the [100] direction.

CHAPTER 5

THERMAL ACTUATION OR CYCLING IN NiTiHf

5.1 Introduction to the Thermal Actuation

As mentioned in Chapter 1, actuation in SMAs refers to the ability of these materials to undergo a reversible phase transformation and generate mechanical work in response to an external stimulus, typically a change in temperature or stress. Thermal actuation of an SMA involves subjecting the material to repeated cycles of temperature change, alternating between different levels. This process includes controlled heating and cooling of the material to activate the desired shape memory effect and superelasticity of the SMA. The ability of SMAs to exhibit this shape memory behavior upon temperature variation makes them valuable for various applications, such as actuators in devices that require precise and controllable movement. The thermal cycling of SMAs needs to be studied to investigate the SMA's response to varying temperatures, examining its thermal properties, mechanical behavior, phase transformations, and functional characteristics. Moreover, determining important factors in actuator applications such as transformation strains, thermal hysteresis, work output and dimensional stability can be obtained by studying thermal cycling.

Thermal cycling can also be employed to investigate the fatigue behavior of alloys, as repeated thermal expansion and contraction can induce mechanical stresses that may lead to material degradation over time [149]. Understanding the lifecycle of components is a significant challenge in the current implementation of SMAs in actuator applications. This involves comprehending the fatigue behavior of these actuators. While conventional engineering materials primarily experience fatigue due to cyclic load variations, materials undergoing phase transformations, such as SMAs, may encounter additional forms of fatigue. In the context of SMAs, an additional source of fatigue is present due to the physical motion of atoms corresponding

to the phase transformations [150]. Actuation fatigue typically is the term that refers to the degradation of dimensional integrity in SMA actuators due to the accumulation of plastic strains while performing thermal cycling. However, it is important to note that other shape memory characteristics, such as transformation temperatures, thermal hysteresis, and actuation strain, can also experience notable changes throughout the thermal cycling process. This evolution of material responses is commonly referred to as functional fatigue [151].

NiTiHf among other HTSMAs has shown promising performance when employed in actuation applications. In recent developments, torque tubes made of Ni-rich NiTiHf have been utilized to enable actuation in unmanned prototype folding wings aircraft, resulting in successful test flights [152]. These torque tubes have demonstrated the ability to rotate the winglets over a remarkable 160° rotation. Additionally, researchers have successfully employed torque tubes to actuate an F18 wing, achieving a span of 90° rotation [153]. Figure 5.1 [154] presents images of the prototype folding wing and the assembly of the torque tube setup used for actuating the F18 wing.

It is evident that there is a necessity to comprehend and optimize the microstructure of Ni-rich NiTiHf alloys in order to achieve the best possible actuation fatigue performance [155]. There have not been many research efforts on the thermal actuation of NiTiHf. This fact indicates the urgent need for performing relevant studies in this area. In similar previous research conducted on other SMAs, CuZnAl wire specimens subjected to repeated temperature-induced transformations demonstrated a relationship between the applied stress level and the fatigue life of SMA [156]. More recent investigations into actuation fatigue in SMAs, specifically NiTi and NiTiCu, were carried out by Lagoudas et al. [157, 158]. In their studies, NiTiCu wire specimens were subjected to various heat treatments and thermally cycled under constant nominal stresses until failure. The findings highlighted that the actuation fatigue performance of the SMAs is influenced by the specific heat treatment conditions, and the identification of optimal heat treatment is crucial for the effective utilization of these materials in fatigue-sensitive applications.

In this chapter, with the motivation of understanding the behavior of Ni-rich NiTiHf HTSMA under thermal cycling in the presence of constant stress, simulations were conducted



Figure 5.1 F18's folding wings and torque tube assembly for actuating the folding wings [154]

on MD models with $\text{Ni}_{50.3}\text{Ti}_{29.7}\text{Hf}_{20}$ composition and the effect of microstructure on thermal actuation of the alloy was studied.

5.2 Methodology

To perform thermal cycling simulation, thin plates were modeled with dimensions of $250 \times 250 \times 30 \text{ \AA}$ (Figure 5.2). MD simulation approach was similar to the method used in the previous chapters and the timestep was 2 fs. To obtain a proper range for constant compressive stress during thermal cycling, a compressive load of up to 1 GPa was applied along [100] crystallographic direction at 500 °C. This temperature is between M_f and A_f in which the model can exhibit shape memory response. The stress-strain response of the model is shown in Figure 5.3. The phase transformation plateau starts around 400 MPa above which the model experiences a large strain. Therefore, this value of stress was used for applying the constant stress during thermal cycling. For the thermal cycling, boundary conditions were periodic. After the equilibration step and before applying temperature change, a compressive load was applied incrementally along [100] direction from 0 to 400 MPa. Then the model was thermally cycled from 200 °C to 900 °C in the presence of constant stress. The values of temperature change were chosen to be below M_f (200 °C) and above A_f (900 °C).

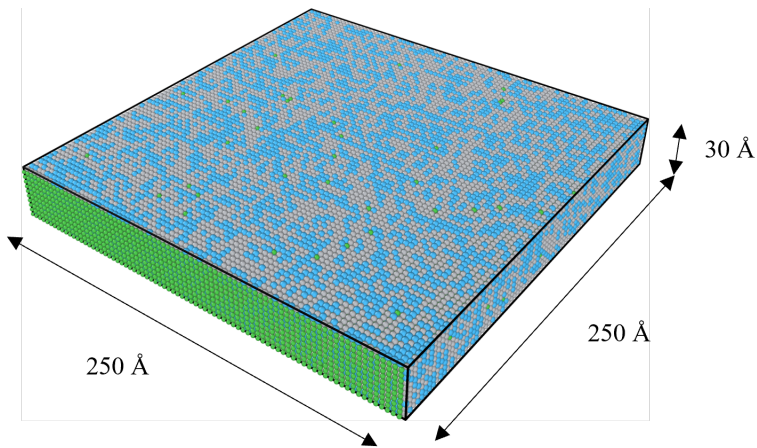


Figure 5.2 Detail of plate model in thermal cycling

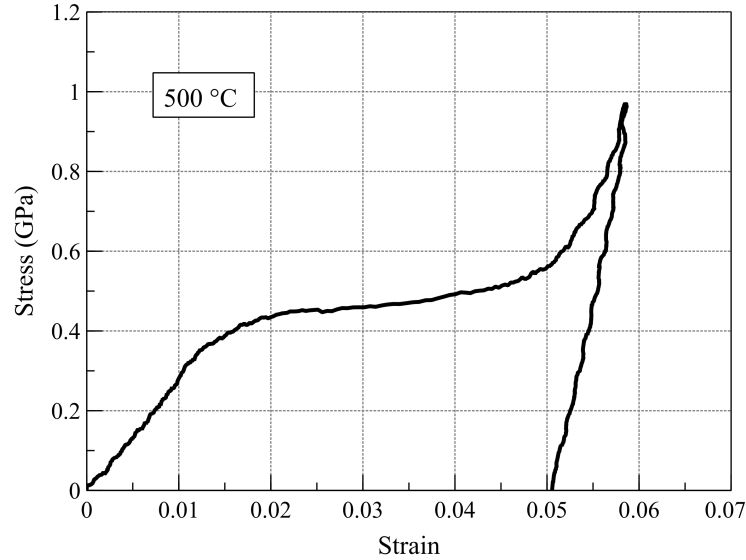


Figure 5.3 Stress-strain response of the plate model at 500 °C

5.3 Results

Due to computational cost in MD studies, it is not feasible to conduct temperature variation with a slow rate. Therefore, it is important to consider the temperature rate in MD simulations. To see the effect of temperature change rate on the response of the material, the temperature change was performed with four different rates i.e. 10, 5, 2 and 1 °C/ps. In Figure 5.4, the shape memory response (temperature-strain curves) of models with four different temperature rates under constant compressive load, is presented. It can be seen that by decreasing the temperature rate, the hysteresis becomes narrower. The temperature hysteresis with a temperature rate of 1 °C/ps drops 30% compared to the model with the rate of 10 °C/ps. However, the temperature rate did not affect the recoverable strain range significantly. The range of recoverable strain was 0.05 in all models. Considering the computational cost, for future simulations, the rate of temperature change was chosen as 5 °C/ps.

Furthermore, the effect of larger stress levels on the thermal cycling of the alloy was studied. First, to understand the monotonic thermo-mechanical response, a cycle of load-unloading-heating was applied to three different models. In each case, the model was loaded to a certain stress level above the plateau stress (i.e. 600, 800 and 1000 MPa) at 500 °C. Then

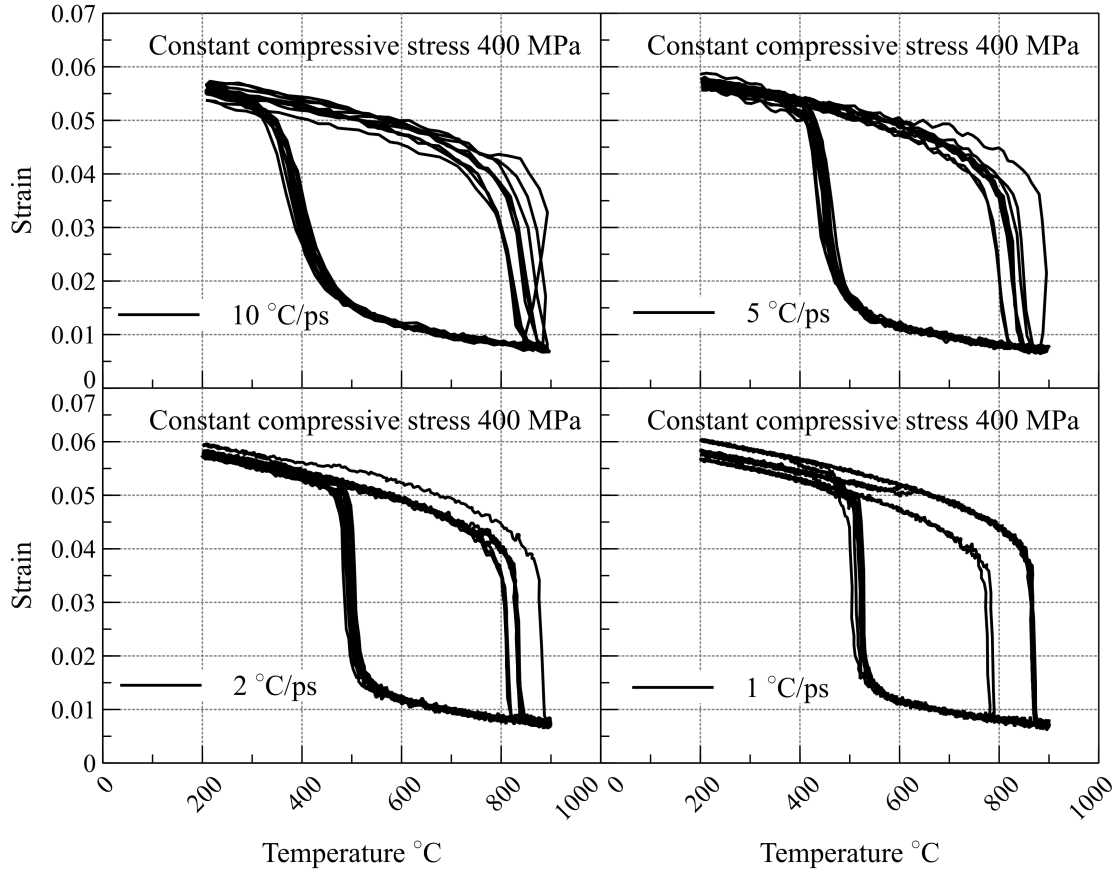


Figure 5.4 Shape memory response of the material obtained via thermal cycling with rates under constant stress of 400 MPa

it was unloaded and subjected to heating to a temperature above the A_f . Afterwards, in separate simulations, the thermal cycling was applied to the models under different constant stresses i.e. 600, 800 and 1000 MPa. The monotonic stress-strain-temperature curve and the thermal cycling response of each model are shown in Figures 5.5 to 5.7. As can be seen in Figure 5.5-5.7 (a), in the stress-strain part of the graph, the maximum stress is above the plateau stress. However, except for the first cycle of thermal cycling under 600 MPa, no shape memory response was observed in all models. Thermal hysteresis arises from the creation of structural imperfections (such as dislocations) and the dissipation of frictional energy caused by the resistance encountered when phase boundaries move. By increasing the constant stress, the dissipated energy decreases, which can be attributed to the contribution of plastic deformation resulted from constant stress.

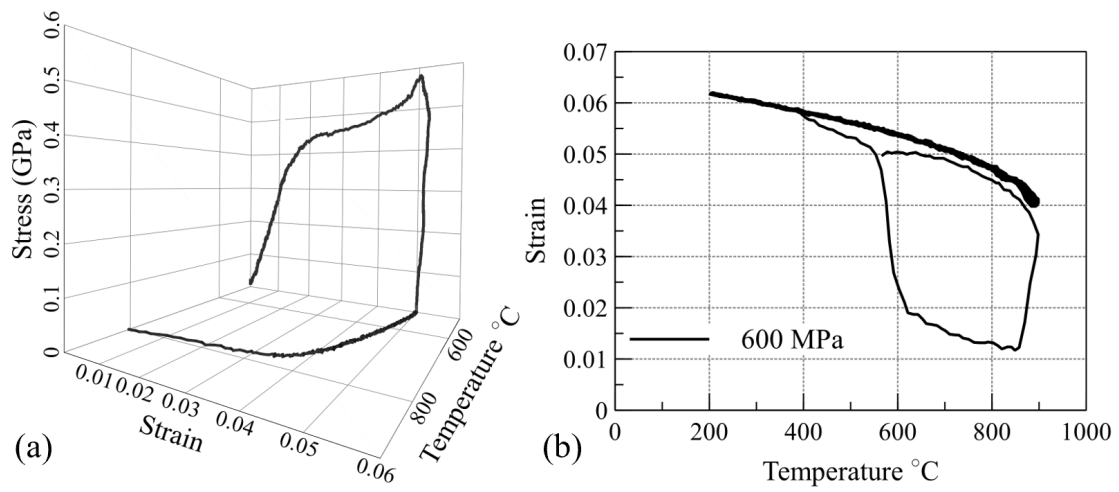


Figure 5.5 (a) Stress-strain-temperature curve, and (b) shape memory response of the material subjected to thermal cycling under 600 MPa constant stress

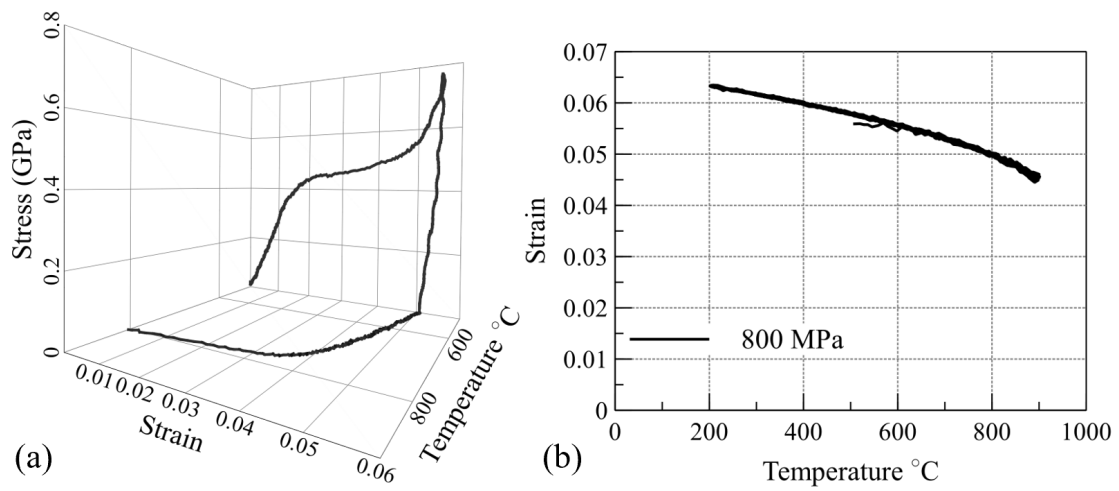


Figure 5.6 (a) Stress-strain-temperature curve, and (b) shape memory response of the material subjected to thermal cycling under 800 MPa constant stress

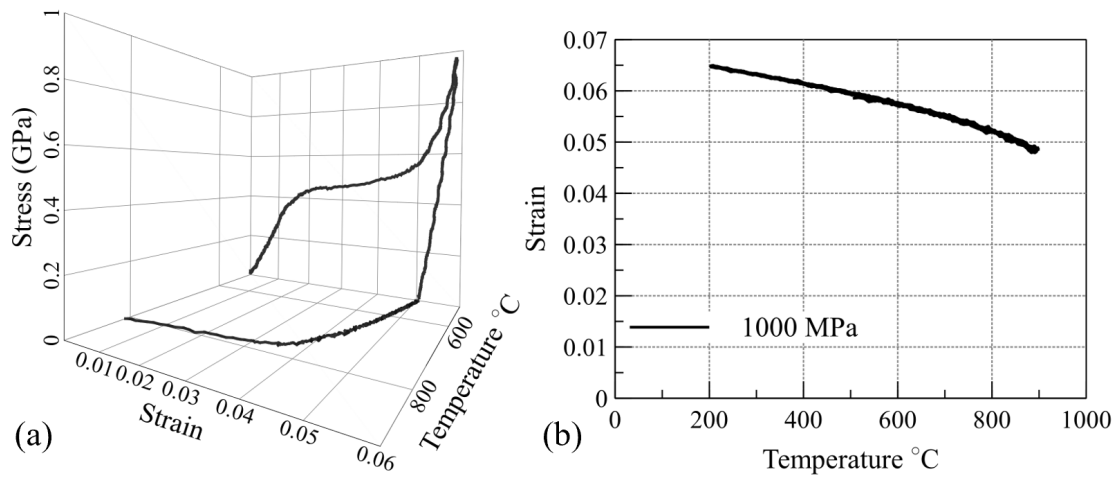


Figure 5.7 (a) Stress-strain-temperature curve, and (b) shape memory response of the material subjected to thermal cycling under 1000 MPa constant stress

CHAPTER 6

SUMMARY, CONCLUSIONS AND FUTURE WORKS

6.1 Summary and Conclusions

The unique properties of shape memory alloys which can reduce the complexity of multi-component assemblies into single adaptive components, are particularly advantageous in high-temperature applications. The use of SMAs, particularly NiTi, in such applications is limited due to the restricted transformation temperatures below 100 °C. At high temperatures, SMAs lose their proper superelasticity and shape memory effect properties. Moreover, the current SMAs suffer from material property degradation at high temperatures, making them unsuitable for applications at high operating temperatures, due to the risk of failure from insufficient material strength.

The demand for SMAs capable of operating at high temperatures is driven by their potential applications in solid-state actuators, which exhibit high energy densities, reduced weight, and frictionless, noiseless operation. These characteristics make SMA-based solid-state actuators highly desirable for weight-critical systems such as jet turbine engines, spacecraft, and other aerospace applications. To enable the practical utilization of shape memory characteristics in aerospace and automotive applications, the development of high-temperature shape memory alloys (HTSMAs) has become a crucial task. HTSMAs will play a vital role in enhancing the performance and reliability of SMA-based systems in aerospace and other high-temperature environments including clearance control in compressor and turbine sections of jet engines, self-damping components in fuel line clamps, electrical appliances and actuators in proximity to engine parts in automobiles.

NiTi-based HTSMAs are highly popular due to the unique properties of NiTi. There are various approaches for modifying the activation temperature range in NiTi-based SMAs. These approaches include adjusting the alloy composition, applying heat treatment processes, controlling

the microstructure, utilizing alloy combinations, introducing dopants or alloying elements, and applying mechanical processing techniques. Alloying elements like Pt, Cu, Pd, Zr, and Hf can be used, but the expensive nature of Pd, Pt, and Au limits their use to specific high-priority applications like aerospace. In addition, Zr has a strong affinity towards oxygen. Among these alloys, NiTiHf is a promising HTSMA with excellent properties such as cost-effectiveness, exceptional shape memory, high work output, and thermal stability. Previous studies indicate that Hf has a more significant impact on transformation temperatures compared to Pd and Au, even at similar compositions. In spite of the importance of NiTiHf, there is a lack of comprehensive research on different aspects of the thermo-mechanical properties of the alloy.

The computational studies provide a deep understanding of material properties. Among computational methods, atomistic approaches particularly molecular dynamics (MD), can be used for microstructural investigations and design of application-specific materials. MD simulations involve studying the behavior and movement of atoms and molecules over time using interatomic potentials which describe the energy and forces between atoms in a system. The development of reliable interatomic potentials is crucial for accurate MD simulations. To date, no applicable interatomic potential has been developed for NiTiHf which has resulted in an untouched research area of MD studies on NiTiHf.

In this study, a Second Nearest-Neighbor Modified Embedded Atom Method (2NN MEAM) interatomic potential was developed for ternary NiTiHf. MEAM potential has shown to be a great candidate to describe the mechanical properties of multi-element alloys with different ground states. To calibrate this MEAM potential, the constituent unary and binary systems (i.e. Ni, Ti, HfNi, HfTi, NiTi) had to be calibrated first. The MPC tool [91] was used for the calibration of these interatomic potentials. To calibrate the parameters of each potential, the physical properties of each material were calculated from a lower length scale (in this study DFT method was used for a lower length scale) as target values. Then, the parameters were calibrated based on these target values in a way that they can reproduce the physical properties such as cohesive energy, lattice parameters, vacancy formation energy and surface energies. For DFT simulations, QUANTUM ESPRESSO suite [97] was utilized. The results of unary and binary MEAM potential showed

a good agreement with the experimental and DFT values of each mechanical property. Then, based on constituent MEAM potentials, the ternary MEAM potential was calibrated using MD simulations. The parameters of ternary MEAM potential which were screening parameters, were calibrated to reproduce the superelasticity and shape memory effect in NiTiHf alloy.

In order to study the reliability and transferability of the MEAM potential, the lattice parameters of austenitic B2 and martensitic B19' were calculated using the developed MEAM potential. The results showed a good agreement with the experimental values of each lattice parameter. Furthermore, the formation energy of NiTiHf alloys with different compositions was computed using the developed potential and DFT method, showing close results.

In addition, the temperature-induced and stress-induced phase transformation of NiTiHf was simulated using the developed MEAM potential. A popular and frequently-used composition i.e. $\text{Ni}_{50.3}\text{Ti}_{29.7}\text{Hf}_{20}$ was considered and simulation box was generated. In order to attain the targeted NiTiHf composition, a predetermined quantity of Ti atoms within the equiatomic NiTi box was chosen randomly (according to the desired NiTiHf composition) and substituted with Hf atoms. Periodic boundary conditions were employed in all directions to minimize surface effects and to allow the atoms in the system to interact as if they were part of an infinite lattice. For temperature-induced phase transformation, a cooling and heating cycle between 900 °C and -100 °C was applied to the model. By recording the atomic volume during the thermal cycle, transformation temperatures were obtained indicated by sudden increase and decrease in the atomic volume. Moreover, the phase transformation of the alloy was visualized using color coding showing martensitic and austenitic phases that were present in the material. The dependency of the M_s and A_f temperatures on the model size was also studied. Numerous models containing atoms ranging from 2000 to 1,000,000 were modeled and their TTs were captured. The results showed that TT values become more stable and fluctuate less when the size of the model is large ($\geq 200,000$ atoms).

For stress-induced phase transformation, a monotonic compressive load was applied to the models with the same size at three different temperatures ($T > A_f$, $T < M_f$, $T > M_s$) to capture superelastic, martensitic and mixed phase behavior of NiTiHf. The compressive load was applied

in [100] direction gradually up to 2 GPa. The stress-strain graphs showed residual strain for martensitic and mixed phase models unlike the superelastic model (as has been reported in the previous studies). In addition, twinning planes were observed in the superelastic model during phase transformation.

To overcome some challenges of employing HTSMAs at high temperatures like large plastic deformations and unstable cyclic performance, precipitate hardening has shown to be the most applicable and cost-effective approach. The addition of nanoparticles to the material can enhance the strength of the matrix by raising the critical shear stress needed for slip to occur. Different types of precipitates can form during the aging of Ni-rich and Ti-rich NiTiHf alloys. Ni-rich alloys have become more popular recently due to their superior properties compared to Ti-rich alloys. The crystal structure of the precipitate that forms in $\text{Ni}_{50.3}\text{Ti}_{29.7}\text{Hf}_{20}$ was previously characterized and reported. Therefore, to investigate the effect of H-phase precipitates on superelasticity and shape memory response of NiTiHf alloy, oblate spindle-like precipitate was generated with Ni_3TiHf_2 crystal structure and embedded into the NiTiHf box. Models with single and large precipitate (called single-precipitate model) and multiple fine precipitates (called multi-precipitate model) were created. By obtaining the TTs of models, it was found that A_s and A_f of precipitated models increased resulted from a slower reverse phase transformation that occurred due to the presence of fewer nucleation zones.

Furthermore, MD simulations were conducted to analyze the influence of precipitates on the superelasticity and shape memory effect of NiTiHf alloy under compressive stress at austenitic and martensitic temperatures. The results showed that in the presence of H-phase precipitates, the martensitic matrix undergoes adjustments to accommodate these non-transforming particles, resulting in increased strain levels. Additionally, the yield stress in models with precipitates was higher compared to model without precipitate. This is because the precipitates serve as obstacles to dislocation movement within the alloy, effectively enhancing the material's strength by impeding dislocation slip. The single-precipitate model showed poor superelastic behavior with some irrecoverable strain after unloading. This phenomenon was attributed to the loss of coherency between the large precipitate and the matrix. On the contrary, in the multi-precipitate

model, an improved superelastic behavior was observed due to the presence of coherent and smaller precipitates distributed throughout the material.

Since it was reported that the crystallographic orientation of Ni-rich NiTi alloys has a significant influence on their shape memory and mechanical properties, the direction-dependence of NiTiHf and the impact of H-phase precipitates on its mechanical response were investigated in this study. Models with and without precipitate were subjected to compressive load along [110] direction and it was observed at high temperatures, the superelastic behavior is significantly different than the [100] direction. The maximum strain in [110] direction was approximately half of what was observed in the equivalent models in [100] direction. Additionally, the energy dissipation in the [110] models was significantly lower compared to the [100] models. Moreover, compared to single-precipitate and precipitate-free models, the energy dissipation was smaller in the multi-precipitate model in [110] direction.

In materials undergoing phase transformations like SMAs, fatigue can arise not only from cyclic load variations but also from the physical motion of atoms during phase transformations. Actuation fatigue specifically refers to the degradation of dimensional integrity in SMA actuators due to the accumulation of plastic strains during thermal cycling. Other shape memory characteristics, such as transformation temperatures, thermal hysteresis, and actuation strain, can also change significantly during thermal cycling, known as functional fatigue. Optimizing the microstructure of Ni-rich NiTiHf alloys is crucial for achieving optimal actuation fatigue performance. With the aim of understanding the behavior of Ni-rich NiTiHf high-temperature SMAs under thermal cycling with constant stress, simulations were performed on MD models using $\text{Ni}_{50.3}\text{Ti}_{29.7}\text{Hf}_{20}$ composition to study the influence of microstructure on the thermal actuation of the alloy. The observation revealed that reducing the temperature rate resulted in a narrower thermal hysteresis. However, the temperature rate had minimal impact on the range of recoverable strain. Furthermore, increasing the constant stress led to the absence of a shape memory response. This lack of response was attributed to the presence of plastic deformation caused by the elevated constant stress.

6.2 Future Works

Figure 6.1 [159] presents a schematic representation of the ultimate strength of various material classes. Based on previous calculations, the ratio of actual strength to ideal strength can be calculated as 25% for Ni-rich NiTiHf. Considering the ultimate strength values, this ratio is remarkably high compared to conventional materials, as the actual to ideal strength ratio for conventional steels is typically less than 20%. These findings highlight the exceptional strength and mechanical properties exhibited by Ni-rich NiTiHf alloys, surpassing those of conventional steels and shape memory alloys. This intriguing result opens up exciting possibilities for further exploration and investigation of NiTiHf alloys.

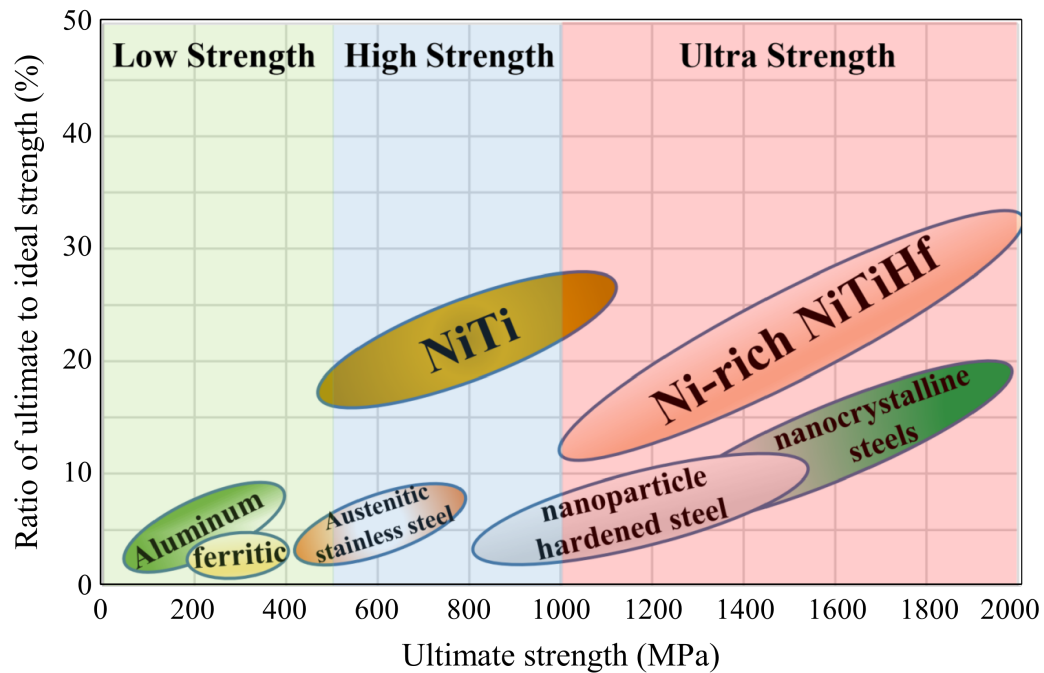


Figure 6.1 Schematic presentation of common materials strength [159]

By employing the developed ternary MEAM potential of NiTiHf, systematic MD simulations can be performed on different compositions of NiTiHf to understand the current unknowns of these alloys. Among these unknowns, further investigations are needed to explore the effects of subtle modifications in the lattice parameters of Ni-rich NiTiHf HTSMAs. It is widely recognized

that improved compatibility between the transforming phases results in reduced dissipation [160]. The compatibility, in turn, is heavily influenced by the lattice parameters of the transforming phases, which are intricately linked to the matrix composition and temperature. To advance our understanding of this relationship and exploit its potential, systematic studies are needed to investigate the influence of alloy composition, heat treatments, and processing methods on achieving slight alterations in the lattice parameters. Gaining a comprehensive understanding of the interplay between composition, temperature, and lattice parameters will facilitate the optimization of compatibility between the transforming phases.

Due to high efficiency, MD simulations can be used to investigate the impact of Ni content on lattice parameters and transformation temperatures in NiTiHf alloys. These simulations can provide atomic scale insights into the relationship between Ni concentration, lattice distortions, and phase stability. By systematically varying the Ni content, it is possible to predict the corresponding changes in lattice parameters and transformation temperatures, thereby elucidating the underlying mechanisms in the path of alloy design.

In addition, the optimum design of the material can be achieved by controlling the distribution of precipitates within the material, equivalent to different aging times. Utilizing computational modeling and experimental techniques to tailor the distribution of precipitates in the material and mimic the effects of different aging times, is an attractive option. By studying the mechanical properties, phase transformations, and microstructural evolution, the optimal precipitate distribution can be determined to enhance the material's strength, fatigue resistance, and shape memory behavior.

REFERENCES

- [1] D. C. Lagoudas, *Shape memory alloys: modeling and engineering applications*. Springer, 2008.
- [2] V. Birman, “Review of mechanics of shape memory alloy structures,” 1997.
- [3] M. Sreekumar, T. Nagarajan, M. Singaperumal, M. Zoppi, and R. Molfino, “Critical review of current trends in shape memory alloy actuators for intelligent robots,” *Industrial Robot: An International Journal*, 2007.
- [4] M. Formentini and S. Lenci, “An innovative building envelope (kinetic façade) with shape memory alloys used as actuators and sensors,” *Automation in Construction*, vol. 85, pp. 220–231, 2018.
- [5] K. Ikuta, “Micro/miniature shape memory alloy actuator,” in *Proceedings., IEEE International Conference on Robotics and Automation*, pp. 2156–2161, IEEE, 1990.
- [6] D. J. Hartl and D. C. Lagoudas, “Aerospace applications of shape memory alloys,” *Proceedings of the Institution of Mechanical Engineers, Part G: Journal of Aerospace Engineering*, vol. 221, no. 4, pp. 535–552, 2007.
- [7] L. Petrini and F. Migliavacca, “Biomedical applications of shape memory alloys,” *Journal of Metallurgy*, vol. 2011, 2011.
- [8] J. M. Jani, M. Leary, and A. Subic, “Shape memory alloys in automotive applications,” in *Applied Mechanics and Materials*, vol. 663, pp. 248–253, Trans Tech Publ, 2014.
- [9] C. Zanotti, P. Giuliani, and A. Chrysanthou, “Martensitic–austenitic phase transformation of ni–ti smas: thermal properties,” *Intermetallics*, vol. 24, pp. 106–114, 2012.
- [10] K. Otsuka and C. M. Wayman, *Shape memory materials*. Cambridge university press, 1999.
- [11] T. Tadaki, K. Otsuka, and K. Shimizu, “Shape memory alloys,” *Annual Review of Materials Science*, vol. 18, no. 1, pp. 25–45, 1988.
- [12] G. B. Kauffman and I. Mayo, “The story of nitinol: the serendipitous discovery of the memory metal and its applications,” *The chemical educator*, vol. 2, pp. 1–21, 1997.
- [13] K. Otsuka and X. Ren, “Physical metallurgy of ti–ni-based shape memory alloys,” *Progress in materials science*, vol. 50, no. 5, pp. 511–678, 2005.

- [14] L. Yahia, *Shape memory implants*. Springer Science & Business Media, 2012.
- [15] S. Ataollahi and M. J. Mahtabi, “Effects of precipitate on the phase transformation of single-crystal niti alloy under thermal and mechanical loads: A molecular dynamics study,” *Materials Today Communications*, vol. 29, p. 102859, 2021.
- [16] M. Es-Souni, M. Es-Souni, and H. Fischer-Brandies, “Assessing the biocompatibility of niti shape memory alloys used for medical applications,” *Analytical and bioanalytical chemistry*, vol. 381, pp. 557–567, 2005.
- [17] C. Liang, F. M. Davidson, L. M. Schetky, and F. K. Straub, “Applications of torsional shape memory alloy actuators for active rotor blade control: opportunities and limitations,” in *Smart Structures and Materials 1996: Smart Structures and Integrated Systems*, vol. 2717, pp. 91–100, SPIE, 1996.
- [18] L. Garner, L. Wilson, D. Lagoudas, and O. Rediniotis, “Development of a shape memory alloy actuated biomimetic vehicle,” *Smart Materials and structures*, vol. 9, no. 5, p. 673, 2000.
- [19] V. Brailovski and F. Trochu, “Review of shape memory alloys medical applications in russia,” *Bio-medical materials and engineering*, vol. 6, no. 4, pp. 291–298, 1996.
- [20] S. Ataollahi and M. J. Mahtabi, “A molecular dynamics study on the effect of precipitate on the phase transformation in niti,”
- [21] T. Philip and P. A. Beck, “CscI-type ordered structures in binary alloys of transition elements,” *JOM*, vol. 9, pp. 1269–1271, 1957.
- [22] Q.-P. Sun and Z.-Q. Li, “Phase transformation in superelastic niti polycrystalline microtubes under tension and torsion—from localization to homogeneous deformation,” *International Journal of Solids and Structures*, vol. 39, no. 13-14, pp. 3797–3809, 2002.
- [23] P. Sittner, Y. Liu, and V. Novák, “On the origin of lüders-like deformation of niti shape memory alloys,” *Journal of the Mechanics and Physics of Solids*, vol. 53, no. 8, pp. 1719–1746, 2005.
- [24] D. Favier, Y. Liu, L. Orgeas, and G. Rio, “Mechanical instability of niti in tension, compression and shear,” in *IUTAM Symposium on Mechanics of Martensitic Phase Transformation in Solids: Proceedings of the IUTAM Symposium held in Hong Kong, China, 11–15 June 2001*, pp. 205–212, Springer, 2002.
- [25] G. Firstov, J. Van Humbeeck, and Y. N. Koval, “High temperature shape memory alloys problems and prospects,” *Journal of intelligent material systems and structures*, vol. 17, no. 12, pp. 1041–1047, 2006.
- [26] J. Van Humbeeck, “Shape memory alloys: a material and a technology,” *Advanced engineering materials*, vol. 3, no. 11, pp. 837–850, 2001.

- [27] S. Padula, S. Qiu, D. Gaydos, R. Noebe, G. Bigelow, A. Garg, and R. Vaidyanathan, "Effect of upper-cycle temperature on the load-biased, strain-temperature response of niti," *Metallurgical and Materials Transactions A*, vol. 43, pp. 4610–4621, 2012.
- [28] G. S. Ded, "Characterization of ni-rich nitihf based high temperature shape memory alloys," 2010.
- [29] R. Noebe, T. Biles, and S. Padula, "Niti-based high-temperature shape-memory alloys: properties, prospects, and potential applications," *MATERIALS ENGINEERING-NEW YORK-*, vol. 32, p. 145, 2006.
- [30] M. Constantinou, C. Pfeiffer, and M. Mosley, "Conventional actuators, shape memory alloys and electrorheological fluids," *Automation, Miniature Robotics and Sensors for Non-Destructive Testing and Evaluation*, 1999.
- [31] R. Noebe, D. Gaydos, I. Santo Padula, A. Garg, T. Biles, and M. Nathal, "Properties and potential of two (ni, pt) ti alloys for use as high-temperature actuator materials," in *Smart Structures and Materials 2005: Active Materials: Behavior and Mechanics*, vol. 5761, pp. 364–375, SPIE, 2005.
- [32] T. R. Quackenbush, B. F. Carpenter, A. H. Boschitsch, and P. V. Danilov, "Development and test of an htsma supersonic inlet ramp actuator," in *Industrial and Commercial Applications of Smart Structures Technologies 2008*, vol. 6930, pp. 185–195, SPIE, 2008.
- [33] J. H. Mabe, F. T. Calkins, and M. B. Alkisar, "Variable area jet nozzle using shape memory alloy actuators in an antagonistic design," in *Industrial and Commercial Applications of Smart Structures Technologies 2008*, vol. 6930, pp. 233–244, SPIE, 2008.
- [34] J. Van Humbeeck, M. Chandrasekaran, and L. Delaey, "Shape memory alloys: materials in action," *Endeavour*, vol. 15, no. 4, pp. 148–154, 1991.
- [35] J. Ma, I. Karaman, and R. D. Noebe, "High temperature shape memory alloys," *International Materials Reviews*, vol. 55, no. 5, pp. 257–315, 2010.
- [36] B. Kockar, I. Karaman, J. Kim, and Y. Chumlyakov, "A method to enhance cyclic reversibility of nitihf high temperature shape memory alloys," *Scripta materialia*, vol. 54, no. 12, pp. 2203–2208, 2006.
- [37] M. Nishida and C. Wayman, "Electron microscopy studies of precipitation processes in near-equiatomic tni shape memory alloys," *Materials Science and Engineering*, vol. 93, pp. 191–203, 1987.
- [38] A. R. Pelton, S. M. Russell, and J. DiCello, "The physical metallurgy of nitinol for medical applications," *Jom*, vol. 55, no. 5, pp. 33–37, 2003.
- [39] K. Bhattacharya *et al.*, *Microstructure of martensite: why it forms and how it gives rise to the shape-memory effect*, vol. 2. Oxford University Press, 2003.

- [40] P. K. Kumar, U. Desai, J. A. Monroe, D. C. Lagoudas, I. Karaman, G. Bigelow, and R. D. Noebe, "Experimental investigation of simultaneous creep, plasticity and transformation of ti50. 5pd30ni19. 5 high temperature shape memory alloy during cyclic actuation," *Materials Science and Engineering: A*, vol. 530, pp. 117–127, 2011.
- [41] J. Monroe, I. Karaman, D. Lagoudas, G. Bigelow, R. Noebe, and S. Padula II, "Determining recoverable and irrecoverable contributions to accumulated strain in a nitipd high-temperature shape memory alloy during thermomechanical cycling," *Scripta Materialia*, vol. 65, no. 2, pp. 123–126, 2011.
- [42] A. P. Stebner, G. S. Bigelow, J. Yang, D. P. Shukla, S. M. Saghaian, R. Rogers, A. Garg, H. E. Karaca, Y. Chumlyakov, K. Bhattacharya, *et al.*, "Transformation strains and temperatures of a nickel–titanium–hafnium high temperature shape memory alloy," *Acta materialia*, vol. 76, pp. 40–53, 2014.
- [43] A. Evirgen, I. Karaman, R. Santamarta, J. Pons, C. Hayrettin, and R. Noebe, "Relationship between crystallographic compatibility and thermal hysteresis in ni-rich nitihf and nitizr high temperature shape memory alloys," *Acta Materialia*, vol. 121, pp. 374–383, 2016.
- [44] A. Evirgen, I. Karaman, R. Noebe, R. Santamarta, and J. Pons, "Effect of precipitation on the microstructure and the shape memory response of the ni50. 3ti29. 7zr20 high temperature shape memory alloy," *Scripta Materialia*, vol. 69, no. 5, pp. 354–357, 2013.
- [45] Y. Shirakawa, Y. Morizono, and M. Nishida, "New precipitate phase in pd and ni rich ti-pd-ni shape memory alloys," in *Materials science forum*, vol. 327, pp. 171–174, Trans Tech Publications, 2000.
- [46] R. Wasilewski, S. Butler, J. Hanlon, and D. Worden, "Homogeneity range and the martensitic transformation in tini," *Metallurgical Transactions*, vol. 2, pp. 229–238, 1971.
- [47] J. Yang and J. Simpson, "Stress-induced transformation and superelasticity in ni-ti-nb alloys," *Journal de Physique iv*, vol. 5, no. C8, pp. C8–771, 1995.
- [48] N. Boriskina, E. Kenina, and T. Tumanova, "Phase equilibria and several properties of ti-tiPd-tini system alloys at 400 deg c," *Izvestiya Akademii Nauk SSSR*, vol. 5, no. C8, pp. 13–17, 1982.
- [49] T. W. Duerig, K. Melton, and D. Stöckel, *Engineering aspects of shape memory alloys*. Butterworth-heinemann, 2013.
- [50] S. Shimizu, Y. Xu, E. Okunishi, S. Tanaka, K. Otsuka, and K. Mitose, "Improvement of shape memory characteristics by precipitation-hardening of ti pd ni alloys," *Materials letters*, vol. 34, no. 1-2, pp. 23–29, 1998.
- [51] W. S. Yang and D. Mikkola, "Ductilization of ti-ni-pd shape memory alloys with boron additions," *Scripta metallurgica et materialia*, vol. 28, no. 2, pp. 161–165, 1993.

- [52] K. Eckelmeyer, "Effect of alloying on the shape memory phenomenon in nitinol," *Scr Metall.:(United States)*, vol. 10, no. 8, 1976.
- [53] H. Donkersloot and J. Van Vucht, "Martensitic transformations in gold-titanium, palladium-titanium and platinum-titanium alloys near the equiatomic composition," *Journal of the Less Common Metals*, vol. 20, no. 2, pp. 83–91, 1970.
- [54] P. Lindquist and C. Wayman, "Shape memory and transformation behavior of martensitic ti–pd–ni and ti–pt–ni alloys," *Butterworth-Heinemann, Engineering Aspects of Shape Memory Alloys(UK)*, 1990, pp. 58–68, 1990.
- [55] H. Hosoda, M. Tsuji, Y. Takahashi, T. Inamura, K. Wakashima, Y. Yamabe-Mitarai, S. Miyazaki, and K. Inoue, "Phase stability and mechanical properties of ti-ni shape memory alloys containing platinum group metals," in *Materials Science Forum*, vol. 426, pp. 2333–2338, Trans Tech Publ, 2003.
- [56] J. Mulder, "Investigation on high temperature shape memory alloys using ni-ti-zr and ni-ti-hf system," *University of Twente, Enschede, The Netherlands*, 1994.
- [57] L. Meisner and V. Sivokha, "Deformation of crystal lattice in the process of martensitic transformation in alloys of ni₅₀ti_{50-x}zrx," *Journal De Physique IV*, vol. 5, no. C8, pp. C8–765, 1995.
- [58] G. Firstov, J. Van Humbeeck, and Y. N. Koval, "Comparison of high temperature shape memory behaviour for zrcu-based, ti–ni–zr and ti–ni–hf alloys," *Scripta Materialia*, vol. 50, no. 2, pp. 243–248, 2004.
- [59] H. Sehitoglu, Y. Wu, L. Patriarca, G. Li, A. Ojha, S. Zhang, Y. Chumlyakov, and M. Nishida, "Superelasticity and shape memory behavior of nitihf alloys," *Shape Memory and Superelasticity*, vol. 3, pp. 168–187, 2017.
- [60] L. C. Chang and T. Read, "Plastic deformation and diffusionless phase changes in metals—the gold-cadmium beta phase," *Jom*, vol. 3, pp. 47–52, 1951.
- [61] T. Saburi and C. Wayman, "Crystallographic similarities in shape memory martensites," *Acta Metallurgica*, vol. 27, no. 6, pp. 979–995, 1979.
- [62] K. Wu and Z. Pu, "Martensite transformation of (hfxti_{50-x}) ni₅₀shape memory alloys," *Journal de Physique IV*, vol. 5, no. C8, pp. C8–801, 1995.
- [63] M. Nishida, C. M. Wayman, and T. Honma, "Precipitation processes in near-equiatomic tini shape memory alloys," *Metallurgical Transactions A*, vol. 17, pp. 1505–1515, 1986.
- [64] X. Meng, Y. Zheng, Z. Wang, and L. Zhao, "Effect of aging on the phase transformation and mechanical behavior of ti₃₆ni₄₉hf₁₅ high temperature shape memory alloy," *Scripta materialia*, vol. 42, no. 4, pp. 341–348, 2000.

- [65] S. Saghaian, H. Karaca, H. Tobe, A. Turabi, S. Saedi, S. Saghaian, Y. Chumlyakov, and R. Noebe, “High strength nitihf shape memory alloys with tailorable properties,” *Acta Materialia*, vol. 134, pp. 211–220, 2017.
- [66] H. Karaca, S. Saghaian, G. Ded, H. Tobe, B. Basaran, H. Maier, R. Noebe, and Y. Chumlyakov, “Effects of nanoprecipitation on the shape memory and material properties of an ni-rich nitihf high temperature shape memory alloy,” *Acta Materialia*, vol. 61, no. 19, pp. 7422–7431, 2013.
- [67] D. R. Coughlin, L. Casalena, F. Yang, R. D. Noebe, and M. J. Mills, “Microstructure–property relationships in a high-strength 51ni–29ti–20hf shape memory alloy,” *Journal of materials science*, vol. 51, pp. 766–778, 2016.
- [68] D. Coughlin, P. Phillips, G. Bigelow, A. Garg, R. Noebe, and M. Mills, “Characterization of the microstructure and mechanical properties of a 50.3 ni–29.7 ti–20hf shape memory alloy,” *Scripta Materialia*, vol. 67, no. 1, pp. 112–115, 2012.
- [69] F. Yang, D. Coughlin, P. J. Phillips, L. Yang, A. Devaraj, L. Kovarik, R. D. Noebe, and M. Mills, “Structure analysis of a precipitate phase in an ni-rich high-temperature nitihf shape memory alloy,” *Acta Materialia*, vol. 61, no. 9, pp. 3335–3346, 2013.
- [70] L. E. Murr, “Computer simulation in materials science and engineering,” in *Handbook of Materials Structures, Properties, Processing and Performance*, pp. 1105–1121, Springer, 2015.
- [71] M. Horstemeyer, D. Farkas, S. Kim, T. Tang, and G. Potirniche, “Nanostructurally small cracks (nsc): A review on atomistic modeling of fatigue,” *International Journal of Fatigue*, vol. 32, no. 9, pp. 1473–1502, 2010.
- [72] A. I. Vakis, V. A. Yastrebov, J. Scheibert, L. Nicola, D. Dini, C. Minfray, A. Almqvist, M. Paggi, S. Lee, G. Limbert, *et al.*, “Modeling and simulation in tribology across scales: An overview,” *Tribology International*, vol. 125, pp. 169–199, 2018.
- [73] S. D. Brown, R. Tauler, and B. Walczak, *Comprehensive chemometrics: chemical and biochemical data analysis*. Elsevier, 2020.
- [74] M. H. Müser, S. V. Sukhomlinov, and L. Pastewka, “Interatomic potentials: Achievements and challenges,” *Advances in Physics: X*, vol. 8, no. 1, p. 2093129, 2023.
- [75] V. Bulatov and W. Cai, *Computer simulations of dislocations*, vol. 3. OUP Oxford, 2006.
- [76] J. E. Jones, “On the determination of molecular fields.—i. from the variation of the viscosity of a gas with temperature,” *Proceedings of the Royal Society of London. Series A, Containing Papers of a Mathematical and Physical Character*, vol. 106, no. 738, pp. 441–462, 1924.

- [77] M. S. Daw, S. M. Foiles, and M. I. Baskes, "The embedded-atom method: a review of theory and applications," *Materials Science Reports*, vol. 9, no. 7-8, pp. 251–310, 1993.
- [78] M. S. Daw and M. I. Baskes, "Embedded-atom method: Derivation and application to impurities, surfaces, and other defects in metals," *Physical Review B*, vol. 29, no. 12, p. 6443, 1984.
- [79] M. Finnis and J. Sinclair, "A simple empirical n-body potential for transition metals," *Philosophical Magazine A*, vol. 50, no. 1, pp. 45–55, 1984.
- [80] J. Nørskov and N. Lang, "Effective-medium theory of chemical binding: Application to chemisorption," *Physical Review B*, vol. 21, no. 6, p. 2131, 1980.
- [81] V. Rosato, M. Guillope, and B. Legrand, "Thermodynamical and structural properties of fcc transition metals using a simple tight-binding model," *Philosophical Magazine A*, vol. 59, no. 2, pp. 321–336, 1989.
- [82] M. Baskes, J. Nelson, and A. Wright, "Semiempirical modified embedded-atom potentials for silicon and germanium," *Physical Review B*, vol. 40, no. 9, p. 6085, 1989.
- [83] B.-J. Lee and M. I. Baskes, "Second nearest-neighbor modified embedded-atom-method potential," *Physical Review B*, vol. 62, no. 13, p. 8564, 2000.
- [84] M. I. Baskes, "Modified embedded-atom potentials for cubic materials and impurities," *Physical review B*, vol. 46, no. 5, p. 2727, 1992.
- [85] M. I. Baskes, J. Angelo, and C. Bisson, "Atomistic calculations of composite interfaces," *Modelling and Simulation in Materials Science and Engineering*, vol. 2, no. 3A, p. 505, 1994.
- [86] B.-J. Lee, "A modified embedded-atom method interatomic potential for the fe–c system," *Acta materialia*, vol. 54, no. 3, pp. 701–711, 2006.
- [87] B.-J. Lee, M. Baskes, H. Kim, and Y. K. Cho, "Second nearest-neighbor modified embedded atom method potentials for bcc transition metals," *Physical Review B*, vol. 64, no. 18, p. 184102, 2001.
- [88] J. H. Rose, J. R. Smith, F. Guinea, and J. Ferrante, "Universal features of the equation of state of metals," *Physical Review B*, vol. 29, no. 6, p. 2963, 1984.
- [89] B.-J. Lee, W.-S. Ko, H.-K. Kim, and E.-H. Kim, "The modified embedded-atom method interatomic potentials and recent progress in atomistic simulations," *Calphad*, vol. 34, no. 4, pp. 510–522, 2010.
- [90] R. G. Parr, "Density functional theory of atoms and molecules," in *Horizons of Quantum Chemistry: Proceedings of the Third International Congress of Quantum Chemistry Held at Kyoto, Japan, October 29-November 3, 1979*, pp. 5–15, Springer, 1980.

- [91] C. D. Barrett and R. L. Carino, “The meam parameter calibration tool: an explicit methodology for hierarchical bridging between ab initio and atomistic scales,” *Integrating Materials and Manufacturing Innovation*, vol. 5, pp. 177–191, 2016.
- [92] B. Jelinek, S. Groh, M. F. Horstemeyer, J. Houze, S.-G. Kim, G. J. Wagner, A. Moitra, and M. I. Baskes, “Modified embedded atom method potential for al, si, mg, cu, and fe alloys,” *Physical Review B*, vol. 85, no. 24, p. 245102, 2012.
- [93] X. Huang, L. Liu, X. Duan, W. Liao, J. Huang, H. Sun, and C. Yu, “Atomistic simulation of chemical short-range order in hfnbtazr high entropy alloy based on a newly-developed interatomic potential,” *Materials & Design*, vol. 202, p. 109560, 2021.
- [94] P. Hohenberg and W. Kohn, “Inhomogeneous electron gas,” *Physical review*, vol. 136, no. 3B, p. B864, 1964.
- [95] D. S. Sholl and J. A. Steckel, *Density functional theory: a practical introduction*. John Wiley & Sons, 2022.
- [96] L. Küne, “Recent developments and applications of modern density functional theory,” 1998.
- [97] P. Giannozzi, S. Baroni, N. Bonini, M. Calandra, R. Car, C. Cavazzoni, D. Ceresoli, G. L. Chiarotti, M. Cococcioni, I. Dabo, *et al.*, “Quantum espresso: a modular and open-source software project for quantum simulations of materials,” *Journal of physics: Condensed matter*, vol. 21, no. 39, p. 395502, 2009.
- [98] F. Birch, “Finite elastic strain of cubic crystals,” *Physical review*, vol. 71, no. 11, p. 809, 1947.
- [99] T. R. Mattsson and A. E. Mattsson, “Calculating the vacancy formation energy in metals: Pt, pd, and mo,” *Physical Review B*, vol. 66, no. 21, p. 214110, 2002.
- [100] R. Tran, Z. Xu, B. Radhakrishnan, D. Winston, W. Sun, K. A. Persson, and S. P. Ong, “Surface energies of elemental crystals,” *Scientific data*, vol. 3, no. 1, pp. 1–13, 2016.
- [101] C. Kittel, *Introduction to solid state physics*. John Wiley & sons, inc, 2005.
- [102] R. Birgeneau, J. Cordes, G. Dolling, and A. D. B. Woods, “Normal modes of vibration in nickel,” *Physical Review*, vol. 136, no. 5A, p. A1359, 1964.
- [103] H. M. Ledbetter and R. P. Reed, “Elastic properties of metals and alloys, i. iron, nickel, and iron-nickel alloys,” *Journal of Physical and Chemical Reference Data*, vol. 2, no. 3, pp. 531–618, 1973.
- [104] J. Neighbours, F. Bratten, and C. S. Smith, “The elastic constants of nickel,” *Journal of Applied Physics*, vol. 23, no. 4, pp. 389–393, 1952.

- [105] J. Wolff, M. Franz, J.-E. Kluin, and D. Schmid, “Vacancy formation in nickel and α -nickel-carbon alloy,” *Acta materialia*, vol. 45, no. 11, pp. 4759–4764, 1997.
- [106] W. Tyson and W. Miller, “Surface free energies of solid metals: Estimation from liquid surface tension measurements,” *Surface Science*, vol. 62, no. 1, pp. 267–276, 1977.
- [107] C. Barrett and T. Massalski, “Structure of metals: Crystallographic methods, principles, and data, vol. 35 of international series on materials science and technology,” 1987.
- [108] G. Simmons, “Single crystal elastic constants and calculated aggregate properties,” *A handbook*, vol. 4, 1971.
- [109] F. R. De Boer, W. Mattens, R. Boom, A. Miedema, and A. Niessen, “Cohesion in metals. transition metal alloys,” 1988.
- [110] W.-S. Ko, B. Grabowski, and J. Neugebauer, “Development and application of a ni-ti interatomic potential with high predictive accuracy of the martensitic phase transition,” *Physical Review B*, vol. 92, no. 13, p. 134107, 2015.
- [111] J. Li, X. Dai, T. Wang, and B. Liu, “A binomial truncation function proposed for the second-moment approximation of tight-binding potential and application in the ternary ni–hf–ti system,” *Journal of Physics: Condensed Matter*, vol. 19, no. 8, p. 086228, 2007.
- [112] A. Jain, S. P. Ong, G. Hautier, W. Chen, W. D. Richards, S. Dacek, S. Cholia, D. Gunter, D. Skinner, G. Ceder, *et al.*, “Commentary: The materials project: A materials genome approach to accelerating materials innovation,” *APL materials*, vol. 1, no. 1, p. 011002, 2013.
- [113] K. G. Vishnu and A. Strachan, “Phase stability and transformations in niti from density functional theory calculations,” *Acta materialia*, vol. 58, no. 3, pp. 745–752, 2010.
- [114] G. Ren and H. Sehitoglu, “Interatomic potential for the niti alloy and its application,” *Computational Materials Science*, vol. 123, pp. 19–25, 2016.
- [115] H.-K. Kim, W.-S. Jung, and B.-J. Lee, “Modified embedded-atom method interatomic potentials for the fe–ti–c and fe–ti–n ternary systems,” *Acta Materialia*, vol. 57, no. 11, pp. 3140–3147, 2009.
- [116] O. Benafan, G. Bigelow, A. Garg, R. Noebe, D. Gaydos, and R. Rogers, “Processing and scalability of nitihf high-temperature shape memory alloys,” *Shape Memory and Superelasticity*, vol. 7, pp. 109–165, 2021.
- [117] G. Bigelow, A. Garg, S. Padula II, D. Gaydos, and R. Noebe, “Load-biased shape-memory and superelastic properties of a precipitation strengthened high-temperature ni50. 3ti29. 7hf20 alloy,” *Scripta Materialia*, vol. 64, no. 8, pp. 725–728, 2011.

- [118] A. P. Thompson, H. M. Aktulga, R. Berger, D. S. Bolintineanu, W. M. Brown, P. S. Crozier, P. J. in't Veld, A. Kohlmeyer, S. G. Moore, T. D. Nguyen, *et al.*, “Lammps-a flexible simulation tool for particle-based materials modeling at the atomic, meso, and continuum scales,” *Computer Physics Communications*, vol. 271, p. 108171, 2022.
- [119] P. Hirel, “Atomsk: A tool for manipulating and converting atomic data files,” *Computer Physics Communications*, vol. 197, pp. 212–219, 2015.
- [120] A. Stukowski, “Visualization and analysis of atomistic simulation data with ovito—the open visualization tool,” *Modelling and simulation in materials science and engineering*, vol. 18, no. 1, p. 015012, 2009.
- [121] P. M. Larsen, S. Schmidt, and J. Schiøtz, “Robust structural identification via polyhedral template matching,” *Modelling and Simulation in Materials Science and Engineering*, vol. 24, no. 5, p. 055007, 2016.
- [122] K. Otsuka and C. Wayman, “Shape memory materials cambridge univ,” *Press, New York*, 1998.
- [123] M. Kassner and M.-T. Pérez-Prado, “Five-power-law creep in single phase metals and alloys,” *Progress in materials science*, vol. 45, no. 1, pp. 1–102, 2000.
- [124] C. P. Frick, A. M. Ortega, J. Tyber, A. E. M. Maksound, H. J. Maier, Y. Liu, and K. Gall, “Thermal processing of polycrystalline niti shape memory alloys,” *Materials Science and Engineering: A*, vol. 405, no. 1-2, pp. 34–49, 2005.
- [125] D. Golberg, Y. Xu, Y. Murakami, S. Morito, K. Otsuka, T. Ueki, and H. Horikawa, “Characteristics of ti50pd30ni20 high-temperature shape memory alloy,” *Intermetallics*, vol. 3, no. 1, pp. 35–46, 1995.
- [126] D. Golberg, Y. Xu, Y. Murakami, K. Otsuka, T. Ueki, and H. Horikawa, “High-temperature shape memory effect in ti50pd50- xnix (x= 10, 15, 20) alloys,” *Materials letters*, vol. 22, no. 5-6, pp. 241–248, 1995.
- [127] J. Khalil-Allafi, A. Dlouhy, and G. Eggeler, “Ni₄ti₃-precipitation during aging of niti shape memory alloys and its influence on martensitic phase transformations,” *Acta materialia*, vol. 50, no. 17, pp. 4255–4274, 2002.
- [128] Y. I. Chumlyakov, E. Y. Panchenko, V. Aksenov, I. Kireeva, M. Kuksa, I. Karaman, and H. Sehitoglu, “The shape memory effect and superelasticity in ti-ni single crystals with one variant of dispersed particles,” in *Journal de Physique IV (Proceedings)*, vol. 115, pp. 21–28, EDP sciences, 2004.
- [129] H. Sehitoglu, D. Canadinc, X. Zhang, T. Kotil, I. Karaman, K. Gall, H. Maier, and Y. Chumlyakov, “Overview of shape memory single crystals,” *Acta Materialia*, vol. 48, no. 13, pp. 3311–3326, 2000.

- [130] J. Jung, G. Ghosh, and G. Olson, "A comparative study of precipitation behavior of heusler phase (ni₂tial) from b2-tini in ni-ti-al and ni-ti-al-x (x= hf, pd, pt, zr) alloys," *Acta Materialia*, vol. 51, no. 20, pp. 6341–6357, 2003.
- [131] J. Jung, G. Ghosh, D. Isheim, and G. Olson, "Precipitation of heusler phase (ni₂ tial) from b2-tini in ni-ti-al and ni-ti-al-x (x= hf, zr) alloys," *Metallurgical and Materials Transactions A*, vol. 34, pp. 1221–1235, 2003.
- [132] D. König, R. Zarnetta, A. Savan, H. Brunken, and A. Ludwig, "Phase transformation, structural and functional fatigue properties of ti-ni-hf shape memory thin films," *Acta Materialia*, vol. 59, no. 8, pp. 3267–3275, 2011.
- [133] P. E. Thoma and J. J. Boehm, "Effect of composition on the amount of second phase and transformation temperatures of nixti_{90-x}hf₁₀ shape memory alloys," *Materials Science and Engineering: A*, vol. 273, pp. 385–389, 1999.
- [134] X. Meng, W. Cai, Y. Fu, J. Zhang, and L. Zhao, "Martensite structure in ti-ni-hf-cu quaternary alloy ribbons containing (ti, hf) 2ni precipitates," *Acta Materialia*, vol. 58, no. 10, pp. 3751–3763, 2010.
- [135] Y. Tong, F. Chen, B. Tian, L. Li, and Y. Zheng, "Microstructure and martensitic transformation of ti₄₉ni_{51-x}hf_x high temperature shape memory alloys," *Materials Letters*, vol. 63, no. 21, pp. 1869–1871, 2009.
- [136] M. M. Javadi, M. Belbasi, M. T. Salehi, and M. R. Afshar, "Effect of aging on the microstructure and shape memory effect of a hot-rolled nitihf alloy," *Journal of materials engineering and performance*, vol. 20, pp. 618–622, 2011.
- [137] X. Meng, W. Cai, F. Chen, and L. Zhao, "Effect of aging on martensitic transformation and microstructure in ni-rich tihf shape memory alloy," *Scripta materialia*, vol. 54, no. 9, pp. 1599–1604, 2006.
- [138] J. Zhang, M. Sato, and A. Ishida, "Structure of martensite in sputter-deposited ti-ni thin films containing homogeneously distributed ti₂ni precipitates," *Philosophical Magazine A*, vol. 82, no. 7, pp. 1433–1449, 2002.
- [139] X. Han, R. Wang, Z. Zhang, and D. Yang, "A new precipitate phase in a tihf high temperature shape memory alloy," *Acta materialia*, vol. 46, no. 1, pp. 273–281, 1998.
- [140] M. Prasher and D. Sen, "Influence of aging on phase transformation and microstructure of ni₅₀.3ti₂₉.7hf₂₀ high temperature shape memory alloy," *Journal of alloys and compounds*, vol. 615, pp. 469–474, 2014.
- [141] R. Santamarta, R. Arróyave, J. Pons, A. Evirgen, I. Karaman, H. Karaca, and R. Noebe, "Tem study of structural and microstructural characteristics of a precipitate phase in ni-rich ni-ti-hf and ni-ti-zr shape memory alloys," *Acta Materialia*, vol. 61, no. 16, pp. 6191–6206, 2013.

- [142] R. F. Hamilton, H. Sehitoglu, Y. Chumlyakov, and H. Maier, “Stress dependence of the hysteresis in single crystal niti alloys,” *Acta Materialia*, vol. 52, no. 11, pp. 3383–3402, 2004.
- [143] H. Sehitoglu, J. Jun, X. Zhang, I. Karaman, Y. Chumlyakov, H. Maier, and K. Gall, “Shape memory and pseudoelastic behavior of 51.5% ni–ti single crystals in solutionized and overaged state,” *Acta Materialia*, vol. 49, no. 17, pp. 3609–3620, 2001.
- [144] H. Sehitoglu, I. Karaman, X. Zhang, A. Viswanath, Y. Chumlyakov, and H. Maier, “Strain–temperature behavior of niticu shape memory single crystals,” *Acta Materialia*, vol. 49, no. 17, pp. 3621–3634, 2001.
- [145] H. Karaca, I. Karaman, Y. Chumlyakov, D. Lagoudas, and X. Zhang, “Compressive response of a single crystalline conial shape memory alloy,” *Scripta Materialia*, vol. 51, no. 3, pp. 261–266, 2004.
- [146] S. Ataollahi and M. J. Mahtabi, “An interatomic potential for ternary nitihf shape memory alloys based on modified embedded atom method,” *Computational Materials Science*, vol. 227, p. 112278, 2023.
- [147] F. Weafer and M. Bruzzi, “Influence of microstructure on the performance of nitinol: a computational analysis,” *Journal of materials engineering and performance*, vol. 23, pp. 2539–2544, 2014.
- [148] K. Gall, H. Sehitoglu, Y. I. Chumlyakov, and I. Kireeva, “Tension–compression asymmetry of the stress–strain response in aged single crystal and polycrystalline niti,” *Acta Materialia*, vol. 47, no. 4, pp. 1203–1217, 1999.
- [149] F. R. Phillips, R. W. Wheeler, A. B. Geltmacher, and D. C. Lagoudas, “Evolution of internal damage during actuation fatigue in shape memory alloys,” *International Journal of Fatigue*, vol. 124, pp. 315–327, 2019.
- [150] O. Karakoc, K. Atli, O. Benafan, R. Noebe, and I. Karaman, “Actuation fatigue performance of nitizr and comparison to nitihf high temperature shape memory alloys,” *Materials Science and Engineering: A*, vol. 829, p. 142154, 2022.
- [151] G. Eggeler, E. Hornbogen, A. Yawny, A. Heckmann, and M. Wagner, “Structural and functional fatigue of niti shape memory alloys,” *Materials Science and Engineering: A*, vol. 378, no. 1-2, pp. 24–33, 2004.
- [152] M. Kamlet and Y. Gibbs, “Nasa tests new alloy to fold wings in flight,” *NASA: Edwards, CA, USA*, 2018.
- [153] R. J., “Metal with memory: Shaping the future of aviation. national aeronautics and space administration [internet]; <https://www.nasa.gov/feature/metal-with-memory-shaping-the-future-of-aviation.>,” *NASA*, 2017.

- [154] T. Umale, *Effect of Composition and Phase Equilibria on Transformation and Precipitation Characteristics in Ni–Ti–Hf High Temperature Shape Memory Alloys*. PhD thesis, 2020.
- [155] O. Karakoc, C. Hayrettin, A. Evirgen, R. Santamarta, D. Canadinc, R. Wheeler, S. Wang, D. Lagoudas, and I. Karaman, “Role of microstructure on the actuation fatigue performance of ni-rich nitihf high temperature shape memory alloys,” *Acta Materialia*, vol. 175, pp. 107–120, 2019.
- [156] L. Delaey, J. Janssen, D. Van de Mosselaer, G. Dullenkopf, and A. Deruyttere, “Fatigue properties of pseudoelastic cu zn al alloys,” *Scripta Metallurgica*, vol. 12, no. 4, pp. 373–376, 1978.
- [157] D. Lagoudas, D. Miller, L. Rong, and P. Kumar, “Thermomechanical fatigue of shape memory alloys,” *Smart Materials and Structures*, vol. 18, no. 8, p. 085021, 2009.
- [158] D. A. Miller and D. C. Lagoudas, “Thermomechanical characterization of niticu and niti sma actuators: influence of plastic strains,” *Smart Materials and Structures*, vol. 9, no. 5, p. 640, 2000.
- [159] S. M. Saghaian, *Shape memory behavior of single crystal and polycrystalline Ni-rich NiTiHf high temperature shape memory alloys*. University of Kentucky, 2015.
- [160] J. Cui, Y. S. Chu, O. O. Famodu, Y. Furuya, J. Hattrick-Simpers, R. D. James, A. Ludwig, S. Thienhaus, M. Wuttig, Z. Zhang, *et al.*, “Combinatorial search of thermoelastic shape-memory alloys with extremely small hysteresis width,” *Nature materials*, vol. 5, no. 4, pp. 286–290, 2006.

VITA

Saeed Ataollahi was born and raised in Tehran, Iran. He is the youngest of four brothers. Before attending the University of Tennessee at Chattanooga, he obtained his Bachelors and Masters of science degrees in civil engineering from Iran. During his PhD studies, he enjoyed utilizing the computational and experimental tools to delve into the material science and mechanical engineering problems. The outcomes of this interdisciplinary research field can help to develop and design novel smart materials and shape memory alloys.